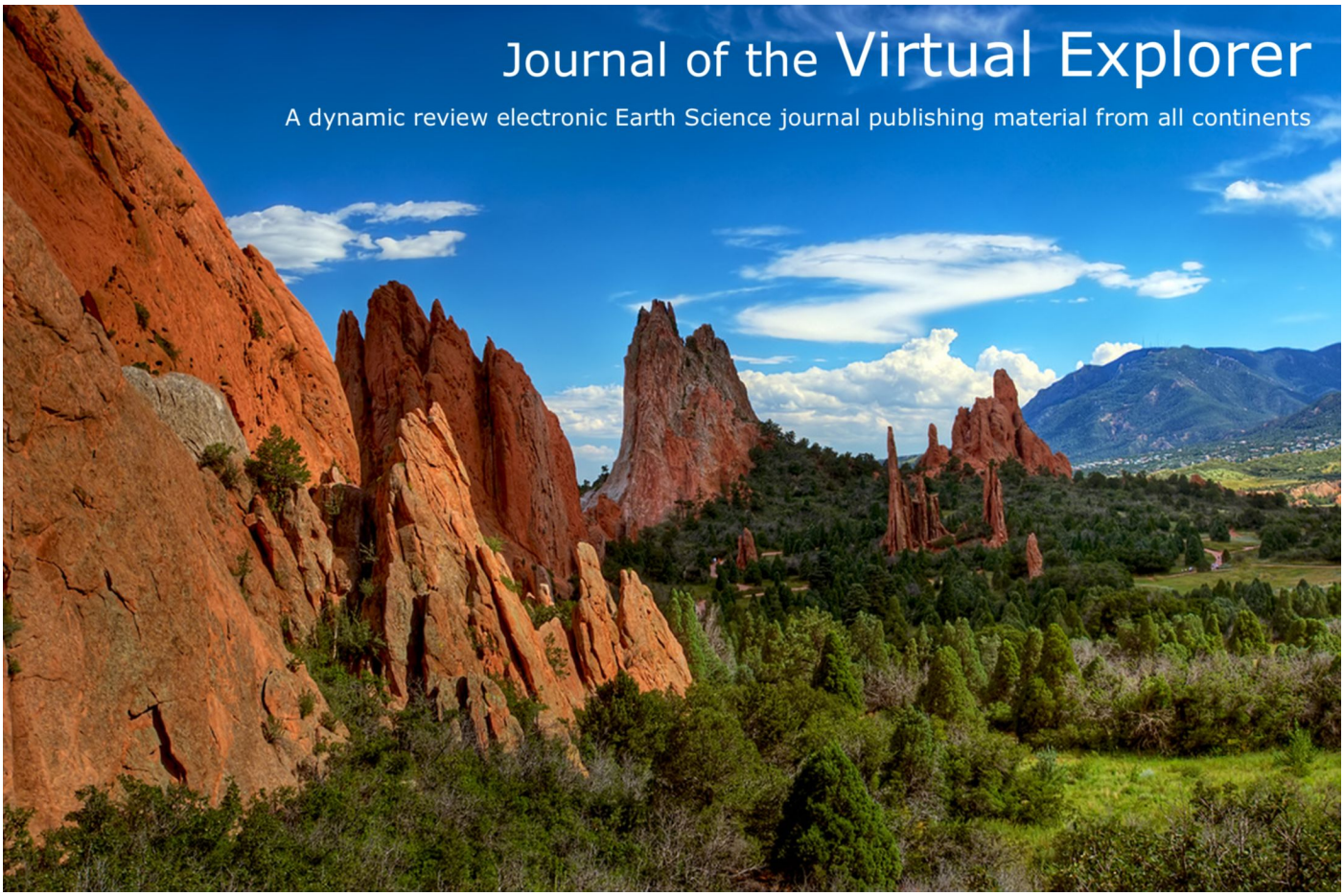

The lithosphere in Italy: structure and seismicity

Enrico Brandmayr, Reneta Blagoeva Raykova, Marco Zuri, Fabio Romanelli, Carlo Doglioni, Giuliano Francesco Panza

Journal of the Virtual Explorer, Electronic Edition, ISSN 1441-8142, volume **36**, paper 1
In: (Eds.) Marco Beltrando, Angelo Peccerillo, Massimo Mattei, Sandro Conticelli, and Carlo Doglioni, The Geology of Italy, 2010.

Journal of the Virtual Explorer, 2010
Volume 36
Paper 1
http://virtualexplorer.com.au/

The lithosphere in Italy: structure and seismicity

Enrico Brandmayr
Department of Earth Sciences, Via Weiss 4, 34127, University of Trieste, Italy. *Email: enrico.brandmayr@gmail.com*

Reneta Blagoeva Raykova
1. The Abdus Salam International Centre for Theoretical Physics, Strada Costiera 11, 34014 Trieste, Italy.
2. Istituto Nazionale di Geofisica e Vulcanologia – Sezione di Bologna, Via D. Creti 12, I-40128 Bologna, Italy

Marco Zuri
Department of Earth Sciences, Via Weiss 4, 34127, University of Trieste, Italy.

Fabio Romanelli
1. Department of Earth Sciences, Via Weiss 4, 34127, University of Trieste, Italy.
2. The Abdus Salam International Centre for Theoretical Physics, Strada Costiera 11, 34014 Trieste, Italy.

Carlo Doglioni
Department of Earth Science, Sapienza University, 00185 Rome, Italy.

Giuliano Francesco Panza
1. Department of Earth Sciences, Via Weiss 4, 34127, University of Trieste, Italy.
2. The Abdus Salam International Centre for Theoretical Physics, Strada Costiera 11, 34014 Trieste, Italy.
Email: panza@units.it

Abstract: We propose a structural model for the lithosphere-asthenosphere system for the Italic region by means of the S-wave velocity (V_S) distribution with depth. To obtain the velocity structure the following methods are used in the sequence: frequency-time analysis (FTAN); 2D tomography (plotted on a grid 1°×1°); non-linear inversion; smoothing optimization method. The 3D V_S structure (and its uncertainties) of the study region is assembled as a juxtaposition of the selected representative cellular models. The distribution of seismicity and heat flow is used as an independent constraint for the definition of the crustal and lithospheric thickness. The moment tensor inversion of recent damaging earthquakes which occurred in the Italic region is performed through a powerful non-linear technique and it is related to the different rheologic-mechanic properties of the crust and uppermost mantle.

The obtained picture of the lithosphere-asthenosphere system for the Italic region confirms a mantle extremely vertically stratified and laterally strongly heterogeneous. The lateral variability in the mantle is interpreted in terms of subduction zones, slab dehydration, inherited mantle chemical anisotropies, asthenospheric upwellings, and so on. The western Alps and the Dinarides have slabs with low dip, whereas the Apennines show a steeper subduction. No evidence for any type of mantle plume is observed. The asymmetric expansion of the Tyrrhenian Sea, which may be interpreted as related to a relative eastward mantle flow with respect to the overlying lithosphere, is confirmed.

Citation: 2010. The lithosphere in Italy: structure and seismicity. In: (Eds.) Marco Beltrando, Angelo Peccerillo, Massimo Mattei, Sandro Conticelli, and Carlo Doglioni, *Journal of the Virtual Explorer*, volume **36**, paper 1, doi: 10.3809/jvirtex.2009.00224

Paper Status

Paper is in dynamic review. Readers are invited to submit comments to the author and cc: team@virtualexplorer.com.au.

Introduction

The geodynamic evolution of Italy and the Mediterranean has been controlled by the Mesozoic Tethyan rifting and the later Tertiary subduction zones. The Permian-Mesozoic rifting developed separating Europe from Africa, and possibly some smaller intervening microplates. At the same time, toward the east, the Cinmerian NE-directed subduction zone was operating in the eastern Mediterranean-Asian area. The rifting in the Mediterranean evolved on a lithosphere previously thickened by the Paleozoic orogens. The stretching of the lithosphere locally evolved to oceanization in some areas of the Mediterranean (Ligure-Piemontese, Valais, Pennidic zone, eastern Mediterranean), and generated articulated continent-ocean transitions (i.e., passive continental margins) with undulated shapes. During the early Cretaceous, the Alpine subduction initiated to transfer some oceanic basins underneath the Adriatic-African plates. Collision possibly started during the Eocene. At a later stage, possibly during the Eocene-Oligocene, the opposite Apennines subduction initiated along the retrobelt of the Alps where oceanic or thinned continental lithosphere was present. The Alpine and Apennines orogens involved the passive margin sequences into their accretionary prisms. Most of the oceanic lithosphere was consumed into subduction, and only some small fragments of oceanic suites have been sandwiched into the belts. The oceanic crust formed during the expansion was almost totally assimilated in the subduction and dragged deep in the mantle, although it is possible to see its fragments involved in the collision now present in the Western Alps and North-western Apennines as ophiolites. The crust involved in the collisional process got thicker and thicker, uplifting for isostatic adjustment, thus starting the Alpine orogenic process. The deformation in the Alps started first in the Adriatic margin (African promontory). The European continental margin and the related sedimentary prism deformed last, thrusting over the European foreland to complete the generation of the Alpine orogen. At the same time, there were other active subductions, like the north-eastward directed subduction of the Adriatic plate below Eurasia (along the Dinarides) and westward subduction below the Apennines. In this belt, the slab retreat generated a different style of orogen, with a rather lateral growth, lower topography, shallower decollement and deeper foredeep. In the hanging wall of the Apennines slab, a backarc basin opened to form the present western Mediterranean basins. During the backarc rifting, since about 20 Ma, a fragment of the European margin detached from the continent and, rotating counterclockwise by about 60°, moved the Sardinia-Corsica block south-eastward to its present position. Behind this movement the crust thinned, forming the Algerian-Provencal basin. Then, since about 15 Ma, to the east of the Sardinia-Corsica block, a new tensional process caused the opening of the Tyrrhenian basin (Gueguen *et al.* 1997; Carminati *et al.*, 2004). These rotations and expansions modified and completed the structure of the Apennines chain. Evidence of these processes are the Calabrian-Peloritan arc's reliefs, whose "Alpine" rocks represent a relict of alpine chain, "boudinated" and dragged inside the accretionary prism of Apennines during the eastward migration of the subduction hinge. The rifting accompanied the eastward retreat of the Apenninic subduction zone, and the slab retreat kinematically requires a contemporaneous eastward mantle flow, regardless of whether this is the cause or a consequence of the retreat (Doglioni *et al.*, 1999). Therefore, the Italian and Mediterranean mantle should have recorded this long history with relevant anisotropies. However, the debate about the geodynamic evolution of the Mediterranean area is still open.

The advantage of joining geophysical models with geological and petrological data in order to understand the complex evolution of Italic region is discussed in Panza *et al.* (2007a) which presents a reliable model of the Tyrrhenian Sea. The study described, for the first time, a very shallow crust–mantle transition and a very low S-wave velocity (V_S) just below it, in correspondence of the submarine volcanic bodies (Magnaghi, Marsili and Vavilov) indicating the presence of high amounts of magma. Panza *et al.* (2007b) integrated crustal geological and geophysical constraints with the V_S models along the TRANSMED III geotraverse. As a result a new model of the mantle flow in a backarc setting, which first reveals an easterly rising low-velocity zone (LVZ) in the active part of the Tyrrhenian basin, is obtained, thus an upper mantle circulation in the Western Mediterranean is suggested. This upper mantle circulation, mostly easterly directed, affects the boundary between upper

asthenosphere (LVZ) and lower asthenosphere, which undulates between about 180 and 280 km. An explanation for the detected shallow, very low velocity mantle in the non-volcanic part of Tyrrhenian region is presented in Frezzotti *et al.* (2009). These anomalous layers were generated by the melting of sediments and/or continental crust of the subducted Adriatic-Ionian (African) lithosphere at temperatures above 1100°C and pressure greater than 4 GPa (130 km). The resulting low fractions of carbonate-rich melts have low density and viscosity and can migrate upward forming a carbonated partially molten CO_2-rich mantle in the depth range from 130 to 60 km. Carbonate-rich melts upwelling to depth less than 60-70 km induce massive outgassing of CO_2 that can migrate and be accumulated beneath the Moho and within the lower crust.

This article analyzes the central Mediterranean mantle through surface waves tomography and the comparison of crustal and mantle structure with seismicity. The systematic inversion of recent damaging earthquakes that have occurred in the Italic region is performed through a powerful non-linear technique named INPAR (Guidarelli and Panza, 2006, and references therein). The space distribution of such events is analyzed and related to the different rheologic-mechanic properties of the upper and lower crust and uppermost mantle. This led to a drastic relocation and change of mechanism of a major event of the Umbria-Marche 1997 seismic sequence with respect to the solution reported by Centroid Moment Tensor (CMT) and Regional Centroid Moment Tensor (RCMT) bulletins, providing new constraints to the geological setting and local stress field.

We contribute to the debate on the geodynamical evolution of the Italic region with a cellular model of the lithosphere-asthenosphere system of the area in terms of V_S distribution with depth (V_S-depth) structure. The model presented in this work is constrained with independent studies concerning Moho depth (Dezes and Ziegler, 2001; Grad and Tiira, 2008; Tesauro *et al.*, 2008), seismicity-depth distribution (ISC, 2007), V_P tomographic data (Piromallo and Morelli, 2003) and other independent information as heat flow (Hurting *et al.*, 1991; Della Vedova *et al.*, 2001) and gravimetric anomaly (ISPRA, ENI, OGS, 2009) data.

Methodology

Surface wave dispersion data and tomography

The surface wave dispersion data are used in the present study to investigate the V_S structure in the Italic region. The following methods are applied in the sequence: (a) frequency-time analysis, FTAN (Levshin *et al.*, 1989, and references therein), to measure group-velocity dispersion curves of the fundamental mode of Rayleigh waves; (b) two-dimensional tomography (Yanovskaya, 2001, and references therein) to map the distribution of group and phase velocities of Rayleigh waves, plotted on a grid 1°×1° to compile the cellular dispersion curves; (c) non-linear inversion (Panza, 1981, and references therein) of the assembled cellular dispersion curves to calculate the set of accepted models for each cell; (d) smoothing optimization algorithms (Boyadzhiev *et al.*, 2008) to choose the representative model for each cell and thus to define, for the Italic region, the three-dimensional V_S model and its uncertainties.

The FTAN is an interactive group velocity-period filtering method that uses multiple narrow-band Gaussian filters and maps the waveform record in a two-dimensional domain: time (group velocity) -frequency (periods). The measurement of group velocity of Rayleigh and/or Love waves is performed on the envelope of the surface-wave train and can be robustly measured across a broad period band, from fractions of seconds to hundreds of seconds (e.g. Chimera *et al.*, 2003; Guidarelli and Panza, 2006). Seismic records from national and international seismic networks are analyzed by FTAN to study the velocity structure in the broad Mediterranean region. The information about the hypocenters of the events (location, depth, and origin time) is collected from NEIC (2003) or ISC (2007). The length of most of the epicenter-to-station paths considered does not exceed 3000 km in order to have, as much as possible, reliable measurements of group velocity at short and intermediate periods. After group-velocity measurements, all the curves are linearly interpolated and sampled at the set of predefined periods. In addition group-velocity measurements available in the literature have been considered. The penetration depth of our dataset is increased (Knopoff and Panza, 1977; Panza, 1981) considering published phase-velocity measurements for Rayleigh waves that span over the period range from about 15 s – 20 s to about 150 s.

The two-dimensional tomography based on the Backus–Gilbert method is used to determine the local values of the group and/or phase velocities for a set of periods, mapping the horizontal (at a specific period) and vertical (at a specific grid knot) variations in the Earth's structure. From these tomographic maps, local values of group and phase velocities are calculated on a predetermined grid of 1°×1°, for a properly chosen set of periods, in the ranges from 5 s to 80 s for group velocities and from 15 s to 150 s for phase velocities. The choice of the set of periods is based on the vertical resolving power of the available data, as determined by the partial derivatives of dispersion values (group and phase velocities) with respect to the structural parameters (Panza, 1981). The lateral resolution of the tomographic maps is defined as the average size, L, of the equivalent smoothing area and its elongation (Yanovskaya, 1997) and hence it is not necessary to perform check board or similar tests.

The local dispersion curves are assembled at each grid knot from the tomographic maps. The average size L and its stretching is used as a criterion for the assemblage of the local dispersion curves. At each period, the group and/or phase velocity value is included in the dispersion curve if L is less than some limits: for group velocity L_{max} is 300 km at the period of 5 s and increases to 600 km at 80 s; for phase velocity L_{max} is 500 km at the period of 15 s and reaches a value of 800 km at 80 s; the stretching of the averaging area of all considered values is less than 1.6. Hence the local dispersion curves have a different period range and take into account only the dispersion values sufficiently well resolved.

Each cellular dispersion curve is calculated as the average of the local curves at the four corners of the cell. The single point error for each value at a given period is estimated as the average of the measurement error at this period and the standard deviation of the dispersion values at the four corners. If, at a given period, the cell is crossed by few wave paths, and, according to the L_{max} criterion, the dispersion value at a corner of the cell is not available, the value of the single point error is doubled. The value of group velocity at 80 s is calculated as an average between our tomography results and the global data from the study of Ritzwoller and Levshin (1998). The single error at this period for group velocity is estimated as the r.m.s. of the errors of our data and those of the global data set. The r.m.s. for the set of dispersion curves (group or phase velocity) are routinely estimated as 60-70% of the average single point error of the specific cellular curve (Panza, 1981; Panza *et al.*, 2007a). The assembled cellular dispersion curves span over a varying period range according to the available reliable data.

The non-linear inversion

The non-linear "hedgehog" inversion method is applied to obtain the V_S models for cells sized 1°×1° in the Italic region using the compiled cellular dispersion curves. To solve the inverse problem, the structural model of each cell has to be replaced by a finite number of numerical parameters, and, in the elastic approximation, it is divided into a stack of homogeneous isotropic layers (Fig. 1). The method is a trial-and-error optimized Monte Carlo search and the layer parameters (thickness, V_P, V_S, and density ρ can vary or be constant during the inversion procedure. For each dispersion curve, digitized at N points, the parameter's steps δP_j (where j is the number of parameters, equal to 10 in our case) are defined following Knopoff and Panza (1977) and Panza (1981) and they are minima subject to the condition:

Figure 1. Earth's model adopted for the inversion scheme.

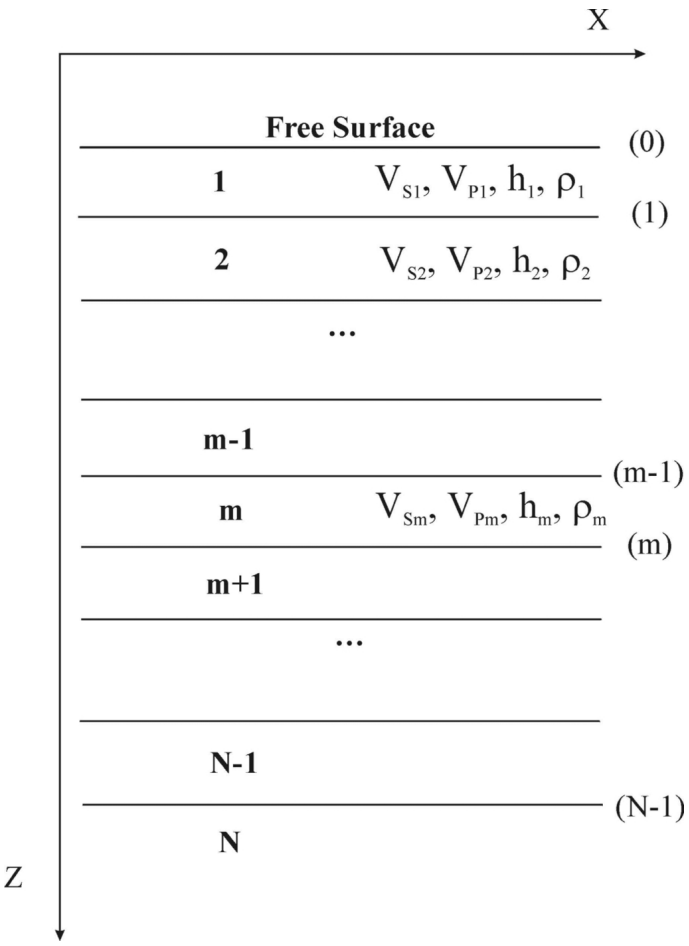

The modeling of the Earth's structure in hedgehog inversion by laterally-homogeneous isotropic plane layers. The physical properties V_S, V_P, thickness (h), density(ρ) of each layer can be independent (i.e. the variable parameters that can be well resolved by the data), dependent (i.e. in some fixed relation with inverted parameters) or fixed (i.e. during the inversion the parameter is held constant accordingly to independent geophysical evidence). Upper crust layers (i.e. layers 1, 2, …) are fixed according to independent data. Parameterized layers (i.e. layers m-1,..., m+1) are inverted, while the deep structure (i.e. layers N-1, N, …) are fixed according to global models.

$$\sum_{j=1}^{N}\left(\frac{\partial V(T_i)}{\partial P_j}\right)\cdot\delta P_j=\sigma(T_i) \qquad (1)$$

where $V(T_i)$ is the group or phase velocity at period T_i and $\sigma(T_i)$ is the relevant standard deviation. The uncertainties of the accepted model are defined as ± half of the relevant parameter's step.

The group and phase velocities of the Rayleigh waves (fundamental mode) are computed for each tested structural model. The model is accepted if the difference between the computed and measured values at each period are less than the single point error at the relevant period and if the r.m.s. values for the whole group and phase velocity curves are less than the given limits.

The structure is parameterized taking into account the resolving power of the data and *a priori* geophysical information. The resolving power of dispersion measurements is only indirectly connected with the lateral variations of the structural models and identical dispersion properties do not necessarily correspond to equal structures (see Appendix A). *A priori* independent information about the crustal parameters of each defined cell can be introduced in the inversion procedure to improve the resolving power of the tomographic data (Panza and Pontevivo, 2004; Pontevivo and Panza, 2006). A similar conclusion is reached by Peter *et al.* (2008): in the absence of an accurate crustal model, the retrieved upper mantle structure is dubious down to about 200 km of depth.

According to the values of the partial derivatives of the group and phase velocities for Rayleigh waves with respect to structural parameters (Urban *et al.*, 1993), the assembled cellular dispersion data, in the period ranges from 5 s to 150 s for group velocity and from 15 s to 150 s for phase velocity, allows us to obtain reliable velocity structure in the depth range from 3 km – 13 km to about 350 km. In each cell, the Earth's structure is modeled by 19 layers down to the depth of about 600 km: the uppermost five layers have properties fixed *a priori*, using independent literature information specific for each cell; the following five layers have variable V_S, V_P, thicknesses and if necessary - density; in the eleventh layer V_P, V_S, and density are fixed while the thickness varies in such a way that the whole stack of eleven layers has a total thickness, H, equal to 350 km; below 350 km of depth there are eight layers, of Poissonian material, with constant properties common to all cells. The structure below 350 km is taken from the average model for the whole Mediterranean, EurID database, of Du *et al.* (1998). The EurID database is based upon existing geological and geophysical literature, it incorporates topographic and bathymetric features and it has been proven to be quite consistent with several broad-band waveforms. The use of global models, e.g. ak135 (Kennett *et al.*, 1995), for the structure below 350 km does not introduce any significant difference in the calculated dispersion curves (Raykova and Panza, 2010), thus does not affect our inversion

results. In each cell, the thickness of the fixed uppermost crustal structure depends on the lower limit of the period range of the cellular dispersion curves, and varies from about 3 km to 13 km. When the cell is located in a sea region, the thickness of the water layer is defined as a weighted average of the bathymetry and topography (online data from NGDC, 2003) inside the area of the cell. The thickness of the sediments is defined in a similar way from the map of Gennesseaux *et al.* (1998) or from the data given by Laske and Masters (1997). The structural data available from seismic, geophysical and geological studies in the region are used to fix the properties of the remaining upper crustal layers. The same information is considered in the parameterization of the five layers used to model the depth range from 3 km – 13 km to 350 km. Eleven parameters (P_j, j=1,10 and P_0) are used to define these five layers: five for the shear-wave velocity in each layer, five for the thickness of each layer, and P_0 for the V_P/V_S ratio. The independent available geophysical information is used to define the following parameters ranges: (1) Moho depth; (2) V_S in the crust ($V_S \leq 4.0$ km/s); (3) V_S in the mantle layers (4.0 km/s $\leq V_S \leq$ 4.8 km/s); (4) the total thickness of the parameterized structure cannot be greater than 350 km (the maximum depth of relevant penetration of our data). Nevertheless, the V_S ranges for crust and mantle represent globally valid rules that may not be satisfied in some specific complex cases. In the Alps, the maximum V_S in the crust is set to 4.10 km/s according to reported velocities for some crustal minerals (Anderson, 2007) and in the upper mantle beneath Tyrrhenian Sea, where a high percentage of melting is present (Panza *et al.*, 2007a), low mantle velocities ($V_S \leq 4.0$ km/s) are allowed.

Optimization algorithms

The non-linear inversion is multi-valued and a set of models is obtained as the solution for each cell. In order to summarize and define the geological meaning of the results, it is necessary to identify a representative model, with its uncertainties, for each cell. An optimized smoothing method, which follows the Occam's razor principle, is used to define the representative model for each cell with a formalized criterion. This method avoids, as much as possible, the introduction of artificial discontinuities in V_S models at the borders between neighboring cells and keeps the 3D structure as homogeneous as possible by minimizing the lateral velocity gradient. In this way, the dependence of the final model from the predefined grid is minimized. The method represents the models as velocity vectors with equal size (250 layers) for all sets of cellular solutions. The distance (divergence) *d* between two models (velocity vectors) w and v is defined as the standard Euclidean norm between two vectors:

$$\|w - v\| = \sum_{i=1}^{n} \sqrt{(w_i - v_i)^2} \quad (2)$$

where w_i and v_i are the S-wave velocities in the i^{th} layer and n is the number of layers in the models.

To take into account the contribution of the i^{th} layer thickness, each velocity value has been weighted with the ratio given by the correspondent layer thickness, h, over the total thickness of the structure, i.e. in the i^{th} layer the weighted velocity (v_{Wi}) is:

$$v_{w_i} = v_i \cdot \frac{h_i}{H} \quad (3)$$

Three quite different criteria for optimization have been developed that lead to the minimization of the lateral velocity gradient for the whole domain, or, in other words, to the smoothing of the shape of the global solution in all the study area Ω as much as possible.

The definitions of the criteria are as follows. (I) Local Smoothness Optimization (LSO): the optimized local solution of the inverse problem is the one that is searched for, cell by cell, considering only the neighbors of the selected cell and fixing the solution as the one which minimizes the norm between such neighbors. (II) Global Flatness Optimization (GFO): the optimized global solution of the inverse problem with respect to the flatness criterion is the one with minimum global norm in-between the set of global combinations G(Ω). (III) Global Smoothness Optimization (GSO): the optimized global solution of the inverse problem with respect to the smoothness criterion is the one with minimum norm in-between all the members of the subset Γ(Ω).

The LSO follows the principle of minimal divergence in the models. The search starts from the cell where the average dispersion of the cellular models is minimal, i.e. the accepted solutions in this cell are the densest in the parameter space and therefore the potential systematic bias introduced by the choice is minimized. The LSO fixes, as the representative solution of the processed cell $\delta_{i,j}$,

the cellular model that minimizes the norm between the neighbour cells $\delta_{i\pm1,j\pm1}$ (i.e. cells with one side in common). Once a solution is chosen in the running cell, it is fixed and the search continues by applying the procedure to one of the neighbouring cells, not yet processed, and with the smallest average dispersion of the cellular models. The LSO follows the direction of "maximum stability" in the progressive choice of the representative solution of the cells until the whole investigation domain is explored.

The GSO is based on the idea of close neighbours (local smoothness) extended, in a way, to the whole study domain. The method consists of two general steps. The first step extracts a suitable subset $\Gamma(\Omega)$ from $G(\Omega)$, namely the global combination u belongs to $\Gamma(\Omega)$ if and only if:

$$\|u_{i,j} - u_{i\pm1,j\pm1}\| = \min(\|u_{i,j} - \tilde{u}\|) \quad (4)$$

where $\tilde{u} \in \delta_{i\pm1,j\pm1}$. In other words $\Gamma(\Omega)$ contains all global combinations with close neighbouring components. Then we select, as the best solution in $G(\Omega)$ with respect to the smoothness criteria, the member of $\Gamma(\Omega)$ with least global norm, i.e. we apply the flatness criterion to $\Gamma(\Omega)$ and not to the entire $G(\Omega)$.

The GFO is based on the concept of maximum flatness among the whole domain Ω. It records, by iterative steps for every row starting from the right border of the domain Ω, each combination of solutions in the processing row which has minimal norm with the combinations in the previous processed row. Then, in the last step, GFO selects the combinations which have the minimal global norm, with respect to flatness criterion, among the global set $G(\Omega)$.

Due to the different way of action and computing time necessary to perform GFO and GSO, we applied the three smoothing algorithms hierarchically in the region of Alps (Boyadzhiev *et al.*, 2008). We perform LSO and GSO, which are the fastest methods acting on the smoothing criterion basis, on the whole area of the Alps. The application of these two methods preserves some local features which may be flattened by GFO, according to its acting criterion. Then, in order to reduce the dependence from the starting cell that affects LSO, the common solution to LSO and GSO are selected and fixed during the performed GFO. This sequential execution of the smoothing algorithms reduces the computing time and concentrates the effort on that portion of Ω in which the solutions chosen by LSO and GSO differ.

Since the non-linear inversion and its smoothing optimization guarantee only the mathematical validity of the solution of the inverse problem, the optimization procedure can be repeated whenever necessary, including additional geophysical constrains, such as Moho depth, seismic energy distribution versus depth, presented magmatism, heat flow, etc., until the appraisal of the selected models against well-known and constrained structural features gives a result comparable with the model's uncertainties (see section "Discussion").

The resulting three-dimensional V_S structure of the study region is juxtaposed against the selected representative one-dimensional cellular models. The steps used in the parameterization of the non-linear inversion obey condition (1), therefore they can be used to define the uncertainties of each cellular model (Panza *et al.*, 2007a). The representative cellular solution gives, for each inverted layer, the preferred value of V_S and thickness with uncertainties equal, as a rule, to ±1/2 of the relevant parameter (V_S or thickness) step. The *a priori* information is taken into account when the uncertainties of the representative solution are specified. Therefore, the variability range of the inverted parameters can turn out to be smaller than the step used in the inversion and the exact value given by the representative solution does not necessarily fall in the middle of its uncertainty range.

Independent geophysical constraints

The resulting representative cellular models are appraised and constrained using independent studies concerning Moho depth (Dezes and Ziegler, 2001; Grad and Tiira, 2008; Tesauro *et al.*, 2008), seismicity-depth distribution (ISC, 2007), V_P tomographic data (Piromallo and Morelli, 2005) and other independent information as the heat flow (Hurting *et al.*, 1991; Della Vedova *et al.*, 2001) and gravimetric anomaly (ISPRA, ENI, OGS, 2009).

The data from Dezes and Ziegler (2001), Tesauro *et al.* (2008), and Grad and Tiira (2008) are used to define the range of Moho depth for each cell. The Moho depth, with its uncertainties, is compared for each cellular model with the depth range derived from the literature. Where the value indicated by our models is out of the range, additional constraints are used (see section "Discussion").

The depth distribution of seismicity is used as an additional criterion for appraisement of the cellular models. The revised ISC (2007) catalogue for the period 1904–June 2005 is used and for each cell we compute several histograms, grouping hypocentres in depth intervals. The depth grouping considers the uncertainties of the hypocentre's depth calculation: 4 km for the crustal seismicity and 10 km for the mantle seismicity. The computed histograms are the following: (a) distribution of the logarithm of earthquake's number per depth intervals (logN-h): (b) distribution of the logarithm of total energy released by the earthquakes per depth intervals (logE-h); (c) distribution of the logarithm of product of energy released by the earthquakes per depth intervals (log∏E-h). Each of these three depth distributions is generated for two selections of the events: all events in the considered catalogue and all events with depth not fixed during hypocenter calculations in order to reduce the influence of "standard" depths, as 33 km, in the histogram construction. The logN-h distribution gives an estimation of the material fragility in the relevant depth interval: high earthquake's frequency is related to more brittleness materials. Similar distributions are used in the studies of Meletti and Valensise (2004) and Ponomarev (2007) but this kind of earthquake frequency distribution does not evidence the presence of strong single events. The logE-h distribution valuates the strangeness of the material in the relevant depth interval: high energy release is relevant to high energy accumulation in strong materials. This kind of seismic energy distribution is used by Panza *et al.* (2007a) but some strong badly located events can bias the results. The log∏E-h distribution gives an integral characteristic of the seismicity in the relevant depth interval, since the product of energy is proportional to the number of earthquakes and relevant energy release. Let us consider two events in a depth interval, with energy release of E_1 and E_2 respectively, where E_1=aE_2. The log∏E for this interval is the following:

$$\log(E_1 \cdot E_2) = \log(E_1) + \log(E_2) = \log(aE_2) + \log(E_2) = \log(a) + 2\log(E_2) \quad (5)$$

The seismicity distribution presented in this way is used by Panza and Raykova (2008) to define the Moho depth in the Italic region.

The logN-h distribution is calculated using all events from ISC catalogue (with and without depth estimated). For energy calculation (logE-h and log∏E-h) the relation of Richter (1958) $\log E = 1.5M_S + 11.4$ is used considering all events from ISC catalogue with indicated magnitude. The value of M_S is either directly taken from the ISC catalogue or computed from currently available relationships between M_S and other magnitudes (Peishan and Haitong, 1989; Gasperini, 2002; Panza and Raykova, 2008). Some examples for computed seismicity-depth distributions are shown and discussed in section "Discussion".

The information about heat flow (Hurting *et al.*, 1991; Della Vedova *et al.*, 2001) is used to define the nature of some relatively shallow layers (down to about 80 km of depth). A high heat flow likely indicates the presence of magma reservoirs with low V_S at shallow depths. A low heat flow usually requests cold mantle (relatively high V_S) and thick crust.

Independent information about gravimetric anomaly (ISPRA, ENI, OGS, 2009) together with heat flow data is used in the interpretation of the lithosphere-asthenosphere structure along several sections (see section "Discussion").

The V_P tomographic data of Piromallo and Morelli (2003) are used to reduce the uncertainty range of our V_S models in the construction of the cellular database.

Non-linear inversion of moment tensor: INPAR method

The determination of the moment tensor, i.e. of the source mechanism of a seismic event from its complete waveforms, is a non-linear problem. Nevertheless, its determination is of fundamental importance to determine the properties of seismic sources, and straightforward for the comprehension of the local stress field acting in a given tectonic region.

Several methods were developed, linear and non-linear, from body waves, surface waves or complete waveforms, from a regional or global event. Some of them are routinely applied and published in bulletins shortly after a seismic event. However, all these methods have different accuracies and resolving power.

We analyze, in detail, the non-linear method named INPAR (INdirect PARameterization), developed at the Department of Geosciences, University of Trieste (Sileny *et al.*, 1992; Sileny, 1998).

The INPAR method for the inversion of moment tensor, that adopts a point-source approximation, is a sophisticated non-linear method using the dominating part of

complete waveforms from events at regional distances (up to 2500 km), in this way maximizing the signal-to-noise ratio. It consists of two steps, the former linear, the latter non-linear.

The k^{th} component of displacement at the surface determined by equivalent forces in the point-source approximation is the convolution product of moment tensor and Green's function spatial derivatives (Aki and Richards, 1980):

$$u_k(t) = M_{ij} * G_{ki,j}(t) \quad (6)$$

The Green's functions represent the response of the medium to singlet sources with Dirac-delta time dependence.

In the first step, Green's functions are extracted from signals to calculate the time derivatives of the six independent components of the moment tensor (hereafter MTRF) (Panza, 1985; Florsch *et al.*, 1991; Panza *et al.*, 2000), in this case with a time dependence given by Heaviside (step) function. Computing the MTRFs from Green's functions does not require an *a priori* source model. Since a bad location of the focus may strongly affect the results of the inversion, INPAR performs, whenever necessary, a re-location of the focus within a fixed volume around the available location. For intermediate coordinates within this volume the base functions, i.e. the medium response to a seismic source modeled by an elementary single source with the time dependence given by Heaviside function, are computed interpolating the base functions computed at the corners of the volume itself. From base functions, the synthetic seismograms are computed and are compared with observed ones: the L^2 norm of synthetic and observed seismograms is minimized to determine the new focus location.

In the next non-linear step, the MTRFs are factorized in a time constant moment tensor m_{ij} and a corresponding source time function f(t):

$$\frac{\partial M_{ij}(t)}{\partial t} = m_{ij} \cdot f(t) \quad (7)$$

assuming the same time dependence for all moment tensor components, i.e. a rupture mechanism constant in time.

The "predicted" values of the MTRFs, $m_{ij} \cdot f(t)$, are matched to the "observed" MTRFs (obtained as the output of the first step of the procedure). Thus, by introducing MTRFs in the first step, the problem of matching the seismograms is transformed to the problem of matching the MTRFs. This allows the reduction of the equations system for the searched source parameters, since the MTRFs are always six, while seismograms can be more than six. In order to reduce the errors coming from the poor knowledge of the structural inhomogeneities of the epicenter-station profile, which can cause scattering, only the correlated parts of the MTRFs are taken into account (Kravanja *et al.*, 1999).

Additional constraints, such as the positivity of the source time function and, whenever available, consistency with polarities, are posed. After several iterations, the focal mechanism is obtained and reduced to the best double couple in case of tectonics events. In this way the volume components, which are often artefacts of the inversion process, are discarded (Kravanja *et al.*, 2000).

INPAR is particularly suitable for determining the foci of shallow events, due to the possibility to use waveforms of relatively short period (down to 10 s). Theoretically, the seismic moment tensor cannot be univocally determined from surface waves signals whose wavelength significantly exceeds the source depth (Bukchin and Mostinskii, 2007), since two components of the moment tensor, M_{zx} and M_{zy}, excite a Green's function vanishing at the free surface. Because of this, the CMT and RCMT methods, which respectively use body and surface waves at periods greater than 35 s, usually fix shallow events at depths of 10 km the former and 15 km the latter.

The correct determination of the hypocentral parameters of a tectonic event is of crucial importance for a reliable understanding of the geodynamic context in which the event occurred. The information coming from moment tensor inversion can be inserted in the tectonic picture obtained from tomography to better constrain it (see section "Discussion").

Further development: cellular database

A cell-by-cell database has been compiled to compare the obtained results with some independent data (V_P, attenuation and density) to enable an easier way to access the data. All collected information for each cell is stored in a table. An example of the database for cell 42.5N 13.5E (b3, L'Aquila) is given in Table 1.

Table 1. Cellular database

H	ρ	V_P	V_S	Q_P	Q_S	Z	Lon	Lat	ΔV_S+	ΔV_S-	ΔH+	ΔH-	V_P/V_S
1.2	2.30	2.70	1.55	440	200	1.20	13.50	42.50	0.00	0.00	0.00	0.00	1.74
0.8	2.50	3.70	2.13	418	190	2.00	13.50	42.50	0.00	0.00	0.00	0.00	1.74
1.5	2.60	5.35	3.10	418	190	3.50	13.50	42.50	0.00	0.00	0.00	0.00	1.73
12.0	2.75	5.70	3.30	330	150	15.50	13.50	42.50	0.05	0.05	1.50	1.50	1.73
20.0	2.80	6.40	3.70	198	90	35.50	13.50	42.50	0.15	0.10	5.00	5.00	1.73
60.0	3.30	7.90	4.40	176	80	95.50	13.50	42.50	0.15	0.00	0.00	15.00	1.80
60.0	3.30	8.00	4.35	176	80	155.50	13.50	42.50	0.00	0.15	25.00	0.00	1.84
110.0	3.30	8.70	4.60	220	100	265.50	13.50	42.50	0.00	0.20	0.00	25.00	1.89
84.5	3.60	8.95	4.75	330	150	350.00	13.50	42.50	0.00	0.00	0.00	0.00	1.88

The V_P data are taken from Piromallo and Morelli (2003) where a P-wave tomography study of the whole Mediterranean region is provided on a grid of 50 km in both horizontal and vertical directions down to a depth of 1000 km. The V_P data are given in a coordinate system which is rotated with respect to the geographical one. The prime meridian in the rotated system is 10° W, while the "rotated equator" is the great circle crossing the prime meridian at 45° N. To complete our database, the V_P data are averaged to obtain a single set of V_P values for each of our 1°×1° cells. The averaged data are interpolated linearly to obtain the value of V_P at the centre of each layer of our cellular structures. The V_P data are considered only for the mantle layers down to a depth of 350 km, as the considered P-wave tomography poorly resolves the upper crustal structure.

The calculated V_P value for each layer in our cellular models permits to reduce the uncertainty ranges of V_S in the mantle, as far as the V_P/V_S ratio in the mantle is kept as close as possible to 1.82 (Kennett *et al.*, 1995).

The density data are taken from Farina (2006) where the gravity inversion method is applied to model the density along a set of sections in the Italic region and surroundings. About 30% of our cells are not modelled by Farina (2006). The densities in some of these cells are obtained by linear interpolation of the density in the neighbouring cells (e.g. cells C3, B6, A5). Where the interpolation was not possible, the density data are those used as fixed input in the non-linear inversion.

The database is completed with S-wave attenuation (Q_S) data given in the recent studies of Martinez *et al.* (2009, 2010) for the Mediterranean at latitude less than 45°N. Using averaging and linear interpolation, the value of Q_S is calculated for the centre of each layer in our cellular solutions. The Q_S data for the rest of the cells are taken from Craglietto *et al.* (1989). The values of P-wave attenuation (Q_P) has been derived using the relation $Q_P = 2.2Q_S$ (Anderson, 2007). All V_P and V_S values are rounded to 0.05 km/s, according to the precision of our modelled data.

In some cases a V_S inversion is modelled in the upper 20 km. Whether this is a real structural feature or an artefact of the inversion will be a matter to be settled performing the inversion using the receiver functions data to better constrain the upper fixed crust.

Results

The study region is presented in Figure 2 and the obtained representative 125 cellular solutions are shown in Figures 3-8. The cellular models are presented as V_S-depth distributions. The values of V_S are color-coded and the uncertainty range for each of the parameterized layers is given. Some values of the V_S are omitted in the figures but full models are listed in Appendix B. The uncertainty of the layer's thickness is given by hatched rectangles. The cellular seismicity (magnitude ≥ 3.0, ISC, 2007) is indicated by red dots. The cell's alphanumerical label is given at the bottom of each model.

Figure 2. The studied region.

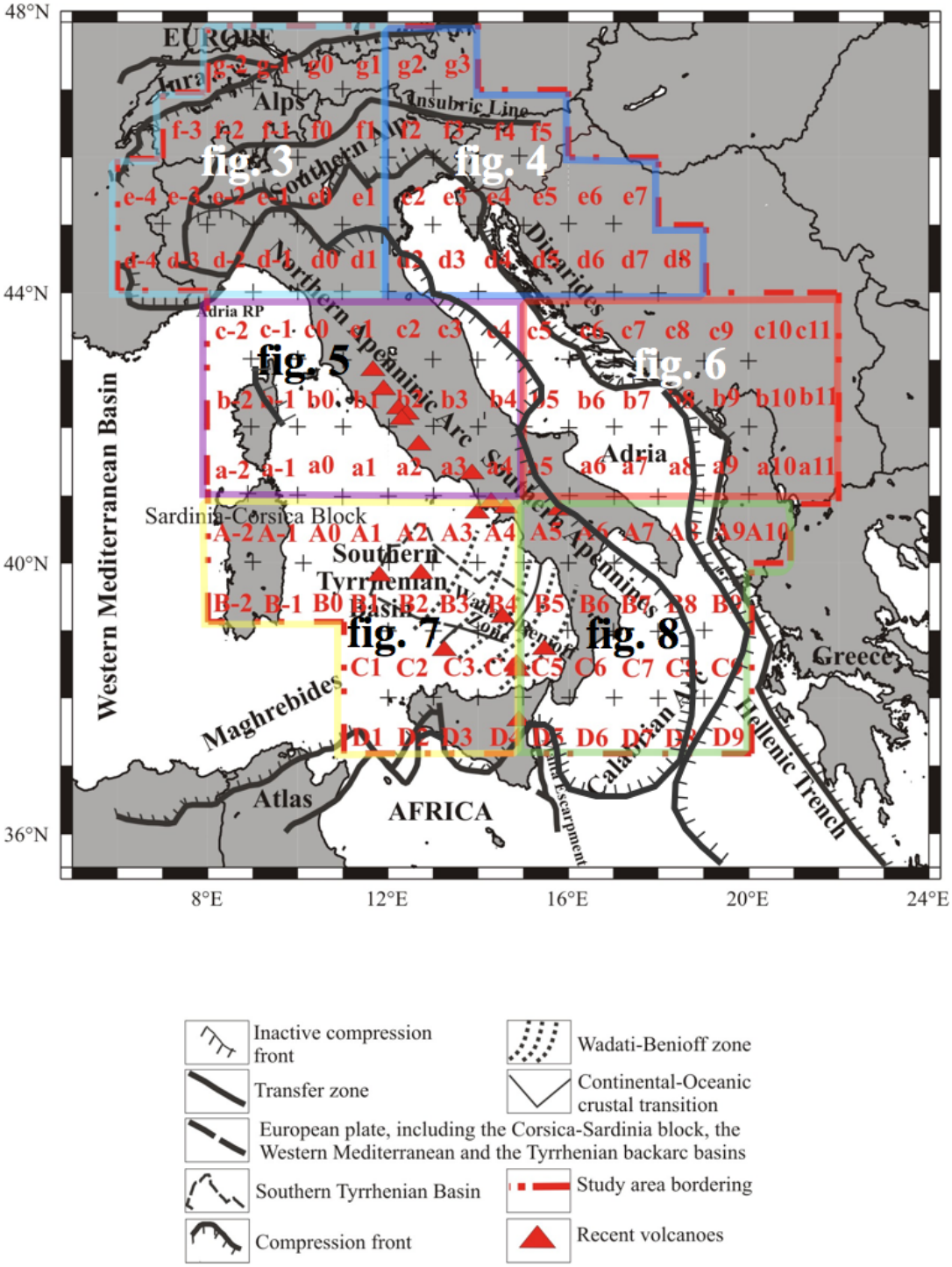

The Italic region with studied cells sized 1°x1°. The main tectonic features and volcanoes are indicated. The colored polygons indicate the grouping of cells which V_S models are presented in Figs. 3-8.

Several definitions are used in the following description of the V_S structures: i) lithospheric mantle (LID); ii) soft mantle lid; iii) asthenospheric low velocity zone (LVZ); iv) mantle wedge. The LID is the portion of the

mantle with high seismic wave velocity and high density. It still has brittle behavior (V_P between 7.5 and 8.6 km/s; V_S lower than 4.9 km/s and generally higher than 4.35 km/s; density between 3.0 and 3.4 g/cm^3). The soft mantle lid is a layer of lithospheric mantle material with anomalous behavior and low seismicity, found right below the Moho discontinuity; this material is partially molten, with low V_S and relatively high density values. The origin of this high-percentage melt layer is not limited, nor directly bound, to subduction areas (V_P between 6.9 and 8.2 km/s; V_S lower than 4.35 km/s; density between 3.0 and 3.3 g/cm^3). The LVZ is an asthenospheric layer with low seismic wave velocity; it is present right below the LID or deeper, under faster asthenospheric layers (V_P between 7.9 and 8.6 km/s; V_S between 4.0 and 4.4 km/s; density between 3.1 and 3.5 g/cm^3). The mantle wedge is the portion of mantle material found between a subducting slab and the overriding lithosphere where plastic deformation occurs; in absence of this geodynamic setting mantle material with similar physical behavior has been simply described as "soft mantle". In this region, according to Van Keken (2003), hydrothermal uprising flow causes partial melting of subducting slab material due to dehydration.

LSO structural model of Italic region

Starting from the north-western margin (Fig. 3) of the study region we face a prominent crustal thickening from cell g-2, with a low V_S crust of 20 km depth lying on a 30 km thick soft mantle lid (V_S about 4.20 km/s) to cell g-1, where a fast crust (V_S about 4.10 km/s) extends down to 40 km depth. In both cells the underlying mantle is characterized by a 30-50 km thick lid (V_S about 4.65 km/s), lying above an asthenospheric layer extended from 90 to 160 km depth (V_S about 4.30 and 4.35 km/s respectively). In cells g0 and g1 a crust about 30 km thick (V_S about 3.70 km/s) lies above two lithospheric mantle layers (V_S about 4.40-4.45 km/s) extended down to 160-180 km of depth. Below them, an asthenospheric layer is present in both cells (V_S about 4.35 and 4.25 km/s respectively) down to 250 km depth.

Figure 3. Western Alps cellular model.

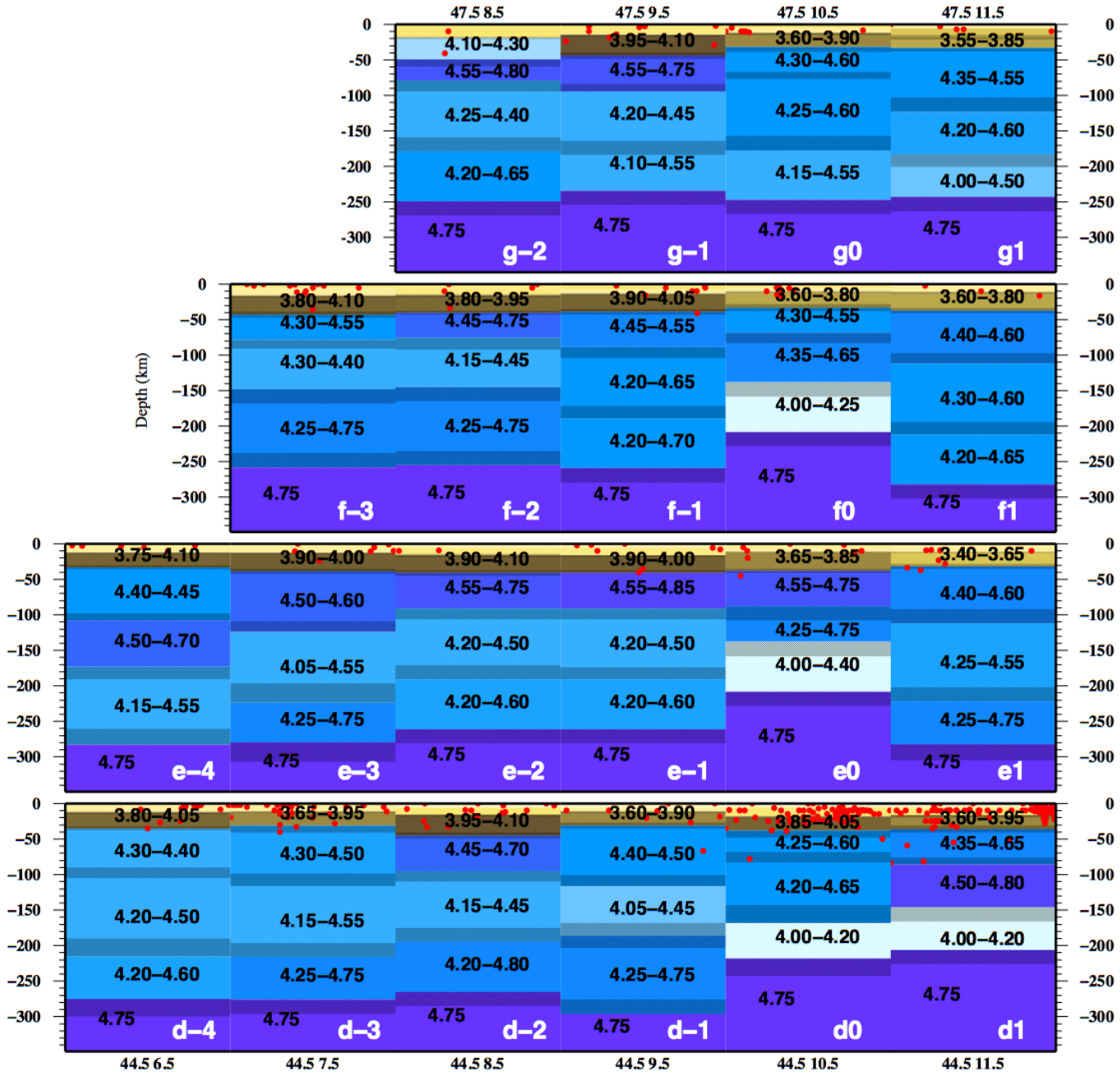

Cellular structural model extended down to 350 km depth for the western Alps area. Yellow to brown colors represent crustal layers, blue to violet colors indicate mantle layers. Red dots denote all seismic events collected by ISC with magnitude greater than 3 (1904-2006). For each layer V_S variability range is reported. For the sake of clarity, in the uppermost crustal layers the values of V_S are omitted. The uncertainty on thickness is represented by texture. All the values are given in Appendix B.

To the east (Fig. 4), in cells g2 and g3, the crust is about 30 km thick and lies on a 40-50 km thick soft mantle layer (V_S about 4.25 and 4.20 km/s, respectively). Below this layer we find in both cells a lid about 50 km thick (V_S about 4.55 km/s) down to a depth of about 130 km, lying on an asthenospheric layer (V_S about 4.40 km/s) down to a depth of about 230 km.

The cells f-3, f-2 and f-1 (Fig. 3) are characterized by a crust about 40 km thick. In the f-3 and f-2 the asthenospheric top is clearly individuated at about 80 km depth

(V_S about 4.35 and 4.30 km/s, respectively), underlying a lid about 40 km thick (V_S about 4.45 and 4.60 km/s). In the cell f-1 the asthenospheric top is not clearly seen, probably lying at 180 km depth (V_S about 4.45 km/s), under two lithospheric layers of V_S about 4.50 and 4.45 km/s, respectively. In cells f0 and f1 a crust about 30 km thick lies on a lithospheric mantle respectively extended down to 140 and 190 km (V_S about 4.45-4.50 km/s). In the former the asthenospheric top is well marked by a low velocity layer (V_S about 4.00 km/s) extended between 140 and 210 km of depth, while in the latter it is not clearly seen, possibly lying at about 200 km of depth (V_S about 4.45 km/s).

Figure 4. Eastern Alps cellular model.

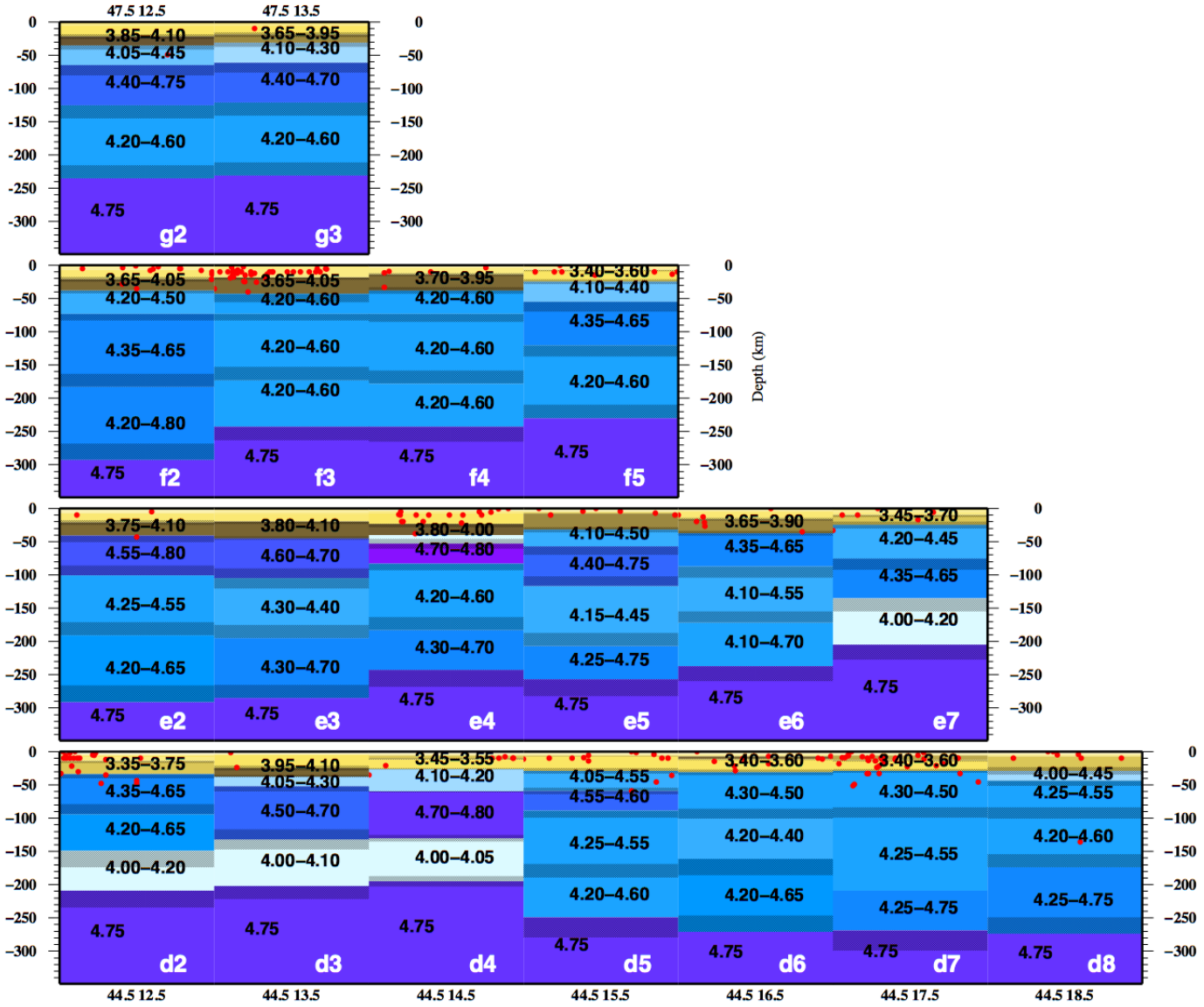

Cellular structural model extended down to 350 km depth for the eastern Alps area. Yellow to brown colors represent crustal layers, blue to violet colors indicate mantle layers. Red dots denote all seismic events collected by ISC with magnitude greater than 3 (1904-2006). For each layer V_S variability range is reported. For the sake of clarity, in the uppermost crustal layers the values of V_S are omitted. The uncertainty on thickness is represented by texture. All the values are given in Appendix B.

In the Eastern Alps, in cells f2 and f3 (Fig. 4) the crust gradually thickens from about 30 to 40 km. The underlying mantle in cell f2 is characterized by velocities gradually increasing down to 280 km of depth (from V_S about 4.35 to 4.50 km/s), while in cells f3 constant velocity layers (V_S about 4.40 km/s) extend down to 250 km depth. The same mantle velocity structure characterizes the cell f4, where the crust is thinner (35 km) than in cell f3. In the cell f5 we find an even thinner crust (about 25 km) than in the previous cell, lying on a soft mantle layer extended down to about 60 km depth (V_S about 4.25 km/s). Below this layer a lid about 60 km thick is present (V_S about 4.50 km/s), while the asthenospheric top (V_S about 4.40 km/s) is detected at a depth of 120-130 km.

In the Western Alps, cell e-4 (Fig. 3) is characterized by a crust about 30 km thick, lying on two lithospheric layers of increasing velocity (V_S about 4.45 and 4.60 km/s) extended down to a depth of about 190 km, where the asthenospheric top is located (V_S about 4.35 km/s). To the east, cells e-3, e-2 and e-1, are characterized by a crust about 40 km thick, lying on a lid extended down to about 120 km in cell e-3 and down to about 90 km in cells e-2 and e-1, with velocities increasing from west to east (V_S about 4.55 to 4.75 km/s). The asthenospheric top is located below the lid, emerging eastward from about 120 to 90 km (V_S about 4.30 and 4.35 km/s respectively). Cell e0 presents a crust of about 40 km thickness lying on two layers of lithospheric mantle extended down to about 140 km depth (V_S about 4.65 and 4.50 km/s). At this depth a marked LVZ individuate the asthenospheric top (V_S about 4.00 km/s). Cells e1 (Fig. 3), e2 and e3 (Fig. 4) present a crust of increasing thickness from about 30 to 45 km depth, below which a lid extended to about 100 km and gently thickening eastward is present, with also eastward increasing velocities (V_S from about 4.50 to 4.65 km/s). The asthenospheric top is detected at about 100 km of depth (V_S about 4.40 km/s in cells e1 and e2, 4.35 km/s in cell e3). In cell e4 we find a crust about 39 km thick lying on a soft mantle layer (V_S about 4.00 km/s) extended down to about 53 km depth. Here a fast lid extends down to about 90 km (V_S about 4.80 km/s). At this depth the asthenospheric top is probably located, with a layer that extends down to about 160 km (V_S about 4.40 km/s). Cell e5 is characterized by a crust about 30 km thick lying on two lithospheric layers with increasing velocities (V_S about 4.30 and 4.55 km/s, respectively) extended to about 110 km of depth, where the asthenospheric top is detected (V_S about 4.30 km/s). Cells e6 and e7 are characterized by a crust of about 35 and 25 km thickness, respectively. In cell e6, right below the Moho, a lid extends down to about 90 km of depth (V_S about 4.50 km/s) where an asthenospheric layer is located (V_S 4.35 and 4.20 km/s, respectively). In cell e7 two lid layers extend from about 25 to about 135 km depth (V_S about 4.35 and 4.50 km/s), where a marked LVZ likely represents the asthenospheric top (V_S about 4.00 km/s).

In the Western Alps, cells d-4 and d-3 (Fig. 3) present a crust about 30 km thick. The underlying mantle is characterized by a gradual increase in velocity down to a depth of 280 km (V_S from about 4.35 to 4.40 km/s) in the cell d-4 while in cell d-3 a lid about 70 km thick underlies the crust (V_S about 4.40 km/s), followed by an asthenospheric layer starting at about 100 km depth (V_S about 4.35 km/s). Cells d-2 and d-1 present a crust of about 40 and 30 km thickness respectively, lying on a lid extended down to about 100 km depth (V_S about 4.60 and 4.45 km/s, respectively). At this depth the asthenospheric top is marked by a low velocity layer (V_S about 4.30 and 4.25 km/s, respectively). To the east, cells d0, d1, and d2 are characterized by a gently thinning crust going from the Apennines to the Adriatic, from 40 to 30 km thickness. The underlying mantle presents two lithospheric layers, thickening westward down to a depth of about 150 in cells d2 and d1 (V_S about 4.50 and 4.70 km/s) and 160 in cell d0 (V_S about 4.70 km/s). Below, a well defined LVZ is extended down to depths of 210-220 km (V_S about 4.00 km/s).

The cells d3 and d4 (Fig. 4) are characterized by a crust of about 25 km thickness, lying on soft mantle material extended down to about 60 km (V_S about 4.10 and 4.15 km/s). Below a lid of about 60 km thickness (V_S about 4.60 and 4.70 km/s, respectively) extends down to about 130 km depth, where the top of asthenosphere is well marked by a LVZ (V_S about 4.00 km/s). Cells d5, d6 and d7 present a crust about 30 km thick. Below, a lithospheric mantle with increasing velocity in cell d5 (V_S from about 4.30 to 4.60 km/s) and constant velocity in cells d6 and d7 (V_S about 4.40 km/s) extends down to about 90 km depth. The asthenospheric top is detected at this depth in cells d5 and d6 (V_S about 4.40 and 4.30 km/s, respectively), while in cell d7 it is not resolved. In cell d8 we find an even thinner crust (about 25 km) than in cell d7, lying on a soft mantle layer (V_S about 4.20 km/s)

of about 15 km thickness. Below, an increasing velocity mantle is found down to about 260 km depth (V_S from about 4.40 to 4.50 km/s).

In cells c-2 and c-1 (Fig. 5), Ligurian Sea, the crust is about 18 and 25 km thick, respectively. In the former a soft mantle layer extends for 20 km below the crust (V_S about 4.10 km/s), lying on a lid extended down to a depth of about 110 km (V_S about 4.40 km/s). In the latter the lid starts below the Moho down to about 100 km depth (V_S about 4.40 km/s). In both cells the top of asthenosphere is detected at depth of 100-110 km (V_S about 4.15 and 4.20 km/s, respectively). Cell c0 is characterized by a crust about 30 km thick, lying on a slightly increasing velocity mantle (V_S from about 4.40 to 4.45 km/s), extended down to a depth of 270-300 km. The crust in cell c1 is relatively thin (about 20 km) and it is followed by a mantle wedge layer about 20 km thick (V_S about 4.10 km/s). Below, a lid layer extends down to about 80 km depth (V_S about 4.55 km/s), where the top of the asthenosphere is probably located (V_S about 4.40 km/s). In cells c2 and c3 both crust and lithosphere slightly thicken eastward through the Apennines, the former ranging from about 35 to 40 km thickness, the latter ranging from about 80 to 90 km thickness (V_S about 4.60 and 4.50 km/s, respectively). The asthenospheric top (V_S about 4.40 and 4.35 km/s, respectively) is located at about 80-90 km of depth. In cell c4, offshore Adriatic sea, a still thick crust (about 40 km) lies on a fast lid (V_S about 4.80 km/s) extended down to about 80 km depth. Below this depth two asthenospheric layers (V_S about 4.30 km/s) are present.

Figure 5. Northern Thyrrenian cellular model.

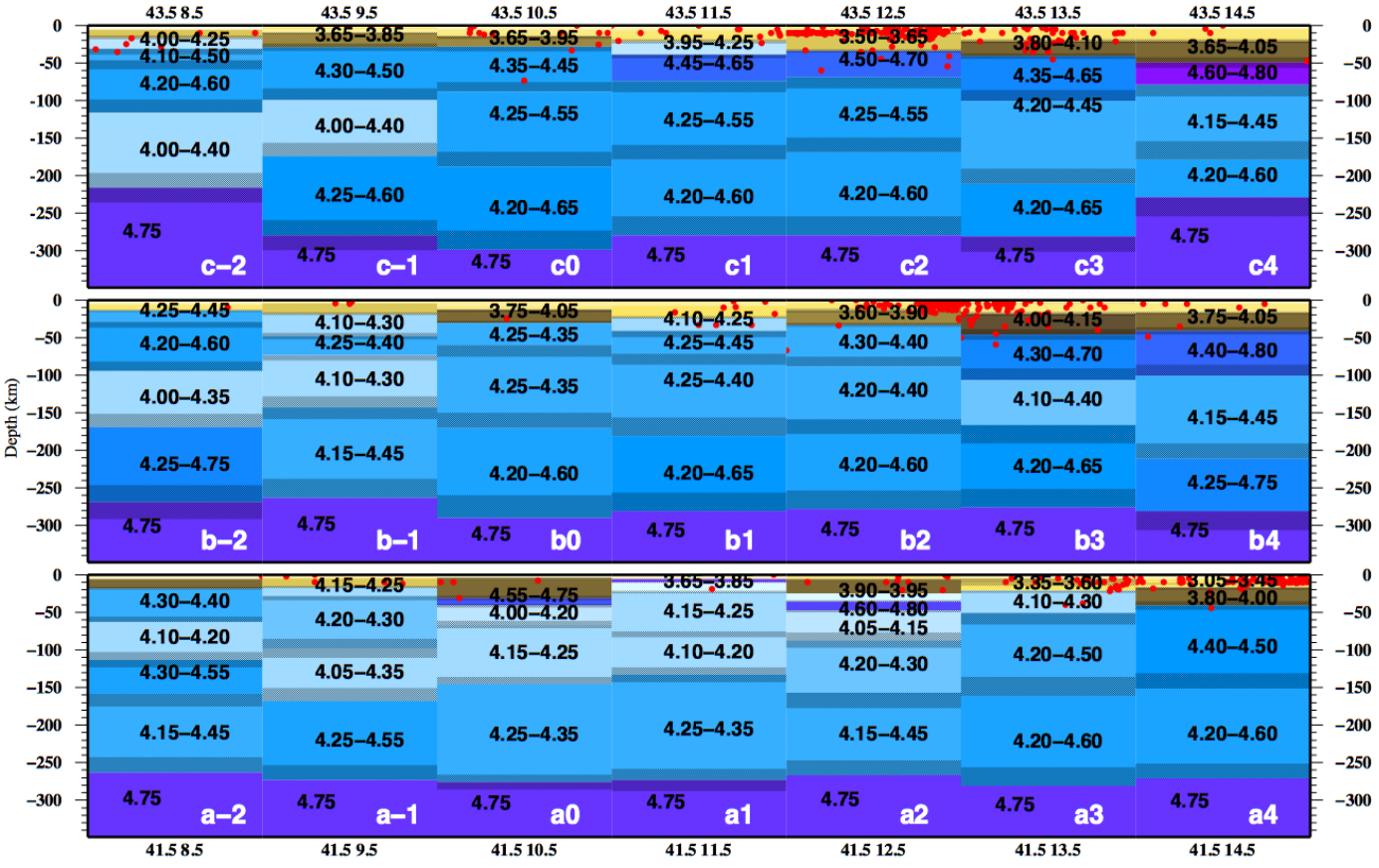

Cellular structural model extended down to 350 km depth for the northern Tyrrhenian area. Yellow to brown colors represent crustal layers, blue to violet colors indicate mantle layers. Red dots denote all seismic events collected by ISC with

magnitude greater than 3 (1904-2006). For each layer V_S variability range is reported. For the sake of clarity, in the uppermost crustal layers the values of V_S are omitted. The uncertainty on thickness is represented by texture. All the values are given in Appendix B.

The cells c5, c6 and c7 (Fig. 6) are characterized by a crust of about 35 km thickness. The underlying mantle presents an almost constant velocity sequence down to about 230 km (V_S about 4.40 km/s) in cells c5 and c6, while in cell c7 a lid about 50 km thick (V_S about 4.50 km/s) extends below the Moho down to about 90 km depth, where the asthenospheric top is likely located (V_S about 4.30 km/s). Cells c8 and c9 present a thick crust (40 and 50 km, respectively) that lies on a mantle with constant V_S of about 4.40 km/s extended down to about 210 – 250 km of depth. Cells c10 and c11 present a crust of about 38 and 35 km, respectively. The underlying mantle in both cells is characterized by lithospheric layers with increasing V_S from 4.35 to 4.50 km/s down to a depth of about 170 - 140 km respectively, followed by an asthenospheric layer with V_S of about 4.40 km/s.

Figure 6. Dinarides cellular model.

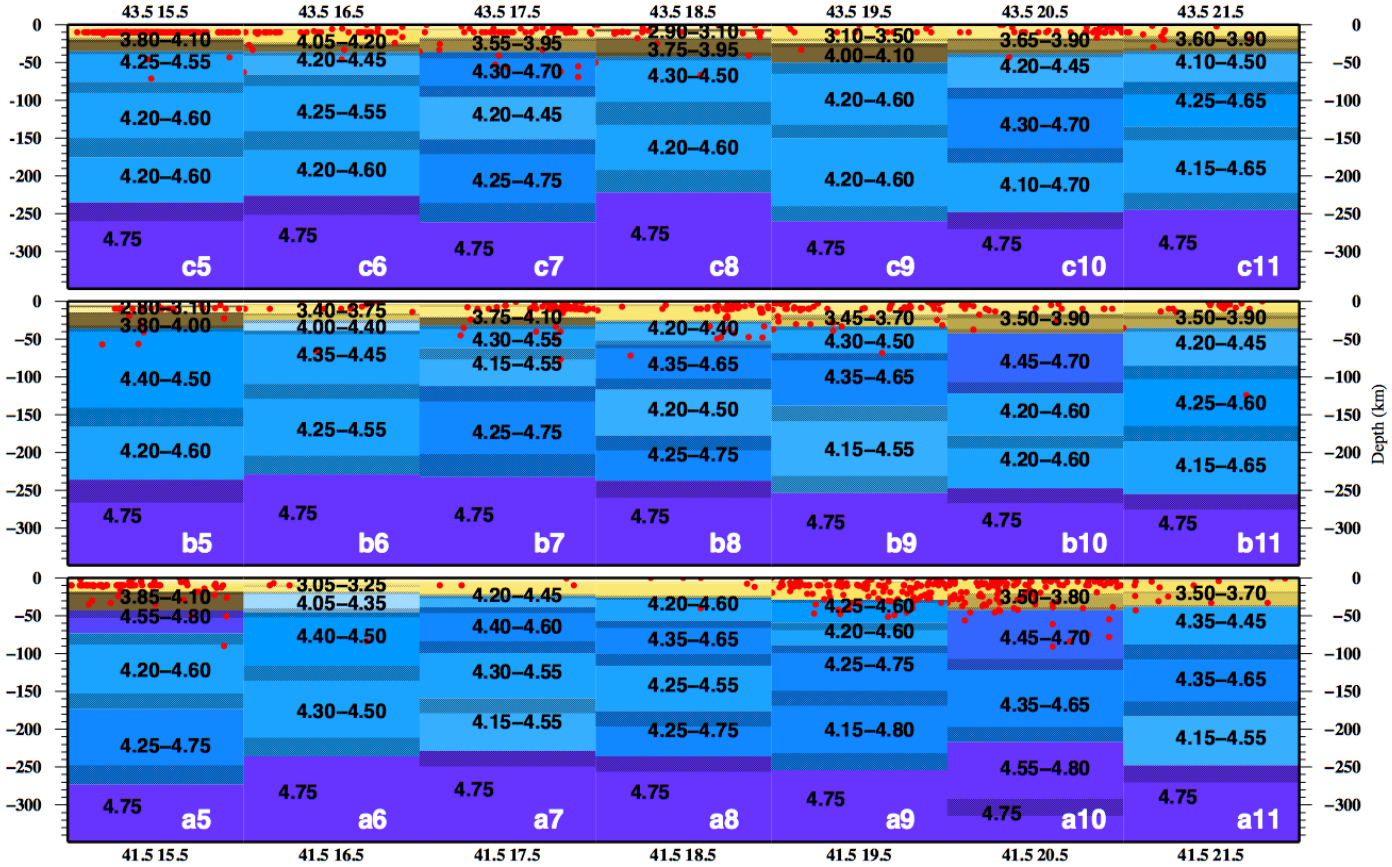

Cellular structural model extended down to 350 km depth for the Dinarides area. Yellow to brown colors represent crustal layers, blue to violet colors indicate mantle layers. Red dots denote all seismic events collected by ISC with magnitude greater than 3 (1904-2006). For each layer V_S variability range is reported. For the sake of clarity, in the uppermost crustal layers the values of V_S are omitted. The uncertainty on thickness is represented by texture. All the values are given in Appendix B.

Cell b-2, in north-eastern Corsica (Fig. 5), is characterized by a thin crust (about 14 km) lying on a lid extended down to a depth of about 80 km (V_S about 4.35-4.40 km/s). Below, the asthenospheric top is well marked by a LVZ of about 60 km thickness (V_S about 4.15 km/s). Cell b-1 presents a crust of about 18 km thickness that lies on a soft mantle layer (V_S about 4.20 km/s) extended down

to about 50 km depth. Here a shallow asthenosphere layer (V_S about 4.30 km/s) is extending down to a depth of 90 km, followed by a LVZ of about 60 km thickness (V_S about 4.20 km/s). In cell b0 a 30 km thick crust seems to lie directly on a shallow asthenosphere or soft mantle layer (V_S about 4.30 km/s). In cell b1 a 20 km thick crust lies on a soft mantle layer (V_S about 4.20 km/s) of about 25 km thickness. Below a shallow asthenosphere (V_S about 4.35 km/s) extends down to a depth of 280 km. In cell b2 a 30 km thick crust lies on a 50 km thick lithospheric layer (V_S about 4.35 km/s) extended down to a depth of about 80 km. At this depth the asthenospheric top is found (V_S about 4.30 km/s). In cells b3 and b4 a crust about 35 km thick lies on a westward thickening lid extended to depths of about 90 km (V_S about 4.55 and 4.60 km/s, respectively). Below the asthenospheric top is well marked by a relative low velocity layer (V_S about 4.20 and 4.30 km/s, respectively) with thickness of 60 km in cell b3 and 100 km in cell b4.

To the east, offshore Adriatic Sea (Fig. 6), cell b5 present a crust about 35 km thick. The underlying mantle in cell b5 is characterized by a lithospheric layer (V_S about 4.45 km/s) down to a depth of about 140 km, where an asthenospheric layer is present (V_S about 4.40 km/s), extended down to about 240 km depth. In cell b6 a thin crust (about 25 km) overlies a soft mantle layer (V_S about 4.20 km/s) that extends below the Moho for a 10 km thickness. Below, a lithospheric layer (V_S about 4.40 km/s) extends down to a depth of about 110 km, where the asthenospheric top is located (V_S about 4.40 km/s). In cell b7 a 35 km thick crust lies on a 40 km thick lid (V_S about 4.40 km/s). The asthenospheric top is located at about 75 km depth (V_S 4.35 km/s). In cells b8 and b9 a gradually thickening crust (from about 30 to 35 km) lies on a eastward thickening lid (V_S increasing from about 4.30 to 4.50 km/s) extended down to a depth of about 150 km. Below the asthenospheric top is clearly detected (V_S 4.35 km/s). In cells b10 and b11 a crust of about 35 km is present. In cell b10 a lid (V_S about 4.60 km/s) extends down to about 130 km, where the asthenospheric top (V_S about 4.40 km/s) is located. In cell b11 a gradually increasing velocity mantle (V_S from 4.35 to 4.45 km/s) extends down to about 170 km, where the asthenospheric top is located (V_S about 4.40 km/s).

Cell a-2 (Fig. 5), in south-western Corsica, presents a crust of about 20 km thickness lying on a lid (V_S about 4.35 km/s) that extends down to about 60 km depth. Below, the top of the asthenosphere is well marked by a LVZ (V_S about 4.15 km/s) of 50 km thickness. Cell a-1 presents a slightly thinner crust (about 18 km) than cell a-2, under which a shallow asthenosphere is detected (V_S about 4.20 km/s). In cell a0, offshore Tyrrhenian, a crust of about 30 km thickness lies on a thin fast lid (V_S about 4.65 km/s) extended down to about 40 km depth, where the asthenospheric top is located (V_S about 4.10 km/s). In cell a1 a very thin crust (about 6 km) lies on a thin fast lid (V_S about 4.75 km/s) extended down to about 11 km depth. Below, a soft mantle layer (V_S about 3.75 km/s) extends down to about 21 km depth, where the top of asthenosphere is likely located (V_S 4.20 km/s). In cell a2 a crust of about 25 km thickness lies on a thin hot mantle layer (V_S about 3.90 km/s) that reaches the depth of about 38 km. A fast lid (V_S about 4.70 km/s) follows, that is extended down to about 50 km depth. Below, the asthenospheric top is well marked by a LVZ (V_S about 4.10 km/s). The structure in this cell is obtained after analysis of the seismicity-depth distribution and it is discussed in details in Panza *et al.* (2007a) and Panza and Raykova (2008). In the Lazio region, cell a3 presents a crust about 25 km thick lying on a soft mantle layer (V_S about 4.20 km/s) that extends down to about 60 km depth, where asthenospheric material is likely to be present (V_S about 4.35 km/s). In cell a4 a crust about 40 km thick lies on a lid layer (V_S about 4.45 km/s) that extends down to about 90 km depth, where the top of asthenosphere is likely to be located (V_S about 4.40 km/s).

Across Apennines, cell a5 (Fig. 6) presents a crust about 50 km thick lying on a fast lid (V_S about 4.70 km/s) extending down to about 90 km depth, where an asthenospheric layer is likely to be present (V_S about 4.40 km/s). To the east, offshore Adriatic Sea, cells a6, a7 and a8 present a gently eastward thickening crust (from about 20 to 30 km). In cell a6 the crust lies on a soft mantle layer (V_S about 4.40 km/s) of about 25 km thickness, below which a lid layer (V_S 4.45 km/s) extends down to about 120 km depth, where asthenospheric top is likely to be located (V_S about 4.40 km/s). In cells a7 and a8 the crust lies directly on a lid layer (V_S about 4.35 and 4.50 km/s) extending down to 90-110 km depth, where the asthenospheric top is likely to be present (V_S about 4.40 km/s). In cells a9 and a10, across Dinarides, an eastward thickening crust (from about 30 to 40 km) lies on a lid (V_S about 4.45 and 4.55 km/s, respectively) extending down to about 70 and 120 km respectively, where the top of

asthenosphere is likely to be located (V_S about 4.40 and 4.50 km/s respectively). In cell a11 a crust about 40 km thick lies on a lid that extends down to about 170 km (V_S about 4.40 and 4.50 km/s), where the top of the asthenosphere is likely to be present (V_S about 4.35 km/s).

In cell A-2 (Fig. 7), north-western Sardinia, a crust about 18 km thick lies on a 10 km thick fast lid (V_S about 4.80 km/s). Below, another lid layer (V_S about 4.30 km/s) extends down to about 60 km depth, where an asthenospheric LVZ starts (V_S about 4.20 km/s), reaching the depth of about 150 km. Cells A-1, A0 and A1 are characterized by a crust about 20 km thick, lying on a lid layer (V_S about 4.45 and 4.30 km/s, respectively) that extends down to about 60 km depth, where an asthenospheric LVZ of about 60-80 km thickness is likely to be present (V_S about 4.20 and 4.00 km/s, respectively). In cell A2 a 25 km thick crust lies on an about 10 km thick lid (V_S about 4.40 km/s). At about 40 km depth the asthenospheric LVZ is likely to be present (V_S about 4.15 km/s), that extends down to about 100 km depth. In cell A3 a thin crust (about 6 km) overlies a lid about 8 km thick (V_S about 4.40 km/s) which lies on a soft mantle layer (V_S about 3.50 km/s) extended down to about 21 km depth, where an asthenospheric LVZ (V_S about 4.00 km/s), that extends down to about 60 km depth, is likely to be present. In cell A4 a crust about 25 km thick lies on a soft mantle layer (V_S about 4.20 km/s) that extends down to about 70 km depth. Below, two asthenospheric layers (V_S about 4.40 km/s) extend down to about 300 km depth.

Figure 7. Southern Thyrrenian cellular model.

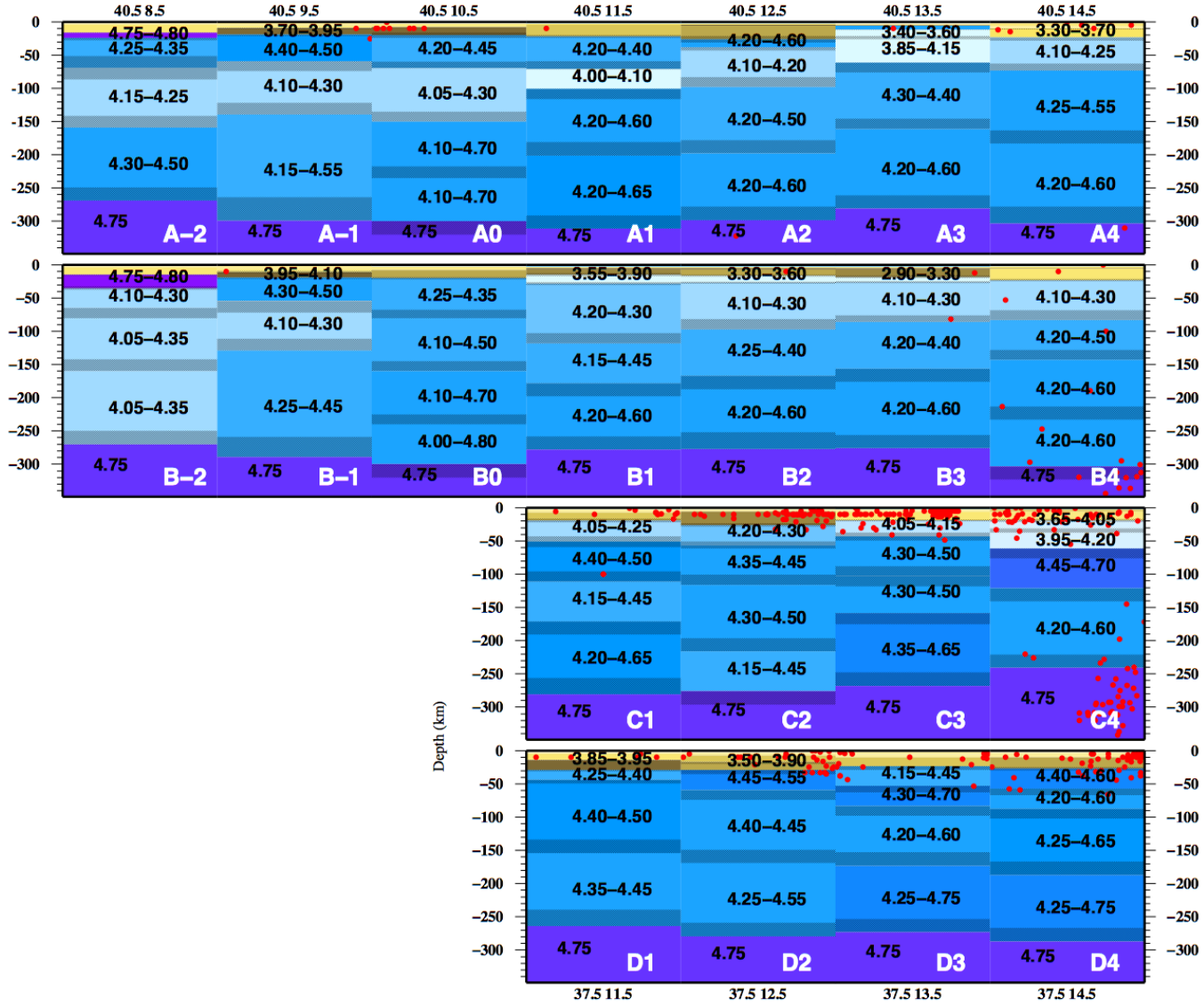

Cellular structural model extended down to 350 km depth for the southern Tyrrhenian area. Yellow to brown colors represent crustal layers, blue to violet colors indicate mantle layers. Red dots denote all seismic events collected by ISC with magnitude greater than 3 (1904-2006). For each layer V_S variability range is reported. For the sake of clarity, in the uppermost crustal layers the values of V_S are omitted. The uncertainty on thickness is represented by texture. All the values are given in Appendix B.

In cells A5 and A6, across the Southern Apennines (Fig. 8), an eastward thickening crust (about 25 km thick in A5 and 36 km thick in A6) overlies a thin mantle wedge with velocities 4.05-4.25 km/s and thickness about 50 km in A5 and 13 km in A6. A high velocity westward thickening lid (V_S about 4.80 km/s) is extended down to about 100 km depth, where the top of the asthenosphere is likely to be present (V_S about 4.30 and 4.35 km/s, respectively). In cell A7 a 40 km thick crust overlies a lid (V_S about 4.60 km/s) that extends down to about 100 km depth. Below, an asthenospheric layer (V_S about 4.45 km/s) extends down to about 250 km of depth. Across the Dinarides, in cells A8, A9 and A10, an eastward thickening crust (from about 25 to 40 km) lies on an eastward thickening lid (V_S about 4.60 and 4.55 km/s, respectively) that extends down to depths of about 70, 90 and 150 km, respectively. Below, astenospheric layers (V_S about 4.30, 4.45 and 4.40 km/s, respectively) extend down to about 290, 300 and 240 km of depth.

Figure 8. Ionian cellular model.

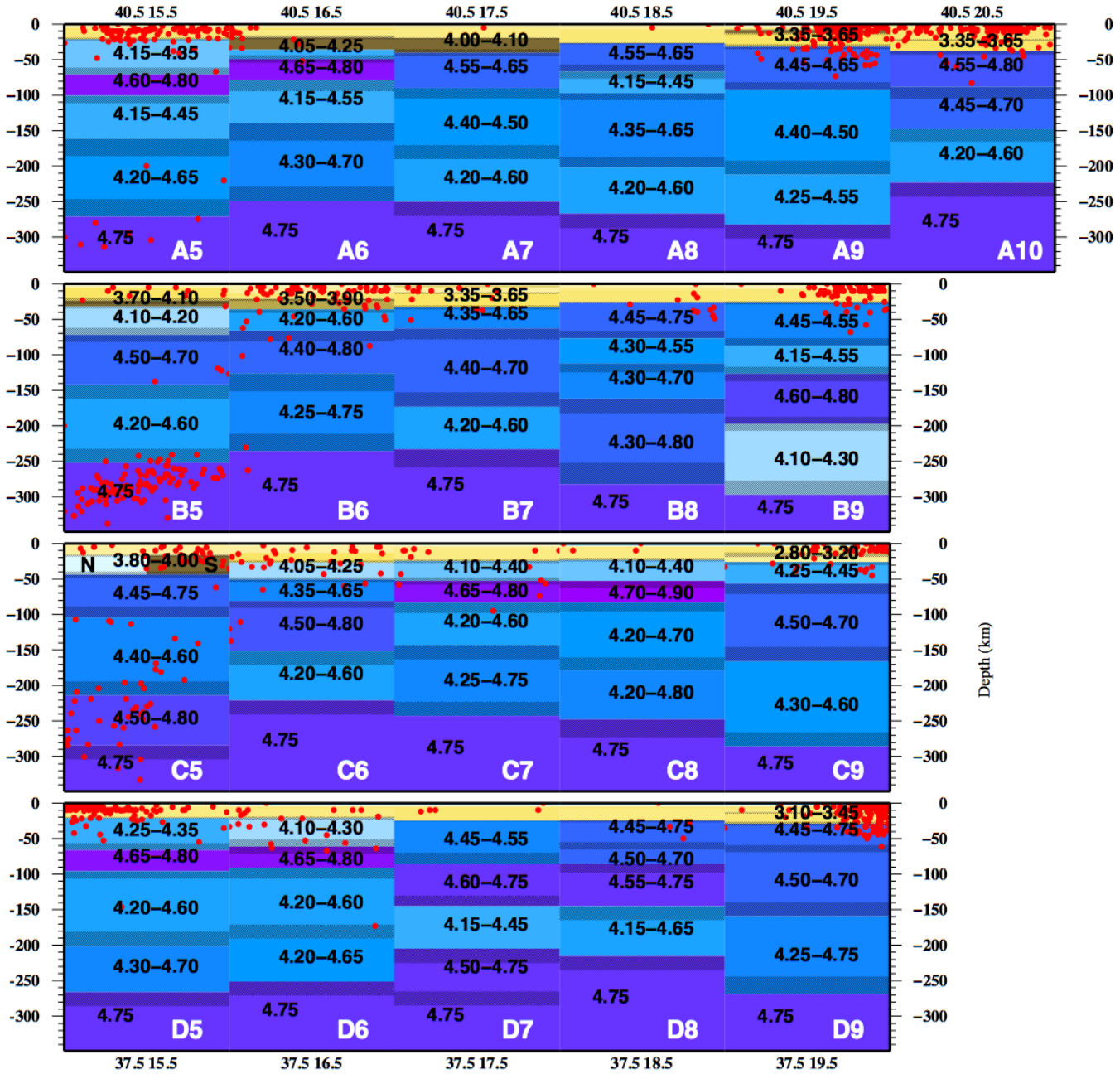

Cellular structural model extended down to 350 km depth for the Ionian area. Yellow to brown colors represent crustal layers, blue to violet colors indicate mantle layers. Red dots denote all seismic events collected by ISC with magnitude greater than 3 (1904-2006). In cell C5 seismicity is projected on a north-south axis, according to split crustal layer. For each layer V_S variability range is reported. For the sake of clarity, in the uppermost crustal layers the values of V_S are omitted. The uncertainty on thickness is represented by texture. All the values are given in Appendix B.

In cell B-2 (Fig. 7), south-western Sardinia, a crust about 18 km thick lies on a fast lid layer (V_S about 4.80 km/s) that extends down to about 35 km depth. Here a marked asthenospheric LVZ (V_S about 4.20 km/s) extends down to about 270 km of depth. Cell B-1 has a high-velocity crust about 20 km thick that overlies a lid (V_S about 4.40 km/s) with thickness of about 40 km. The LVZ (V_S about 4.20 km/s) below the lid has a thickness of about 60 km and it is followed by a layer with V_S about 4.35 km/s extended down to about 290 km of

depth. Cell B0 has a crust with a similar thickness as in cell B-1 but with lower V_S. The following mantle layers have slightly increasing V_S from 4.30 to 4.40 km/s down to about 300 km of depth. In cells B1, B2 and B3 a crust about 12 km thick lies on a very soft mantle (V_S about 3.70, 3.45 and 3.10 km/s, respectively) of about 13 km thickness. The V_S in the following mantle layers gradually increases with depth, from about 4.20 to 4.40 km/s, down to about 280 km depth. Offshore Calabria, in cell B4 (Fig. 7), a crust about 25 km thick lies on a soft mantle layer (V_S about 4.20 km/s) that extends down to about 70 km depth. Below, slightly increasing velocity layers (V_S from about 4.35 to 4.40 km/s) extend down to about 280 km of depth.

In cell B5 (Fig. 8) a crust about 30 km thick lies on a mantle wedge (V_S about 4.15 km/s) extended down to about 70 km of depth. Below, a lid layer (V_S about 4.60 km/s) extends down to about 150 km depth, where an asthenospheric layer begin (V_S about 4.40 km/s). Across Calabria, in cells B6 and B7, a crust of about 35 km and 30 km thickness, respectively, overlies lid layers (V_S about 4.40 and 4.60 km/s in cell B6, 4.50 and 4.55 km/s in cell B7) that extend down to about 150 km of depth. In both cells an asthenospheric layer is likely to be located at this depth (V_S about 4.50 and 4.40 km/s, respectively) that extends down to about 230 km of depth. Offshore Ionian Sea, in cells B8 and B9 a crust about 28 km thick is present, lying on a lid layer (V_S about 4.60 and 4.50 km/s, respectively) extended down to about 75 km depth. Below, in cell B8, an asthenospheric layer is likely to be present (V_S about 4.45 km/s), while in cell B9 a likely asthenospheric layer of about 40 km thickness (V_S about 4.35 km/s) lies on a fast layer (V_S about 4.70 km/s) that extends down to about 200 km depth, where another asthenospheric layer is likely to be present (V_S about 4.20 km/s).

Offshore Sicily (Fig. 7), in cells C1 and C2 a crust about 20 and 25 km thick, respectively, overlies a soft mantle layer (V_S about 4.15 and 4.25 km/s, respectively). Below, a lid layer (V_S 4.45 and 4.40 km/s respectively) extends down to about 100 km depth, where the asthenospheric top is likely to be located (V_S about 4.30 and 4.40 km/s respectively). In cells C3 and C4 a crust of about 20 km thickness lies on a soft mantle layer extended down to 40-60 km depth, respectively. The underlying mantle layers present slightly increasing V_S (from 4.40 to 4.50 km/s) down to the depth of 270 km in cell C3, while in cell C4 the V_S decreases from 4.55 to 4.40 km/s down to the depth of about 240 km.

Toward Calabria (Fig. 8), the V_S structure of cell C5 is obtained after the comparison with the distribution of the seismicity with depth (see section "Discussion" for details). The crust in the northern part of the cell is about 19 km thick and lies over a hot mantle layer (V_S about 3.90 km/s and thickness of 20 km), followed by high velocity lid layers extended down to about 280 km of depth. The crust in the southern part of the cell is about 44 km thick and lies on a seismic lid with a V_S about 4.60 km/s that extends down to about 280 km of depth. In cell C6 a crust about 25 km thick lies on a soft mantle layer (V_S about 4.15 km/s) of about 25 km thickness. Below, two lid layers (V_S about 4.50 and 4.65 km/s, respectively) extend down to about 160 km depth, where an asthenospheric layer (V_S about 4.40 km/s) extends down to about 210 km of depth. Offshore Ionian Sea, cells C7 and C8 present a crust of about 25 km thickness lying on a soft mantle layer (V_S about 4.25 km/s) extended down to about 50 km depth. Below, a fast lid layer (V_S about 4.80 km/s) extends down to about 80 km depth, where the asthenospheric top is likely to be located (V_S about 4.40 and 4.45 km/s, respectively). Toward the Hellenides, in cell C9 a crust of about 30 km thickness lies on lid layers (V_S 4.35 and 4.60 km/s) that extends down to about 160 km, where the top of the asthenosphere is detected (V_S about 4.45 km/s).

In cell D1 (Fig. 7), in the Sicily Channel, a crust about 30 km thick lies on lid layers (V_S about 4.30 and 4.45 km/s) that extend down to about 130 km, where the asthenospheric top is likely to be present (V_S about 4.40 km/s). In cells D2 and D3 an about 30 km thick crust lies on lid layers (V_S about 4.50 km/s in cell D2 and about 4.30 and 4.50 km/s in cell D3) that extend down to about 70 and 90 km depth respectively, where the asthenospheric top is likely to be located (V_S about 4.40 km/s). In cell D4 a crust about 30 km thick lies on two lid layers (V_S about 4.50 and 4.40 km/s) extended down to about 100 km. The asthenospheric top is not clearly detected, possibly represented by a V_S about 4.45 km/s layer between 100 and 170 km depth.

In cells D5 and D6 (Fig. 8), offshore Eastern Sicily, a 20 km thick crust lies on a soft mantle layer (V_S about 4.30 and 4.20 km/s, respectively) that extends down to about 60 km depth. Below a fast lid (V_S about 4.80 km/s) layer of about 30 km thickness extends down to about

100 km depth, where the asthenospheric top is detected (V_S about 4.40 km/s). Toward the Hellenic Trench, in cells D7, D8 and D9 a gently thickening crust (from about 25 to 30 km) lies on a lid layer (V_S about 4.50 and 4.75 km/s in cell D7, 4.60 and 4.75 km/s in cell D8, 4.60 km/s in cell D9) that extends down to about 150-160 km depth, thickening to the east. At this depth the asthenospheric top is likely to be detected (V_S about 4.30, 4.40 km/s and 4.50 km/s, respectively).

GFO refined structural model of Alpine region

The hierarchical application scheme of optimization algorithms described in section "Methodology" is applied to the Alpine region, in order to refine the structural model obtained by LSO. Furthermore, additional constrains to the uppermost fixed crust, taken from seismic reflection experiments (i.e. CROP-ECORS, EGT and TRANSALP), have been used to perform the inversion on half cells, i.e. sized 1°x0.5° or 0.5°x1° (Farina, 2006).

The main features of the LSO structural model are preserved by the application of GSO and GFO, in particular concerning crustal thickness and velocities. The accordance with the values in the literature is improved only in cell f4, where LSO chooses a crust too thin for Eastern Alps (about 25 km), while GFO realistically indicates a crust of about 40 km.

The main differences emerging from the application of GSO and GFO are at mantle depths, in particular in the location of LVZ. In cell d-4, Western Alps, a LVZ (V_S about 4.00 km/s) appears to extend between 215 and 320 km of depth, according to GFO, while LSO depicted in this cell a relatively fast asthenosphere (V_S about 4.40 km/s). On the contrary, in cell d1, GFO depicts a relatively fast asthenosphere (V_S about 4.45 km/s) between about 150 and 210 km of depth while LSO located a LVZ (V_S about 4.00 km/s).

The inversion on half-cells allowed to gain details both on the crust and the underlying mantle structure. (Fig. 9) In the cell e-4, in the Western Alps, the thick lid depicted by the 1°x1° inversion results is present, but is limited to the eastern half part of the cell. Similarly an eastward thickening trend of crust is depicted by GFO results, according to independent data on Moho depth.

Figure 9. Alpine refined cellular model.

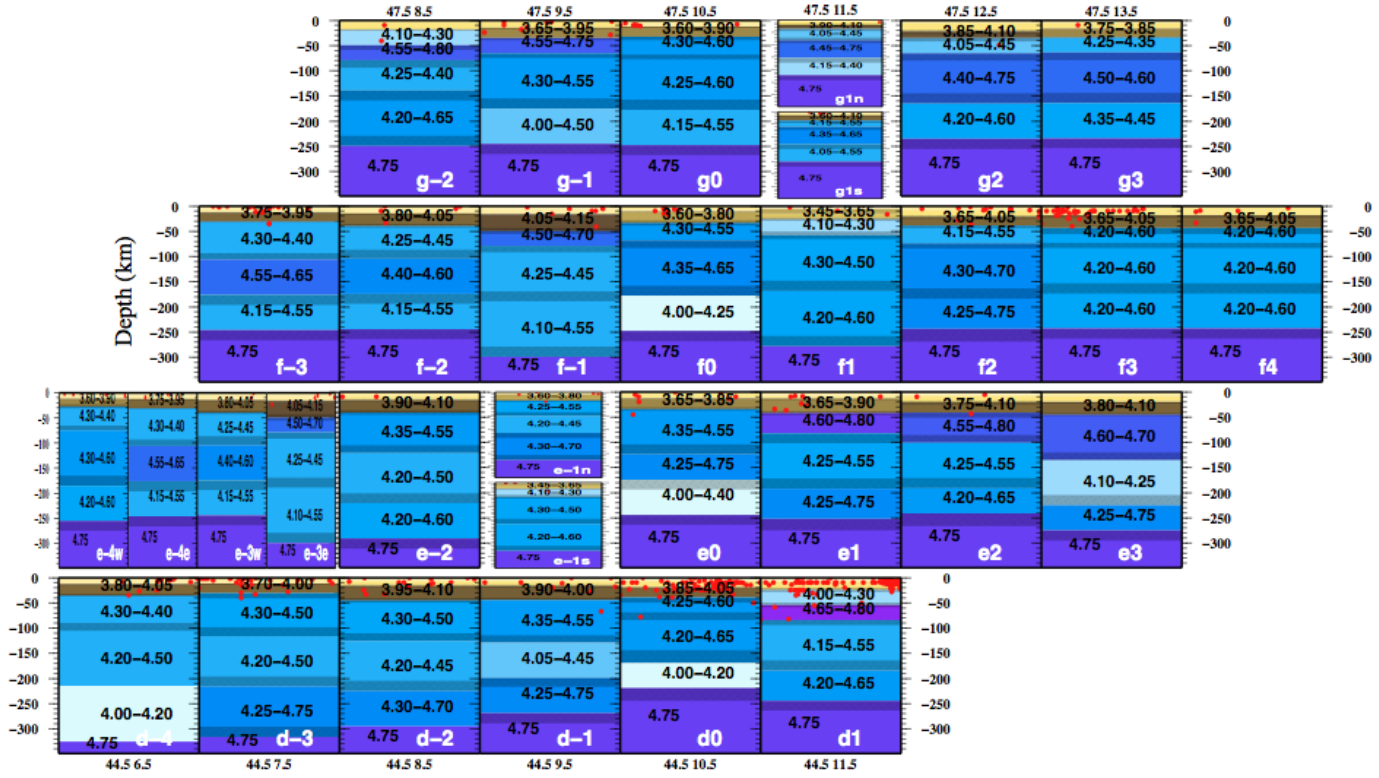

Cellular structural model extended down to 350 km depth for the Alpine area, refined with GSO and GFO optimization algorithms, with splitting of some cells to 1°x0.5° or 0.5°x1.0°, along profiles where additional crustal information were available. Yellow to brown colors represent crustal layers, blue to violet colors indicate mantle layers. Red dots denote all seismic events collected by ISC with magnitude greater than 3 (1904-2006). For each layer V_S variability range is reported. For the sake of clarity, in the uppermost crustal layers the values of V_S are omitted. The uncertainty on thickness is represented by texture. All the values are given in Appendix C.

Latitudinal splitting of cell e-1, in the Ivrea Zone, allowed to define the crustal thickness of about 22 km in the southern half-cell and of about 30 km in the northern half-cell, respectively.

Latitudinal splitting of cell g1, along the TRANSALP profile, allowed a detailed definition of the asthenospheric top, located at about 150 km of depth with V_S about 4.15 km/s in the northern half-cell and about 4.30 km/s in the southern one.

Discussion

V_S structures and geophysical constraints

Since the non-linear inversion and its smoothing optimization guarantee only the mathematical validity of the selected structural models, independent geophysical information (e.g. Moho depth, seismicity and heat flow) are used as additional constraints whenever necessary. The structural models selected by LSO are appraised with respect to independent information available in the literature concerning the Moho boundary depth (Dezes and Ziegler, 2001; Tesauro *et al.*, 2008; Grad and Tiira, 2008). More than half of the cells in the study area have the Moho depth in accordance with the average value reported by Dezes and Ziegler (2001). Moreover, comparing the Moho depth resulting from our model, taken with its uncertainties, to the minimum and maximum depth reported by Tesauro *et al.* (2008) and Grad and Tiira (2008), for each cell, the agreement rises to about 90%.

Some of the cells that have Moho depth in disagreement with the above cited literature can be considered as influenced by border effects, i.e. the cells are at the border of the study area and could not be constrained well by the optimization algorithms. In these cells we choose among the cellular set of solutions the one that has crustal thickness in agreement with the values in the

literature, if such solution exists. This is the case for cells e7, c10, b10 and D4. The selected models correlate well with the observed seismicity-depth distribution. Cells B-2 and g-2 are on the border of the study area and present a crust thinner than the values reported in the literature, but among the set of solutions for both cells there is no model that has values for the Moho depth closer to the published ones. Anyway, we consider the modelled crustal depth for cell B-2 to be realistic, since the obtained V_S model is derived from surface wave data with good coverage, especially in the Sardinia region and we do not know any other more detailed study of the Sardinian crustal structure.

The main differences are observed in cells where a steep Moho gradient is present (i.e. collisional or subduction zones and oceanic-continental boundaries). The crustal structure of these cells is discussed below.

In cell B8 (Ionian Sea), a crust 27 km thick is modelled that is thinner than that reported in the literature. Among the solutions for the cells there is no model with thicker crust, therefore we consider our result more reliable.

In cells A-2, A-1 and A5 the Moho depth is shallower than the values reported in the literature, but the obtained values are well correlated with a geological section crossing these cells (discussed in detail in Panza *et al.*, 2007b).

In cell d4 a crust (25-27 km) thinner than that reported in the above cited literature (30-42 km depth) is modeled, but a recent study of Šumanovac *et al.* (2009) indicates a crust less than 30 km thick in the Quarnaro Gulf. Moreover, the cellular seismicity deeper than 20 km is almost absent. The underlying soft mantle layer (V_S ~ 4.10 km/s) has a thickness of about 34 km, reaching 60 km of depth. The observed heat flow in this cell is low, about 40 mW/m^2.

The selected model for cell a-1 has a thin, about 16 km, crust that overlies a soft mantle layer with V_S of about 4.20 km/s that reaches the depth of 28 km. The cellular seismicity is weak and the heat flow values do not exceed 70 mW/m^2.

In cell a1 the Moho is observed at about 6 km of depth. The crust overlies a LID layer with V_S of 4.70-4.80 km/s that reaches the depth of about 10 km. The following 10 km thick soft mantle lid, with V_S of 3.65-3.85 km/s, is the most probable source of the observed high heat flow (150 mW/m^2). The structure of the cells is in accordance with the petrological interpretation that is discussed in detail by Panza *et al.* (2007a).

In cell A3 the crust reaches the depth of about 6 km and overlies a layer with V_S 4.20-4.60 km/s extended down to 11 km of depth. The underlying layers have V_S about 3.50 km/s and 4.00 km/s, respectively, and thickness of about 10 km and 40 km, therefore can be interpreted as soft mantle, in fair accordance with high heat flow (about 150 mW/m^2). The velocity structure of this cell is discussed in detail by Panza *et al.* (2007a) considering the Moho depth at 6 km. Alternatively we could interpret the 5 km thick layer with V_S between 4.20 and 4.60 km/s as an Ultra High Pressure (UHP) metamorphosed crust with high percentage of coesite (V_S about 4.60 km/s and a density of about 2.9 g/cm^3, according to Anderson 2007). In this way, a Moho depth of about 11 km will be in agreement with Moho depth reported in the literature and seismicity-depth distribution. This new interpretation of the velocity structure is not in contradiction with interpretation given in Panza *et al.* (2007a).

In cell A7 the layer with V_S of 4.10 km/s at depths between 20 and 40 km is interpreted as crust with V_S range of 4.00 - 4.10 km/s. The thickness of the crust is in the range 35 - 45 km and it is slightly thicker than the maximum values found in the above cited literature (30 – 36 km). However, our interpretation fits well the low heat flow (less than 40 mW/m^2) that is observed in the area. Weak seismicity is observed in the cell down to a depth of about 35 km. Similarly in cell c6, the layer with V_S about 4.20 km/s, located between 26 and 36 km of depth, is considered to be crustal with V_S range from 4.05 to 4.20 km/s. The resulting crustal thickness (about 36 km) is in accordance with the above cited literature values (ranging from 32 to 43 km). The values of the heat flow in the cell are less than 35 mW/m^2 (Hurting *et al.*, 1991), correlating well with our interpretation.

In cell a5, the 43 km thick crust is slightly thicker than that reported in the literature (ranging from 29 to 38 km). However, the crustal structure of our model correlates well with observed seismicity, that stops at a depth of about 40 km, and low heat flow (less that 60 mW/m^2). Similarly the obtained 49 km thick crust in cell c4 correlates well with significant seismic energy release (down to about 48 km of depth) and low heat flow (less than 45 mW/m^2) observed in the cell.

The cell a6 (offshore Apulia) presents a thinner crust (about 20 km) than the published values (ranging from 27

to 38 km). The following mantle layer with V_S of 4.05-4.35 right below the Moho is extended to 46 km of depth. The observed seismicity in this layer is weak and heat flow is less than 65 mW/m^2.

In cell a2, under the Albani hills and the Tyrrhenian offshore, with heat flow reaching 150 mW/m^2, the definition of Moho is difficult using V_S alone. The Moho is located at 25 km of depth splitting the 29 km thick layer with V_S range of 3.90-3.95 km/s into two parts: 19 km thick crustal layer and 10 km thick mantle layer, according to the seismicity-depth distribution (discussed in detail in Panza *et al.*, 2007a; Panza and Raykova, 2008). Similarly in cell e4, at about 23 km of depth, the 30 km thick layer with V_S about 4.00 km/s is split in two layers: a 17 km thick crustal layer lying on a 13 km thick soft mantle layer, according to the seismicity distribution that is concentrated in the uppermost 40 km (Panza *et al.*, 2007a). The Moho depth defined in this way for the cells a2 and e4 is in fair agreement with published data. We proceeded similarly for cell A6 (Fig. 10). The values for the crustal thickness range from 32 to 39 km and the heat flow ranges from 30 to 90 mW/m^2. In the obtained V_S model an upper crustal layer with V_S of about 3.10 km/s reaches the depth of 19 km. The following 30 km thick layer has V_S from 4.05 to 4.25 km/s. Below this layer a high velocity lid (V_S 4.65-4.80 km/s) reaches the top of the asthenosphere at about 80 km of depth. The depth distribution of the observed seismicity is analyzed and the computed histograms are shown in Fig.10. The obtained V_S model down to the depth of 60 km is presented in Fig. 10a using the same V_S color coding as in Figs. 3-9. The location of the earthquakes with magnitude specified by the ISC catalogue are noted by red dots, while the events without magnitude indication are noted by red circles. The seismicity-depth distribution is presented in several histograms: logN-h distribution (Fig. 10b), logE-h distribution (Fig. 10c), and log$\prod$E-h distribution (Fig. 10d). All three kinds of seismicity-depth distributions are calculated for two selections of events: all events from the ISC catalogue (red histograms, related red-color annotations and text on the top of the Figs 10b, c, and d) and events with depth not fixed *a priori* in the hypocenter computing (black-line histograms, related black-color annotations and text on the bottom of the Figs 10b, c, and d). The N_{max}in Fig 10b gives the maximal number of the earthquakes in the 4 km thick depth intervals. The E_{min} in Fig. 10c means minimal sum of energy in the depth intervals, that is greater than 0 and that is used as the normalization factor in log$\prod$E-h calculation. The $\prod E_{max}$in Fig. 10d denotes the maximum of the energy product in the depth intervals, that is greater than 0 and that is used as the normalization factor in logE-h calculation. Analyzing the presented seismicity-depth distributions the clear stop of the seismicity at about 36 km is observed and thus we locate the Moho at this depth. Therefore, the lower crust (17 km thick) with a V_S range of 4.05-4.15 km/s lies on a 13 km thick soft mantle layer with a V_S range of 4.05-4.25 km/s. The presence of this shallow, thin, and soft mantle layer can be related to the elevated local heat flow data (up to 90 mW/m^2).

Figure 10. Cell A6: model and seismicity.

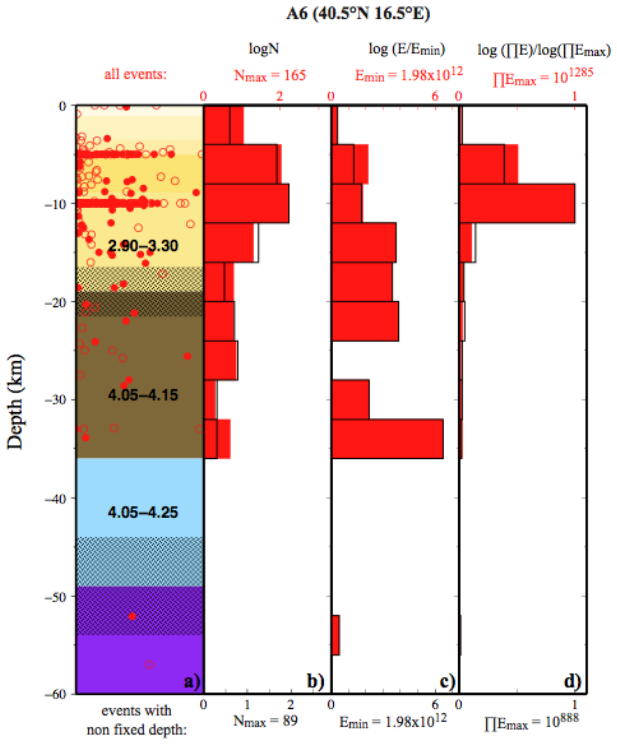

The cellular V_S structure of cell A6 and distributions of seismicity. The model is plotted on the leftmost graph (a). The V_S ranges of variability in km/s are printed on each layer and the hatched rectangles outline the ranges of variability of the layer's thickness. The values of V_S in the uppermost crustal layers are omitted for the sake of clarity. The hypocentres with depth and magnitude type specified in the ISC catalogue are denoted by dots. The hypocentres without magnitude values in the ISC catalogue are denoted by circles. (b) logN-h, distribution of the number of earthquakes with respect to depth obtained by grouping hypocentres in 4-km intervals. (c) logE–h, distribution of the

normalized logarithm of seismic energy for 4-km-thick depth intervals. (d) log∏E-h, distribution of the normalized logarithm of product of seismic energy for 4-km-thick depth intervals. The filled red bars histograms represent the computation that used all earthquakes from the revised ISC (2007) catalogue for period 1904–June 2005. The black line histograms represent the computation that used earthquakes which hypocentre's depth is not fixed *a priori* in the ISC catalogue. The normalizing values of energy's logarithm logE_{min} and product of energy's logarithm log∏E_{max} are given on the horizontal axes of the relevant graphs.

The V_S models of the cells where the intensive deep mantle seismicity is observed are correlated with computed seismicity-depth distribution. In cell C4 (Aeolian Islands) the seismicity is observed down to about 340 km and the heat flow is in the range of 75 – 250 mW/m^2. The very intensive and energetic seismic-depth distributions in the uppermost 20 km of the structure (Fig. 11a, the symbols that are used are the same as in Fig. 10) indicate the Moho depth of about 20 km. A hot mantle layer follows, with V_S about 3.65-4.20 km/s down to 60 km of depth. The seismicity decreases drastically below 20 km of depth and almost stops at a depth of about 50 km. The deep seismicity starts to be notable below 90 km of depth down to about 200 km of depth. The V_S at these depths decreased slightly from 4.55 km/s to about 4.40 km/s. The seismic energy release deeper than 220 km increased drastically and this peak correlates very well with the top of the high velocity layer (V_S about 4.75 km/s). The observed intense seismicity below a depth of 220 km has almost constant energy release down to a depth of 350 km.

Figure 11. Cell C4: model and seismicity.

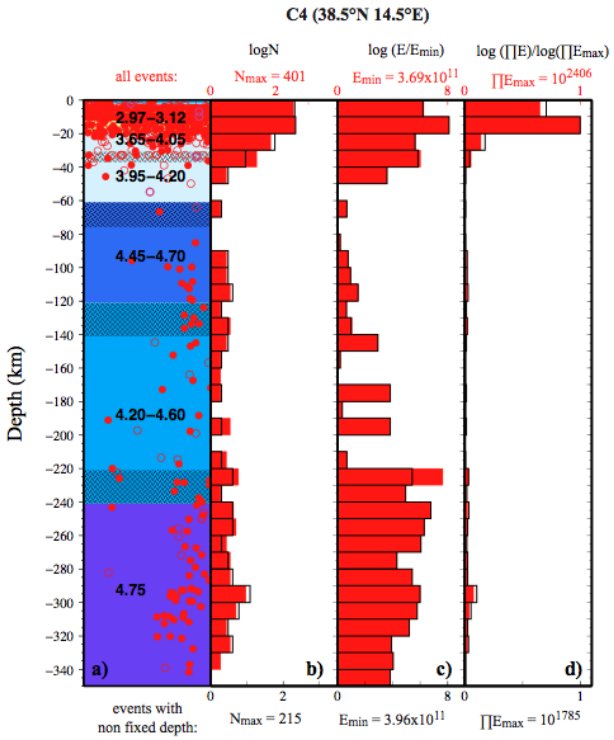

The cellular V_S structure in cell C4 and related seismicity distribution, obtained grouping hypocentres in 10-km intervals: (a) V_S cellular model; (b) logN-h; (c) logE–h; (e) log∏E-h. The symbols used are the same as in Fig. 10.

Similarly, very intensive deep seismicity is observed in cell C5 (Fig. 12) (area of Stromboli, Messina Strait and Southern Calabria) down to the depth of about 400 km. The unconstrained V_S model selected by LSO is not consistent with the observed seismicity and independent data about the presence of a subducting slab (Panza *et al.* 2007a). Among the set of solutions for this cell only those consistent with the seismicity are considered and LSO is performed again keeping the solutions in the neighbouring cells fixed. The selected model is further analyzed considering the seismicity in the northern and southern half of the cell separately (Panza *et al.* 2007a, Panza and Raykova, 2008). The comparison between the unconstrained solution and selected representative cellular model and their correlation with the seismicity distributions is shown in Fig. 12. The unconstrained solution (Fig. 12a) is not consistent with the observed seismicity and known structural features in the region, while the constrained solution shown in Fig. 12b correlates very well with the seismicity-depth distributions (logN-d

shown in Fig. 12c; logE-h shown in Fig 12d, log∏E-h shown in Fig 12e; the symbols used are the same as in Fig. 10). It is difficult to define the nature of the crust in the selected V_S model, since a layer with V_S in the range 3.8–4.0 km/s reaching a depth of about 44 km overlies high velocity mantle material. The analysis of the seismic energy distribution (details given in Panza *et al.*, 2007a; Panza and Raykova, 2008) leads to two distinct interpretations for this two-faced (Janus) crust/mantle layer. Considering only the hypocentres at sea (northern half of the cell), this layer is totally aseismic and therefore it is assigned to the mantle, and the crust in this half of the cell has an average thickness of 17 km. On the other hand, considering only the hypocenters in the continental southern half of the cell, the "Janus" layer is intensively seismic and therefore it is assigned to the brittle continental crust which turns out to be 44 km thick.

Figure 12. Cell C5: model and seismicity.

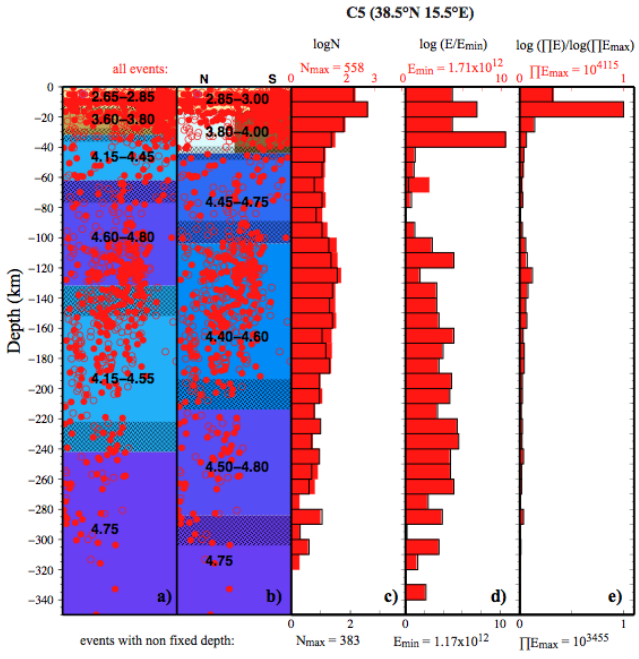

The cellular V_S structure in cell C5 and related seismicity distribution obtained grouping hypocentres in 10-km intervals: (a) the unconstrained model selected by LSO; (b) the representative cellular model; (c) logN-h; (d) logE–h; (e) log∏E-h. The symbols used are the same as in Fig. 10.

Our modeling results confirm some general well-known features as the presence of deep lithospheric roots in western Alps (Panza and Muller, 1979; Farafonova *et al.*, 2006) down to 180-200 km of depth (cells e-4, e-3, e-2 and d-4), while lithospheric roots are likely to be absent in the Jura mountains sector (cells g-2, g-1 and f-2), where the lithosphere thickness is about 90 km.

Lithospheric roots are also detected in the eastern Alps and south-Alpine sector, across the Insubric line (cells f1, f2 and f3), where the lithosphere extends down to 200-250 km depth, indicating a northward dipping with respect to the lithosphere in cells e1, e2, e3. In the Po Valley, the lithosphere thickness ranges between 90 km and 120 km, with a prominent LVZ (V_S about 4.00 km/s) marking the top of the asthenosphere below the Adria Plate (cells f0, e0, d0-d4) .

The main geodynamical features of the Apennines and Tyrrhenian basin are well delineated by the model, as the presence of relatively high-velocity bodies along the Apennines indicates the subduction of the Adria lithosphere (Panza *et al.*, 2007b), and the shallow crust-mantle transition beneath the Tyrrhenian Sea, with extended soft mantle layers (V_S < 4 km/s) just below the Moho indicating a high percentage of melts and magmas (Panza *et al.*, 2007a). In general, the shallow asthenosphere beneath the Tyrrhenian supports the extension process in act following the eastward migration of Apenninic subduction (Gueguen *et al.*, 1997; Doglioni *et al.*, 1999), as a result of the global westward motion of the lithosphere with respect to the underlying mantle (Panza *et al.*, 2010; Riguzzi *et al.*, 2010).

The active part of the Tyrrhenian basin (cells a0, a1, a2, A0, A1, A2, A3, B-2, B-1) is characterized by an eastward emerging LVZ from a depth of about 150 km to 30 km. The considerable thickness of the LVZ may be explained (Frezzotti *et al.*, 2009) not only by the presence of a wide front of basaltic magma, but more likely by the simultaneous presence of small fractions of volatile elements (e.g. CO_2). This hypothesis would support CO_2 non-volcanic emissions extended from the Tyrrhenian coast to the Apennines, in the zone of relatively low heat flow. We therefore interpret the central Tyrrhenian LVZ as induced by the presence of carbonate-rich melts. In this picture the bottom of the LVZ at a depth of 130-150 km likely represents the beginning of a partially-melt mantle, while its upper margin, at about 30 km depth, likely represents the upper limit of the melt's ascent. To the east the LVZ vanishes in cell B5 (Paola basin), where a tick LID (V_S about 4.70 km/s) between 90 km and 160 km of depth likely represents the subducting Ionian slab (Panza *et al.*, 2003) as also supported by deep seismicity.

Evidence of subducting slab is clear along all the Calabrian Arc (cells C5, C6 and B6).

The Hellenic subduction is well delineated (cells A10, B9 and C9) by an eastward thickening lithosphere. In cell B9 a lithospheric doubling is present: a lithospheric layer extends down to about 90 km of depth, lying on an asthenospheric layer (V_S about 4.35 km/s), below which we find another lithospheric layer (V_S about 4.70 km/s) which extends down to about 220 km of depth, where a LVZ starts.

In general, the arc-shaped Ionian-Adria lithosphere supports a strong connection between Hellenic subduction and Ionian-Tyrrhenic subduction, possibly endorsing an upduction-subduction counterflow mechanism in the upper mantle (Doglioni *et al.*, 2007; Scalera, 2007), which discussion is not within the scope of this paper.

Discussion of selected cross-sections

A detailed geodynamical interpretation for several profiles across the study area is elaborated using the obtained structural model. Some of these interpretations are developed starting from seismic reflection experiments profiles (e.g. CROP-ECORS and TRANSALP), others starting from geological sketches. The location of the sections is shown in Fig. 13. The aim of this effort is to enlighten and better understand the geodynamical setting in the Italic region, combining geophysical data (i.e. V_S structural models) with geological interpretation and correlating them with heat flow and gravimetric data.

Figure 13. Interpreted sections.

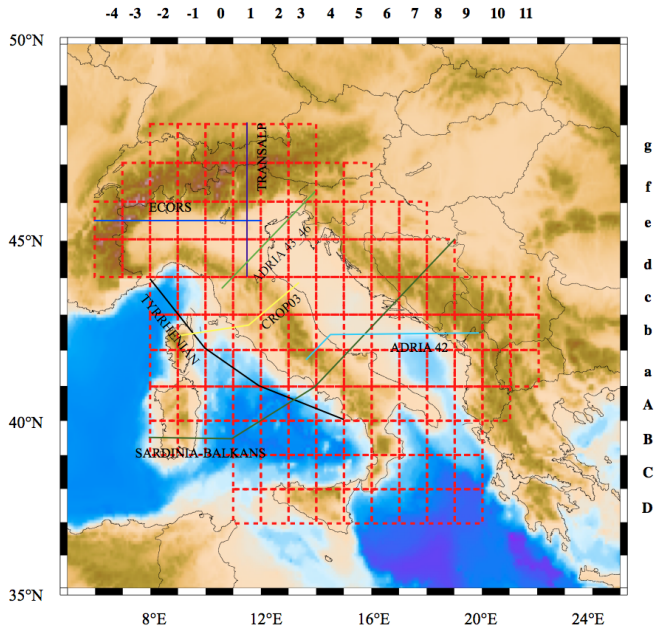

Location of the interpreted sections presented in this paper, Figs. 14, 15, 16, 17, 20, 21, 22.

The section ECORS (Fig. 14), in the Western Alps, has been extended, to the east, to the Adriatic coast. This section allows to investigate the lithospheric-asthenospheric structure resulting from the European-Adriatic plates collisional process in the Western Alps, with a thick lid subducting eastward, marked by strong negative gravimetric anomalies. The presence of lithospheric roots is speculated in cells e-2 and e-1s (Milan), where an almost constant V_S sequence extends to about 280 km of depth. In the same cells the V_S of about 4.35 km/s between 90 km and 140 km depth likely indicates partial melting according to pyrolite phase diagram (Green and Ringwood, 1967). More to the east, just beneath the Moho, a 15-20 km thick mantle wedge is present (V_S 4.00-4.20 km/s), possibly connected to the dehydration process of the downwelling slab. In cell e0 a LVZ (V_S about 4.00 km/s) is clearly seen beneath the Garda zone at depth between 180 and 260 km, in accordance with the high heat flux and volcanism of the Eugani hills.

Figure 14. ECORS section.

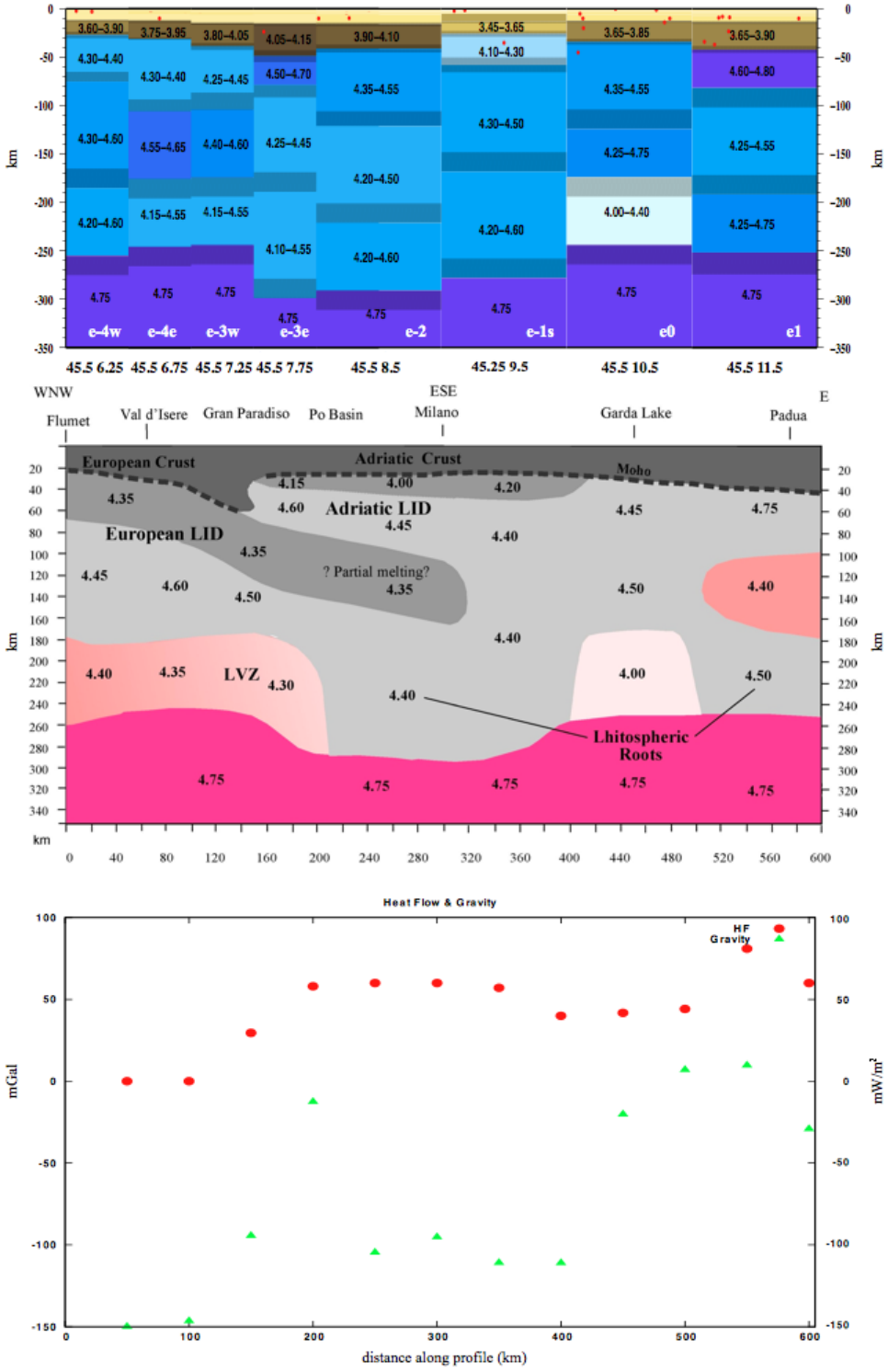

Top: Cellular model of the drawn section along ECORS profile. Yellow to brown colors represent crustal layers, blue to violet colors indicate mantle layers. Red dots denote all seismic events collected by ISC with magnitude greater than 3 (1904-2006). For each layer V_S variability range is reported. For the sake of clarity, in the uppermost crustal layers the values of V_S are omitted. The error on thickness is represented by texture. All the values are reported in Appendix C.

Centre: Interpretation of the model (modified after Schmid and Kissling, 2000). The V_S value reported may not necessarily fall in the centre of the V_S range gained from inversion.

Bottom: Heat flow (mWm^{-2},red full circles) and gravimetric anomaly (mGal, green triangles) data along profile used to support our interpretation.

The collisional process is clearly visible along the TRANSALP profile (Fig. 15), across the Central Alps. This section is extended to the Apennines in order to depict a complete cross-section of the Po Plain. Major elements highlighted are the subduction of the European lid beneath the Adriatic plate, well evidenced by a relatively fast V_S-body dipping southward with significant crustal thickening beneath the Dolomites. The asthenospheric LVZ is well visible under both the European and Adriatic plates, in the former ranging between 150 km and 250 km of depth, in the latter from 90 km to 260 km. The negative gravity anomalies beneath Austro-Alpine (cells g1s and f1) and Apennines (cell d1) are well compatible with the presence of a sinking slab.

The Adriatic plate is also involved in two distinct tectonic processes: the south-westward or westward subduction beneath the Apennines and north-eastward subduction beneath the Dinarides.

Figure 15. TRANSALP section.

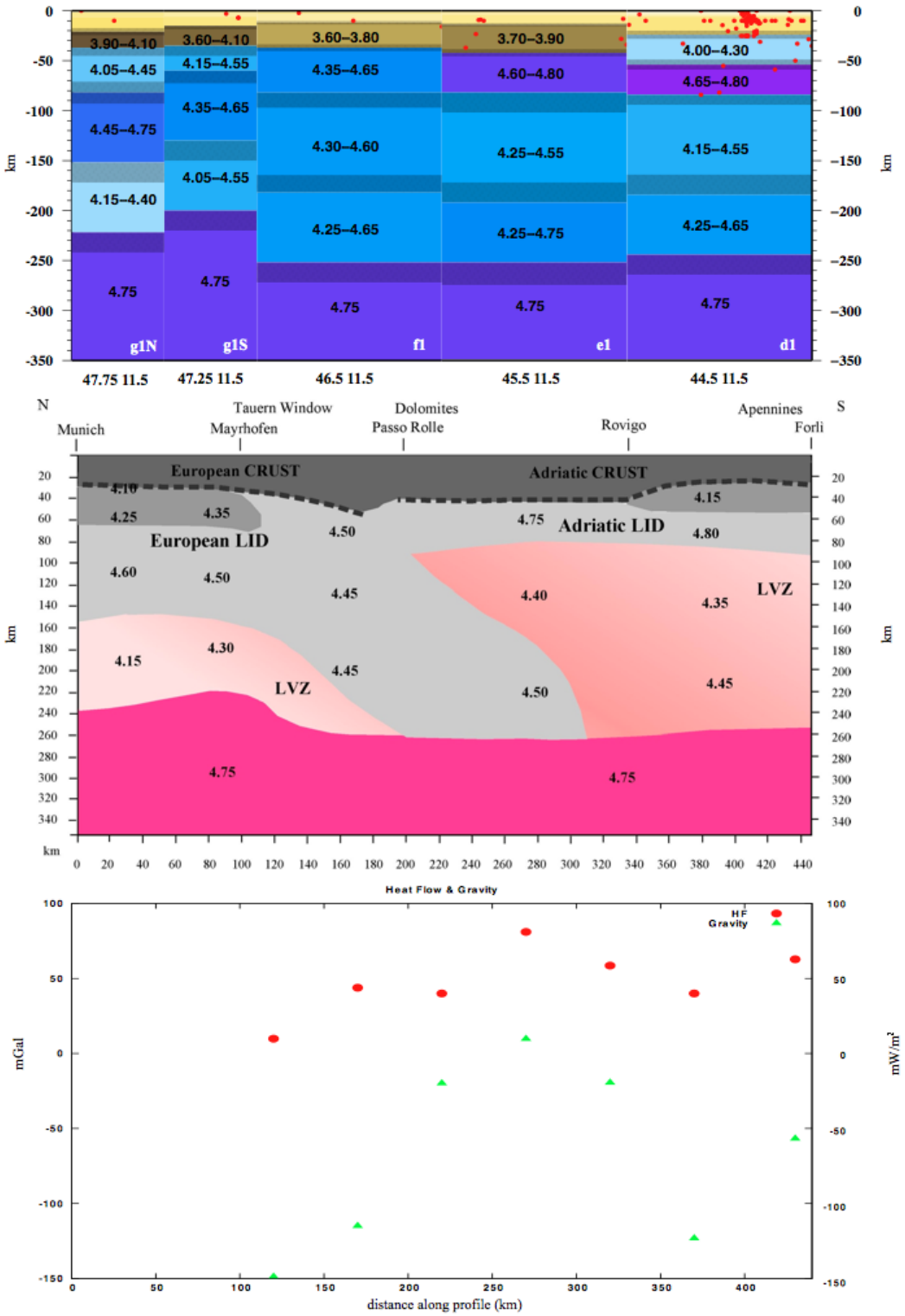

Top: Cellular model of the drawn section along TRANSALP profile. Yellow to brown colors represent crustal layers, blue to violet colors indicate mantle layers. Red dots denote all seismic events collected by ISC with magnitude greater than 3 (1904-2006). For each layer V_S variability range is reported. For the sake of clarity, in the uppermost crustal layers the values of V_S are omitted. The error on thickness is represented by texture. All the values are reported in Appendix C.

Centre: Interpretation of the model. The V_S value reported may not necessarily fall in the centre of the V_S range gained from inversion.

Bottom: Heat flow (mWm^{-2}, red full circles) and gravimetric anomaly (mGal, green triangles) data along profile used to support our interpretation.

The subduction beneath the Apennines (Fig. 16) is well modelled by the Adriatic Moho deepening and by a lid with V_S about 4.50-4.70 km/s that reaches a depth of about 180 km beneath the north-eastern Apennines. A relatively fast asthenosphere extends beneath the Adriatic lithosphere, and the lower velocity (V_S about 4.00 km/s) is reached above the sinking slab, likely witnessing of dehydration processes. Although in the northern Adriatic three distinct subduction zones coexist, (i.e. the Alpine, Apenninic and Dinaric) the Apenninic subduction seems to have a dominant role due to its present eastward migration, as marked by high seismicity and by the thickening toward NE of the Pliocene-Pleistocene sediments (Cuffaro *et al.*, 2009).

Figure 16. ADRIA 43_46 section.

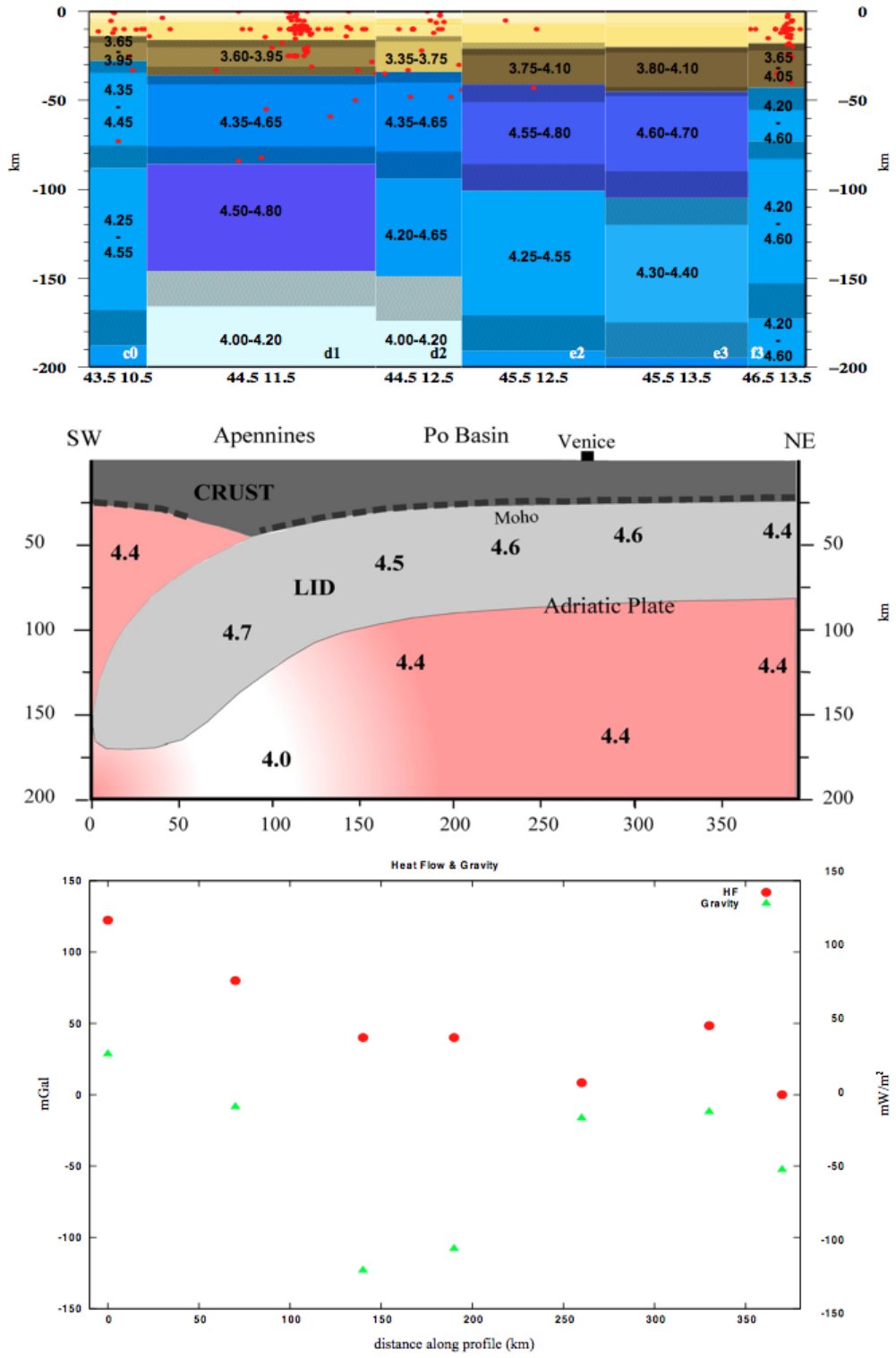

Top: Cellular model of the drawn section across Northern Adriatic. Yellow to brown colors represent crustal layers, blue to violet colors indicate mantle layers. Red dots denote all seismic events collected by ISC with magnitude greater than 3 (1904-2006). For each layer V_S variability range is reported. For the sake of clarity, in the uppermost crustal layers the values of V_S are omitted. The error on thickness is represented by texture. All the values are reported in Appendix B.

Centre: Interpretation of the model, after a sketch of Cuffaro *et al.*, 2009. The V_S value reported may not necessarily fall in the centre of the V_S range gained from inversion.

Bottom: Heat flow (mWm^{-2},red full circles) and gravimetric anomaly (mGal, green triangles) data along profile used to support our interpretation.

The eastward migration of the Apenninic subduction likely causes loss of lithospheric material that should be replaced by uprising asthenospheric material (Doglioni *et al.*, 1999). This is clearly evinced by the CROP03 profile (Fig. 17), where the Tyrrhenian asthenosphere rises up to 30 km depth, much shallower than the Adriatic asthenosphere, observed below about 90 km depth. The shallow Tyrrhenian asthenosphere feeds the Tuscan volcanism, as also marked by the high heat flow. On the contrary, very low heat flow and negative gravimetric anomalies characterize the subducting Adriatic lithosphere (cells c2 and c3) (Suhadolc *et al.*, 1994), marked by a V_S about 4.40-4.60 km/s and intermediate depth seismicity. In order to have a better understanding of the local stress field, and therefore of the geodynamic setting, the recent most damaging seismic events happened in the area (mostly Umbria-Marche seismic sequence of 1997), have been inverted with the INPAR method (Guidarelli and Panza, 2006) and superimposed on the section (Fig. 17). The detailed information about the moment tensor solutions for the events shown in Fig. 17 are given in Appendix D. Besides prevalent shallow normal faulting seismicity (Chimera *et al.*, 2003), thrust-faulting intermediate depth seismicity is present in the subducting slab. An enlightening example of the improved resolving power of the INPAR method with respect to shallow, usually fixed, events, discussed in section “Methodology”, comes from the re-inversion of an event of the strong damaging Umbria-Marche seismic sequence in 1997 (event 4, Fig 17): the event, which occurred on October 6th, at 11:24:52 p.m. (43.06°N 12.80°E) is reported by CMT and RCMT bulletins as a normal-fault mechanism with depth fixed at 10 and 15 km, respectively. INPAR inversion determined a thrust-fault mechanism with a deeper focus, at depth of 27 km. (Fig. 18) To prove our argument we performed the inversion again, constraining the depth interval at 2-10 km and 2-16 km respectively: as we could expect, the former inversion gives a normal fault mechanism at 2 km depth, while the latter gives a thrust fault mechanism at 16 km depth, therefore at the deepest limit of our fixed interval, suggesting to search for a deeper focus (Fig. 19).

Figure 17. CROP03 section.

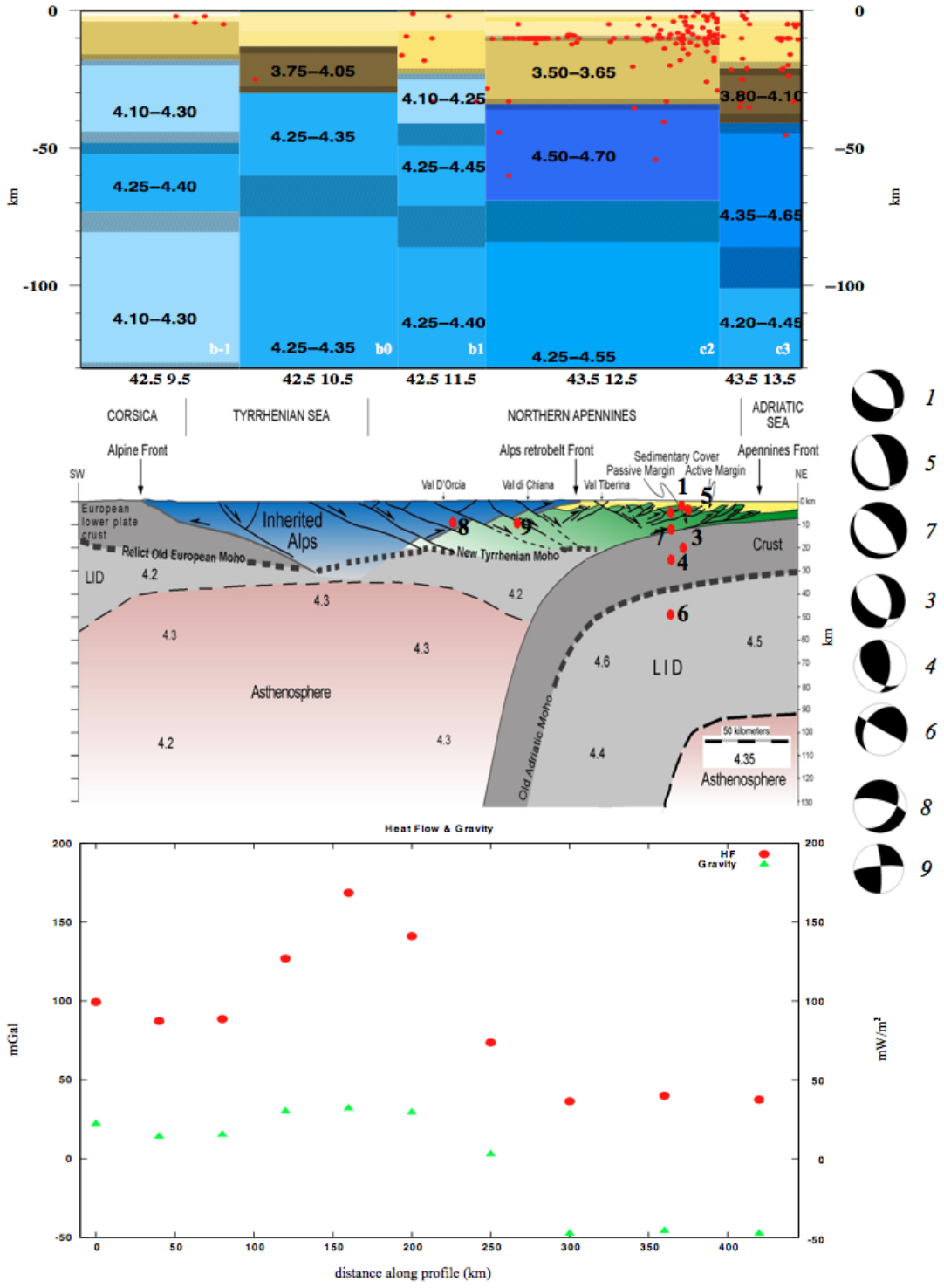

Top: Cellular model of the drawn section along CROP03 profile. Yellow to brown colors represent crustal layers, blue to violet colors indicate mantle layers. Red dots denote all seismic events collected by ISC with magnitude greater than 3 (1904-2006). For each layer V_S variability range is reported. For the sake of clarity, in the uppermost crustal layers the values of V_S are omitted. The error on thickness is represented by texture. All the values are reported in Appendix B.

Centre: Interpretation of the model, modified after Carminati and Scrocca (2004). The V_S value reported may not necessarily fall in the centre of the V_S range gained from inversion. The plotted hypocenters, and their focal mechanisms (on the right side), are retrieved by INPAR moment tensor inversion (see Appendix D for details).

Bottom: Heat flow (mWm^{-2},red full circles) and gravimetric anomaly (mGal, green triangles) data along profile used to support our interpretation.

Figure 18. CMT vs INPAR focal mechanisms.

The focal mechanism for the event of October 6th, 1997 at 11:24:52 p.m. (43.06°N 12.80°E), Umbria-Marche sequence, as retrieved by CMT (nodal planes: 149 23 -73/310 68 -97) (left) and INPAR (nodal planes: 135 41 52/1 59 118) (right). The focal depth, fixed by CMT, is 10 and 27 km, respectively. The different resolving power of the two inversion methods determines an opposite focal mechanism, normal-faulting the former, thrust faulting the latter.

Figure 19. INPAR vs depth focal mechanisms.

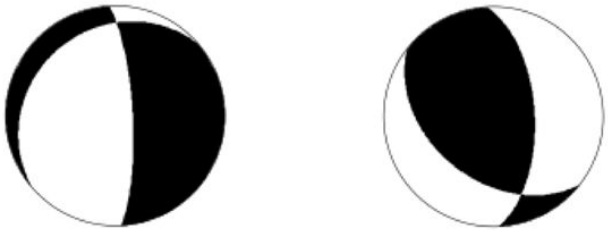

The same event of Figure 18 inverted with the INPAR method constraining depth at two different intervals: 2-10 km (nodal planes: 229 21 -40/357 77 -106) (left) and 2-16 km (nodal planes: 128 42 50/357 59 120) (right). The retrieved depth is 2 km and 16 km, respectively. The focal mechanism is opposite: normal the former (left), thrust the latter (right). The wrong fault-plane solution is determined constraining the event at shallow depth (see Appendix D for details).

The two opposing-side subduction processes of the Adriatic plate under the Apennines and Dinarides are clearly distinguishable in Fig. 20, which is a cross section of the Adriatic at about 42°N latitude. The westward Apenninic subduction is highlighted by relatively fast (V_S 4.40-4.60 km/s) lithosphere dipping to the west, marked by relatively low heat flow and negative gravity anomaly. A mantle wedge (V_S about 4.20 km/s) is likely to be present at the top of the subducting lithosphere, in the upper plate, as a result of both dehydration and mantle compensation. To the east, the lithosphere gets thinner, with partial melt likely to be present offshore Adriatic at about 50 km depth (V_S 4.20 km/s), with relatively high heat flow and positive gravity anomaly possibly associated to rifting process. To the east of the Dalmatian islands, the lithosphere gets gradually thicker, due to the north-eastward directed subduction with a lower dip angle compared to the Apennines subduction. According to Cuffaro *et al.* (2009), the Dinarides are older than the Appenines, but they were downward tilted by the eastward migration of the Apennines subduction hinge and the thrust-belt front, after being sub-aerially eroded, has been subsided.

Figure 20. ADRIA 42 section.

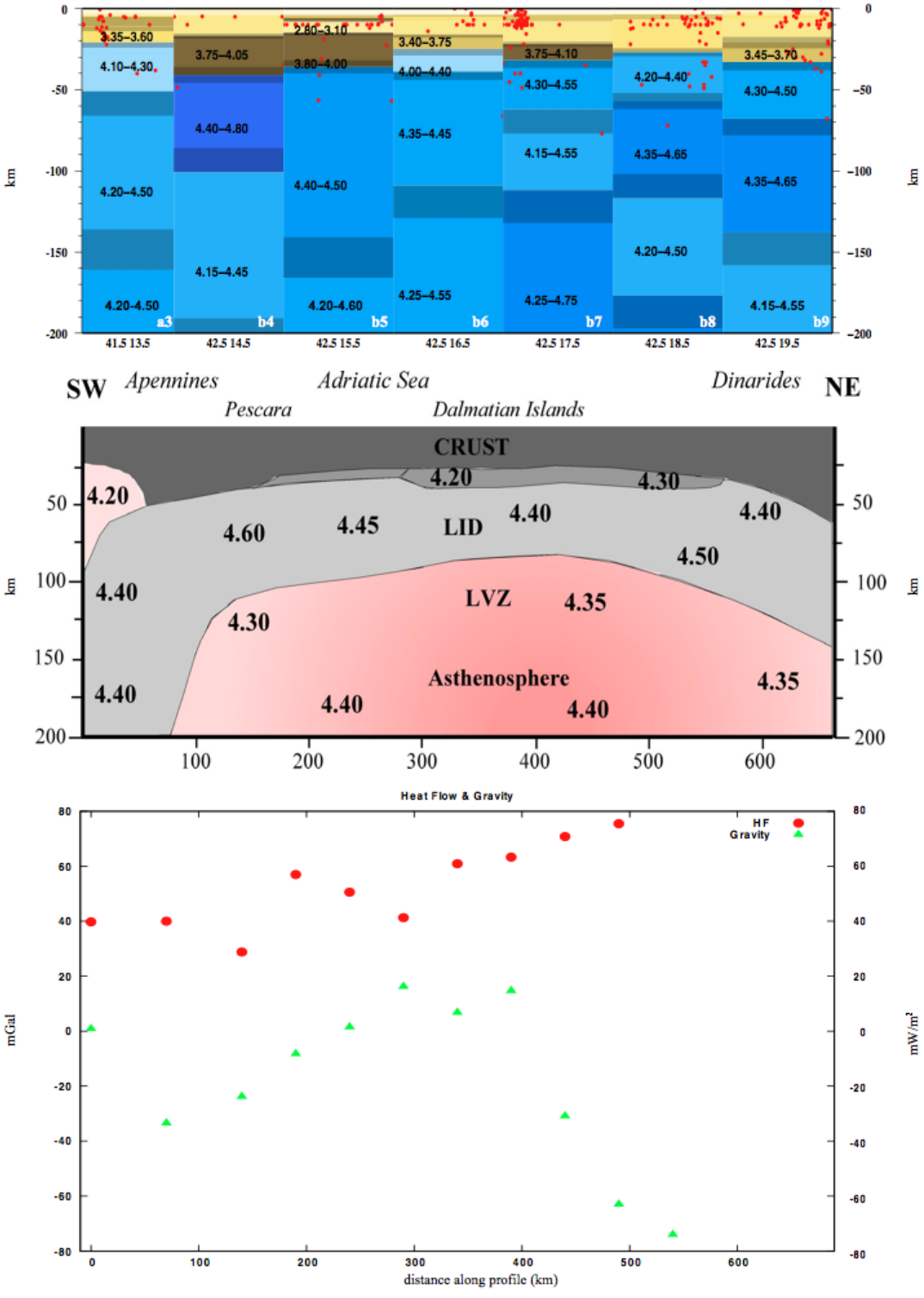

Top: Cellular model of the drawn section across central Adriatic. Yellow to brown colors represent crustal layers, blue to violet colors indicate mantle layers. Red dots denote all seismic events collected by ISC with magnitude greater than 3 (1904-2006). For each layer V_S variability range is reported. For the sake of clarity, in the uppermost crustal layers the values of V_S are omitted. The error on thickness is represented by texture. All the values are reported in Appendix B.

Centre: Interpretation of the model, after a sketch of Cuffaro *et al.*, 2009. The V_S value reported may not necessarily fall in the centre of the V_S range gained from inversion.

Bottom: Heat flow (mWm^{-2},red full circles) and gravimetric anomaly (mGal, green triangles) data along profile used to support our interpretation.

The same process can be seen in Fig. 21, that is, a SW-NE trending profile from Tyrrhenian to the Sava Basin. The westward subducting Apenninic lithosphere is almost vertically bent by the mantle easterly directed flow, while the Dinaric eastward subduction has a dip angle of about 20-30°, as discussed in detail by Doglioni *et al.* (1999) and Carminati *et al.* (2004). A mantle wedge is visible in both upper plates of the Dinaric and Apenninic subductions by low velocities layers (V_S 4.00 km/s and 4.20 km/s). To the west, the eastward retreat of the Apenninic subduction calls for a mantle compensation represented by the uprising LVZ beneath the Tyrrhenian Sea. This shallow asthenospheric material directly feeds Tyrrhenian volcanoes as Magnaghi and Ischia, as fairly supported by heat flow peaks.

Figure 21. SARDINIA-BALKANS section.

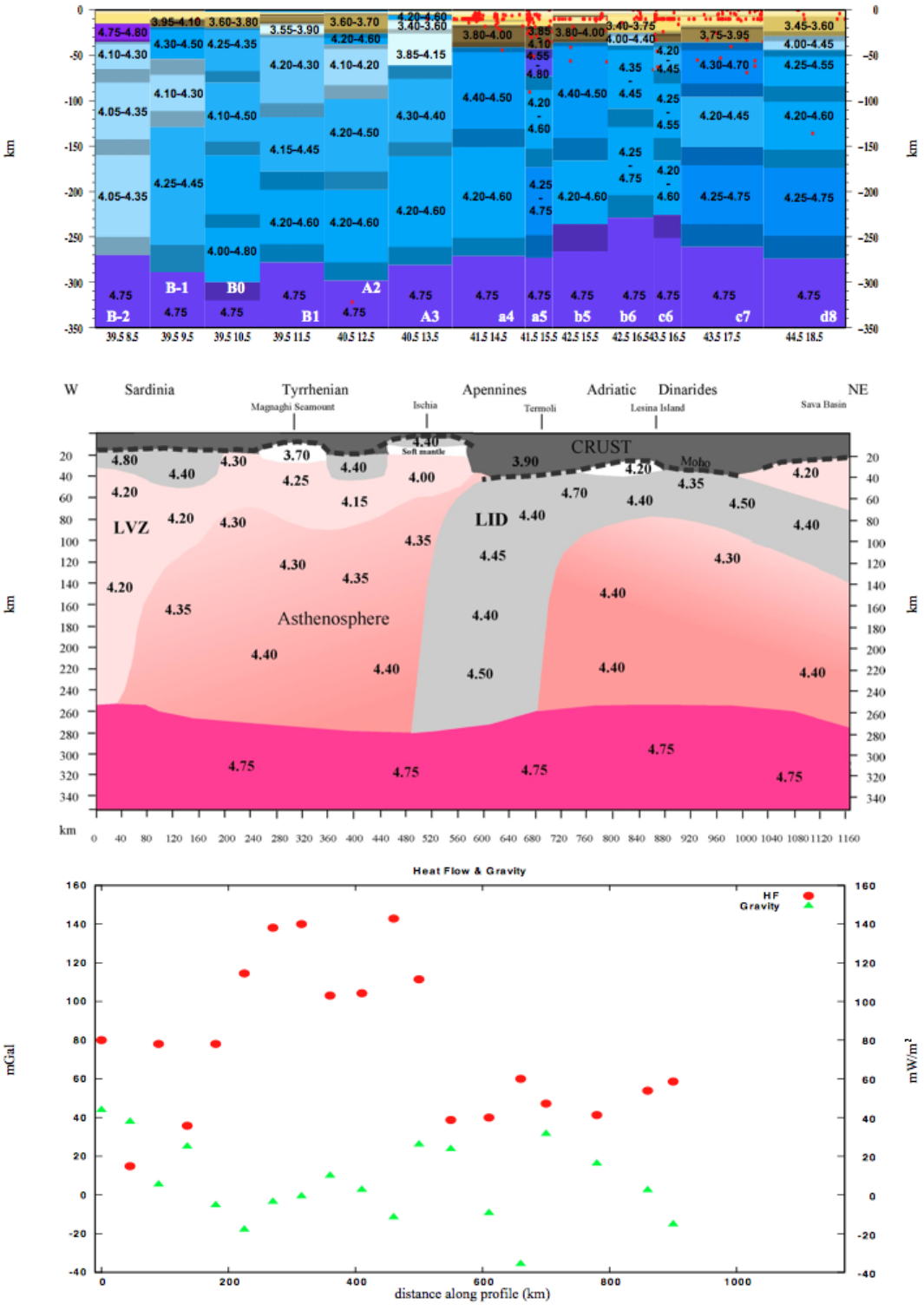

Top: Cellular model of the drawn section from Sardinia to Balkans. Yellow to brown colors represent crustal layers, blue to violet colors indicate mantle layers. Red dots denote all seismic events collected by ISC with magnitude greater than 3 (1904-2006). For each layer V_S variability range is reported. For the sake of clarity, in the uppermost crustal layers the values of V_S are omitted. The error on thickness is represented by texture. All the values are reported in Appendix B.

Centre: Interpretation of the model. The V_S value reported may not necessarily fall in the centre of the V_S range gained from inversion.

Bottom: Heat flow (mWm^{-2},red full circles) and gravimetric anomaly (mGal, green triangles) data along profile used to support our interpretation.

It is well known that the Tyrrhenian Sea started opening about 15 Ma, as the result of the backarc expansion (Scandone, 1980; Gueguen *et al.*, 1997 and reference therein) process induced by the eastward migration of the Apenninic subduction (Royden and Burchfield, 1989; Doglioni, 1991), which took place in the late Oligocene on the preexisting alpine-betic orogen. The Tyrrhenian Sea is still opening, with age of the newly formed oceanic lithosphere decreasing from west to east. This process was likely inhomogeneous and asymmetric. Clear evidence of this are the numerous "boudins" disseminated in the basin at different scales. A "boudin" is a continental isolated block, common at the mesoscale, as the product of extension of a competent layer (i.e. with high resistance to deformation and loss of thickness) within a less competent matrix (Ramsay and Huber, 1983, and references therein). The "boudins" are bounded by thinned areas (necks) where material with lower viscosity flows.

The distance between "boudins" is in the order of the original lithospheric thickness, ranging from 100 to 400 km as argued in Gueguen *et al.* (1997). The most prominent one is the Sardinia-Corsica block (Fig. 21, cells a-2, A-1, B-1), where the lithosphere preserves its original thickness (about 70 km), which represents a fragment of the Betic foreland. To the east a thin neck extends with a lithospheric thickness of about 25-30 km (Magnaghi basin) down to cell A2, where an intra-Tyrrhenian "boudin" is located, likely representing a fragment of the hinterland of the previous Alpine-Betic orogen. Generally crustal thickness reflects the lithospheric thickness, being about 20-25 km beneath "boudins", and 10-15 km and even less beneath necks. Another intra-Tyrrhenian "boudin" is located in cell a0 (see Figure 22), with a thin neck that separates it from cell A2.

Figure 22. Tyrrhenian section.

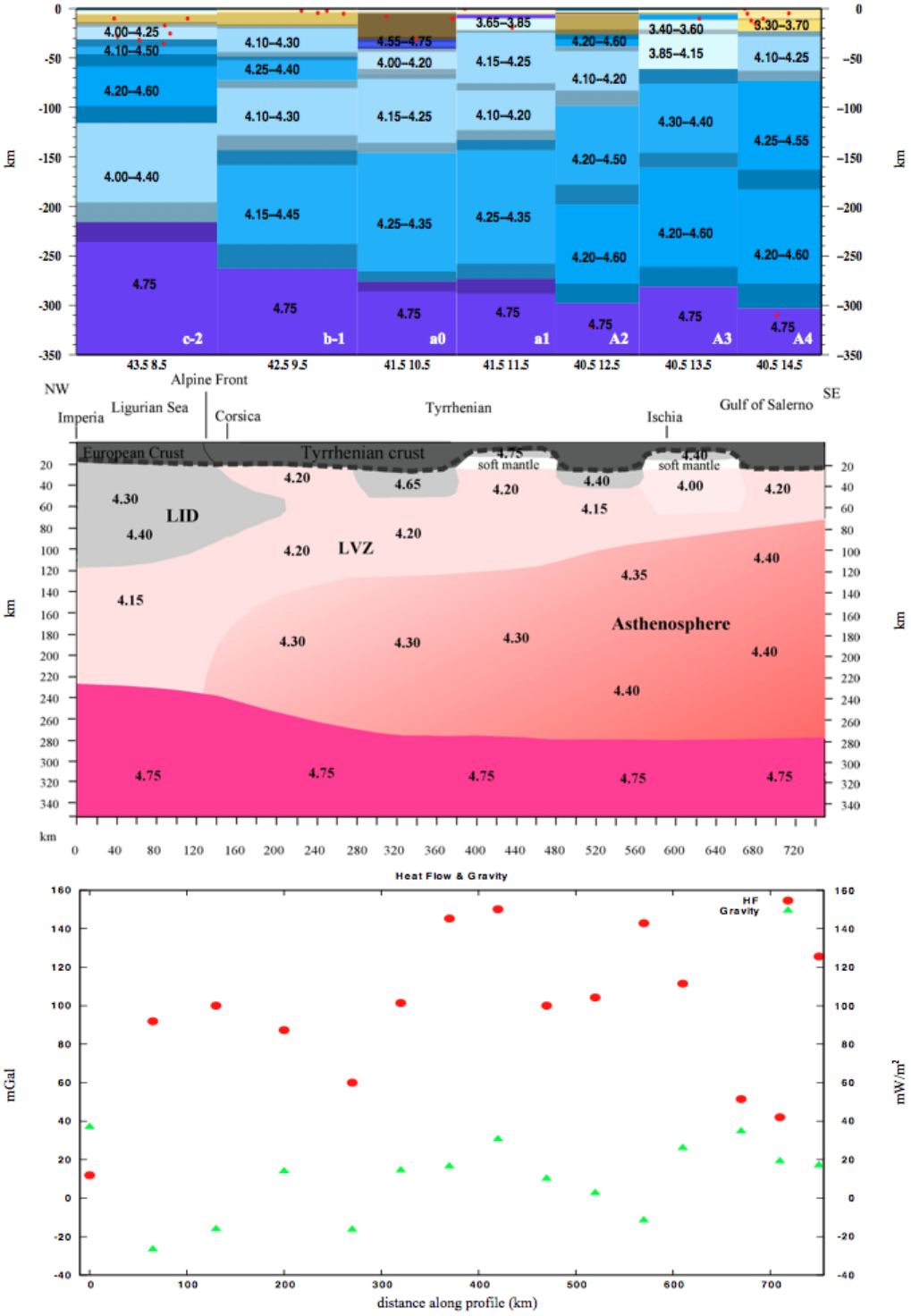

Top: Cellular model of the drawn section across Tyrrhenian. Yellow to brown colors represent crustal layers, blue to violet colors indicate mantle layers. Red dots denote all seismic events collected by ISC with magnitude greater than 3 (1904-2006). For each layer V_S variability range is reported. For the sake of clarity, in the uppermost crustal layers the values of V_S are omitted. The error on thickness is represented by texture. All the values are reported in Appendix B.

Centre: Interpretation of the model. The V_S value reported may not necessarily fall in the centre of the V_S range gained from inversion.

Bottom: Heat flow (mWm^{-2}, red full circles) and gravimetric anomaly (mGal, green triangles) data along profile used to support our interpretation.

Below, along the NE-SW direction of the Tyrrhenian expansion, a rising LVZ is present, likely representing the eastward mantle flow gradually emerging in the hanging wall of the Apennines retreating slab.

Heat flow and gravimetric data substantially support this picture, with the highest peak of heat flow below Magnaghi, Ischia and cell a1, likely feeding the Alban Hills, and evident gravimetric negative anomalies corresponding to the "boudins".

Conclusions

We propose a structural model for the lithosphere-asthenosphere system of Italy and neighbouring areas by means of V_S-depth distribution. The multidisciplinary approach is used to better constrain our model to the independent geological, geophysical and petrological information. The obtained picture of the lithosphere-asthenosphere system confirms the existence of some known features: the lithospheric roots in the western and central Alps, the extended LVZ beneath the Tyrrhenian Sea, steep subduction beneath Calabrian arc, low-angle subduction under the Dinarides.

New evidence reinforces the hypothesis of an asymmetric expansion process of the Tyrrhenian Sea, as the presence of the lithospheric "boudinage" extended along a NW-SE direction through the whole Tyrrhenian Sea, likely representing fragments of the Alpine-Betic collision dragged by the eastward migrating process of the Apennines subduction. Another feature enlightened is the easterly rising shallow low-velocity layer from about 140 km to about 30 km in the Tyrrhenian active part of the backarc basin.

Further proofs for undergoing subduction processes of the Adriatic lithosphere towards northeast beneath the Dinarides and toward the west beneath the Apennines, with significantly different dip angles, corroborate the existence of a global asymmetry between the eastward and westward subduction processes, induced by the eastward relative mantle flow.

The Tertiary to Present subduction processes in the Italian area occurring on a Mesozoic disrupted lithosphere can account for the relevant lateral anisotropies visible in the mantle.

The arc-shaped Ionian-Adriatic lithosphere supports a strong connection between Hellenic subduction and Ionian-Tyrrhenic subduction, possibly endorsing an upduction-subduction counterflow mechanism in the upper mantle.

A wide use of seismicity analysis, both from catalogues and moment tensor inversion by the INPAR method, represents a significant constraint to the model interpretation. INPAR allows the use of relatively short period waveforms, significantly improving the depth determination for shallow events, usually fixed by CMT and RCMT. The depth and the focal mechanism of a significant damaging event of Umbria-Marche sequence are drastically changed with respect to CMT and RCMT determinations, leading to a better comprehension of the local stress field.

Acknowledgments

This research has benefited from funding provided by the Italian Presidenza del Consiglio dei Ministri - Dipartimento della Protezione Civile (DPC). Scientific papers funded by DPC do not represent its official opinion and policies.

This research has benefited form founding provided by Italian Ministero dell'Istruzione, dell'Università e della Ricerca PRIN 2008. The authors are grateful to Chiara D'Ambrogi for kindly sharing heat flow and gravimetric data.

References

Aki, K., Richards, P.G. (1980). Quantitative Seismology, Freeman and Co. New York.

Anderson, D. (2007). New Theory of the Earth. Cambridge University Press.

Anderson, D., 2007. The eclogite engine: Chemical geodynamics as a Galileo thermometer. Geological Society of America Special Papers 430, 47-64.

Bottinga, Y., Steinmetz, L., 1979. A geophysical, geochemical, petrological model of the sub-marine lithosphere. Tectonophysics 55, 311-347. 10.1016/0040-1951(79)90182-3

Boyadzhiev, G., Brandmayr, E., Pinat, T., Panza, G.F., 2008. Optimization for non linear inverse problem. Rendiconti Lincei: Sci. Fis. e Nat. 19, 17-43.

Bukchin, B.G., Mostinskii, A.Z., 2007. Integral Source Characteristics of the Sumatra Earthquakes of December 26, 2004, and March 28, 2005 Journal of Volcanology and Seismology 1, 4, 263-273.

Carminati E., Doglioni C., Scrocca, D., 2004. Alps Vs Apennines. Special volume of the Italian Geological Society for IGC 32 Florence.

Chimera G., Aoudia A., Saraò A., Panza, G.F., 2003. Active tectonics in central Italy: constraint from surface wave tomography and source moment tensor inversion. Phys. Earth Planet. Inter. 138:241-262.

Craglietto A., Panza G.F., Mitchell B.J, Costa G., 1989. Anelastic properties of the crust in the Mediterranean area. American Geophysical Union Geophysical Monograph 51 IUGG 6, 179-196.

Cuffaro M., Doglioni C., Riguzzi, F., 2009. Present geodynamics of the northern Adriatic plate. Rendiconti online Soc. Geol. It. 3.

Della Vedova, B., Bellani, S., Pellis, G., Squarci, P., 2001. Deep temperatures and surface heat flow distribution. In Anatomy of an orogen (Vai & Martini Eds.).

Dezes, P., Ziegler, P., 2001. Map of the European Moho. EUCOR URGENT.

Doglioni, C., 1991. A proposal of kinematic modelling for W-dipping subductions - Possible applications to the Tyrrhenian-Apennines system. Terra Nova 3, 423-434. 10.1111/j.1365-3121.1991.tb00172.x

Doglioni, C., Gueguen, E., Harabaglia, P., Mongelli, F., 1999. On the origin of west-directed subduction zones and application to the western Mediterranean. In: Durand, Jolivet, Horváth, Séranne The Mediterranean Basins: Tertiary Extension within the Alpine orogen. Geological Society of London 156, 541-561.

Doglioni, C., Carminati, E., Cuffaro, M. and Scrocca, D., 2007. Subduction kinematics and dynamic constraints. Earth Science Reviews, 83, 125-175.

Du, Z.J., Michelini, A., Panza, G.F., 1998. EurID: a regionalized 3D seismological model of Europe. Phys. Earth Planet. Inter. 105, 31-62.

Farafonova, Y. G., Panza, G. F., Yanovskaya, T. B., Doglioni, C., 2007. Upper Mantle Structure in the Alpine Zone from Surface Wave Tomography. Doklady Earth Science, Vol. 416, No. 7, 1114-1117.

Farina, B.M., 2006. Lithosphere-asthenosphere system in Italy and surrounding areas: optimized non-linear inversion of surface-wave dispersion curves and modelling of gravity bouguer anomalies. Phd Thesis, University of Trieste.

Florsch, N., Fäh, D., Suhadolc, P., Panza, G.F., 1991. Complete synthetic seismograms for high-frequency multimode SH-waves. Pure and Applied Geophysics, 136, 529-560.

Frezzotti, M.L., Peccerillo, A., Panza, G.F., 2009. Carbonate matasomatism and CO2 lithosphere-asthenosphere degassing beneath the Western Mediterranean: An integrated model arising from petrological and geophysical data. Chemical Geology 262, 108-120. 10.1016/j.chemgeo.2009.02.015

Gasperini, P., 2002. Local magnitude revaluation for recent Italian earthquakes (1981-1996). J. Seismol. 6, 503-524.

Gennesseaux, M., Burollet, P., Winnock, E., 1998. Thickness of the Plio-Quaternary sediments (IBCM-PQ). Boll. Geofis. Teor. Appl. 39, 243-284.

Grad, M., Tiira, T., 2008. The Moho depth map of the European Plate. Geophysical Journal International 176 l, 279-292.

Green, D.H., Ringwood, A.E., 1967. The genesis of basaltic magmas. Springer Contributions to Mineralogy and Petrology 15 2, 103-190.

Gueguen, E., Doglioni, C., Fernandez, M., 1997. Lithospheric boudinage in the Western Mediterranean back-arc basin. Terra Nova 9, 184-187. 10.1046/j.1365-3121.1997.d01-28.x

Guidarelli, M., Panza, G.F., 2006. INPAR, CMT and RCMT seismic moment solutions compared for the strongest damaging events (M≥4.8) occurred in the Italian region in the last decade. Rendiconti Accademia Nazionale delle Scienze detta dei XL Memorie di Scienze Fisiche e Naturali 124 Vol. XXX P. II, 81-98.

Hurting, E., Cermak, V., Haenel, R. and Zui, V. (eds), 1991. Geothermal Atlas of Europe. Hermann Haack Verlag, Gotha, 156 pp.

ISC (2007). International Seismological Centre. http://www.isc.ac.uk.

ISPRA, ENI, OGS (2009). Cartografia Gravimetrica Digitale d'Italia alla scala 1:250.000.

Kennett, B.K.N., Engdahl, E.R., Buland, R., 1995. Constraints on seismic velocities in the earth from travel times. Geophys. J. Int. 122, 108-124. 10.1111/j.1365-246X.1995.tb03540.x

Knopoff, L., Panza, G.F., 1977. Resolution of upper mantle structure using higher modes of Rayleigh waves. Annales Geophysicae 30, 491-505.

Kravanja, S., Panza, G.F., Sílený, J., 1999. Robust retrieval of seismic point source time function. Geophysical Journal International 136, 385-394.

Kravanja, S., Batini, F., Fiordelisi, A., Panza, G.F., 2000. Full moment tensor retrieval from waveform inversion in the Larderello geothermal area. Pure and Applied Geophysics 157, 1379-1392. 10.1007/PL00001124

Laske, G., Masters, G., 1997. A global digital maps of sediment thickness. Eos, Trans. Am. Geophys. Union 78 F483

Levshin, A.L., Yanovskaya, T.B., Lander, A.V., Bukchin, B.G., Barmin, M.P., Ratnicova, L.I., 1989. Surface Seismic Waves in Laterally Inhomogeneous Earth. In: Keilis-Borok VI (ed) Surface Seismic Waves in Laterally Inhomogeneous Earth. Kluiwer Publ. House, Dordrecht.

Martinez, M.D., Lana, X., Guinto, E.R., 2009. Elasto-anelastic regional structures of the crust and upper mantle beneath the Mediterranean basin derived from uncoupled casual inversion of rayleigh wave attenuation coefficient and group velocities. Geophysical research abstracts 11, EGU2009-2420.

Martinez, M.D., Lana, X., Guinto, E.R., 2010. Shear-wave attenuation tomography of the lithosphere-asthenosphere system beneath the Mediterranean region, Tectonophysics 481, 51-67.

Meletti, C. and Valensise, G., 2004. Zonazione sismogenetica ZS9 - App. 2 al Rapporto Conclusivo. In: Gruppo di Lavoro MPS (2004). Redazione della mappa di pericolosita` sismica prevista dall Ordinanza PCM 3274 del 20 marzo 2003. Rapporto Conclusivo per il Dipartimento della Protezione Civile, INGV, Milano-Roma, Aprile 2004, 65 pp. + 5 Allegati.

NEIC (2003) National Earthquake Information Center, US. http://earthquake.usgs.gov.

NGDC (2003) National Geophysical Data Center, US. http://www.ngdc.noaa.gov.

Panza, G.F., Muller, S., 1979. The plate boundary between Eurasia and Africa in the Alpine area. Memorie di Scienze Geologiche, Università di Padova, 33, 43–50.

Panza, G.F., 1981. The resolving power of seismic surface waves with respect to crust and upper mantle structural models. In: Cassinis R (ed) The solution of the inverse problem in geophysical interpretation. Plenum Press New York, 39-77.

Panza, G.F., 1985. Synthetic Seismograms: the Rayleigh Waves Modal Summation. Journal of Geophysics 58, 125-140.

Panza, G.F., Romanelli, F., Vaccari, F., 2000. Seismic wave propagation in laterally heterogeneous anelastic media: theory and applications to seismic zonation. Advances in Geophysics 43, 1-95. 10.1006/ageo.2001.0001

Panza, G.F., Pontevivo, A., Chimera, G., Raykova, R., and Aoudia, A., 2003. The lithosphere-asthenosphere: Italy and surroundings. Episodes. 26, 169–174.

Panza, G.F., Pontevivo, A., 2004. The Calabrian Arc: a detailed structural model of the lithosphere-asthenosphere system. Rend. Accad. Naz. Sci. XL Mem. Sci. Fis. Natur. 28, 51-88.

Panza, G.F., Peccerillo, A., Aoudia, A., Farina, B.M. (2007a). Geophysical and petrological modelling of the structure and composition of the crust and upper mantle in complex geodynamic settings: The Tyrrhenian Sea and surroundings. Earth-Science Reviews 80, 1-46.

Panza, G.F., Raykova, R.B., Carminati, E., Doglioni, C. (2007b). Upper mantle flow in the western Mediterranean. Earth. Planet. Sci. Lett 257, 200-214. 10.1016/j.epsl.2007.02.032

Panza, G.F., Raykova, R.B., 2008. Structure and rheology of lithosphere in Italy and surrounding. Terra Nova 20, 194-199. 10.1111/j.1365-3121.2008.00805.x

Panza, G.F., Doglioni, C., Levshin, A., 2010. Asymmetric ocean basins. Geology 38, 59-62. 10.1130/G30570.1

Peishan, C., Haitong, C., 1989. Scaling law and its applications to earthquake statistical relations. Tectonophysics, 188, 53-72.

Peter, D., Boschi, L., Deschamps, F., Fry, B., Ekström, G., Giardini, D., 2008. A new finite frequency shear-velocity model of the European-Mediterranean region. Geophys. Res. Lett, 35, L16315.

Piromallo, C., Morelli, A., 2003. P wave tomography of the mantle under the Alpine-Mediterranean area. Journal of Geophysical Research 108 (B2), 2065-2088. 10.1029/2002JB001757

Ponomarev, V.S., 2007. Denudation and Seismicity of the Earth s Crust. Doklady Earth Sci., 412, 19-21.

Pontevivo, A., Panza, G.F., 2006. The lithosphere-asthenosphere system in the Calabrian Arc and surrounding seas- Southern Italy. Pure Appl. Geophys. 163, 1617-1659.

Ramsay, J.G., Huber, M.I., 1983. The techniques of modern structural analysis. Strain analysis London Academic Press 1.

Raykova, R.B., Panza, G.F., 2010. The shear-wave velocity structure of the lithosphere-asthenosphere system in the Iberian area and surroundings. Rendiconti Lincei di Scienze FF. NN. 10.1007/s12210-010-0077-1.

Richter, C.F. (1958). Elementary Seismology. W. H. Freeman and Co., San Francisco.

Riguzzi, F., Panza, G.F., Varga, P., Doglioni, C., 2010. Can Earth's rotation and tidal despinning drive plate tectonics? Tectonophysics 484, 60-73. 10.1016/j.tecto.2009.06.012

Ritzwoller M., Levshin, A.L., 1998. Eurasian surface wave tomography: group velocities. J. Geophys. Res. 103, 4839-4878.

Royden, L.H., Burchfiel, B.C., 1989. Are systematic variations in thrust belt style related to plate boundary process? (the western Alps versus the Carpathians). Tectonics 8, 51-62. 10.1029/TC008i001p00051

Scalera, G., 2007. A new model of orogenic evolution. Rend. Soc. Geol. It, 5, 214-218.

Scandone, P., 1980. Origin of the Tyrrhenian Sea and Calabrian Arc. Bollettino della Società Geologica Italiana 98, 27-34.

Schmid, S.M., Kissling, E., 2000. The arc of the Western Alps in the light of geophysical data on deep crustal structure: Tectonics, v. 19, 10, 62-85.

Sílený, J., Panza, G.F., Campus, P., 1992. Waveform inversion for point source moment tensor retrieval with optimization of hypocentral depth and structural model. Geophysical Journal International 109, 259 274.

Sílený, J., 1998. Earthquake source parameters and their confidence regions by a genetic algorithm with a "memory". Geophysical Journal International, 134, 228-242.

Suhadolc, P., Marson, I., Panza, G.F., 1994. Crust and upper mantle structural properties along the active Tyrrhenian rim. Memorie descrittive della carta geologica d'Italia 49.

Šumanovac, F., Orešković, J., Grad, M., ALP 2002 Working Group, 2009. Crustal structure at the contact of the Dinarides and Pannonian basin based on 2-D seismic and gravity interpretation of the Alp07 profile in the ALP 2002 experiment. Geophys. J. Int. 179, 615-633.

Tesauro, M., Kaban, M.K., Cloetingh, S.A.P.L., 2008. EuCRUST-07: a new reference model for the European crust, Geophys. Res. Lett. 35.

Urban, L., Cichowicz, A., Vaccari, F., 1993. Computation of analytical partial derivatives of phase and group velocities for Rayleigh waves with respect to structural parameters. Stud. Geophys. Geod. 37, 14-36.

Van Keken, P.E., 2003. The structure and dynamics of the mantle wedge. Earth and planetary science letters 215, 323-338. 10.1016/S0012-821X(03)00460-6

Yanovskaya, T.B., 1997. Resolution estimation in the problems of seismic ray tomography. Izv. Phys. Solid Earth 33, 762-765.

Yanovskaya, T.B., 2001. In: Keilis-Borok, V.I., Molchan, G.M. (Eds.), Development of methods for surface-wave tomography based on Backus-Gilbert approach. Computational Seismology 32, 11-26.

A. The influence of uppermost crustal composition in the inversion process and obtained V_S structure.

The realistic modeling of uppermost crustal structure is very important in the non-linear inversion of the dispersion data and influences the obtained structures at mantle depths. One example is the inversion in cell b-1, in the Corsica offshore. The same dispersion data are used (phase velocities available in the period range 20 – 80 s and group velocities for 10 – 150 s with relevant single point errors) in two cases of the inversion. Since the smallest period is 10 seconds, the uppermost crust is not well resolved and its structure should be fixed using independent information. Two different parameterization of the uppermost crust (Table 2) are used and the obtained two sets of solutions have significant differences also in the mantle structure. Listed in Table 2 are values of V_P, V_S, thickness and density in the first five uppermost crustal layers that are kept fixed in the inversion. The following 5 layers are parameterized in both cases using five parameters for layer thicknesses, five parameters for V_S and one parameter for V_P/V_S ratio. The used parameterization in both cases (central values, steps, ranges) is listed in Table 3. The explored parameter space (grey area in Fig. 23) is similar in both cases.

Table 2. Parameterization of the uppermost crust

layer	I case				II case			
	h (km)	V_s (km/s)	V_p (km/s)	ρ (kg/cm^3)	h (km)	V_s (km/s)	V_p (km/s)	ρ (kg/cm^3)
1	0.06	0.00	1.50	1.03	0.06	0.00	1.50	1.03
2	2.94	1.20	2.25	2.10	1.44	1.20	2.10	2.10
3	0.50	1.50	2.60	2.20	0.03	1.35	2.35	2.20
4	1.30	3.85	6.66	2.60	1.00	2.80	4.80	2.45
5	1.20	3.95	6.84	2.80	1.00	3.00	5.20	2.55

Table 3. Central values, steps, ranges

parame-ters	I case				II case			
	V_p/V_s				V_p/V_s			
P_0	1.73				1.73			
	H^0 (km)	step (km)	H^{min}	H^{max}	H^0 (km)	step (km)	H^{min}	H^{max}
P_1	12.0	4.0	4.0	16.0	14.0	4.0	10.0	22.0
P_2	4.0	4.0	4.0	12.0	22.0	8.0	14.0	38.0
P_3	40.0	20.0	20.0	60.0	40.0	15.0	25.0	55.0
P_4	45.0	45.0	45.0	90.0	70.0	30.0	40.0	100.0
P_5	135.0	45.0	45.0	180.0	120.0	50.0	70.0	120.0
	V_S^0 (km/s)	step (km/s)	V_S^{min}	V_S^{max}	V_S^0 (km/s)	step (km/s)	V_S^{min}	V_S^{max}
P_6	4.50	0.25	2.25	4.75	3.60	0.15	2.25	4.30
P_7	3.35	0.15	3.20	4.95	4.20	0.20	3.60	4.80
P_8	4.30	0.15	3.70	4.75	4.30	0.15	3.85	4.90
P_9	4.00	0.20	3.80	5.00	4.40	0.20	4.00	4.80
P_{10}	4.35	0.15	3.60	5.10	4.30	0.30	4.00	4.90

Figure 23. Inversion results for cell b-1.

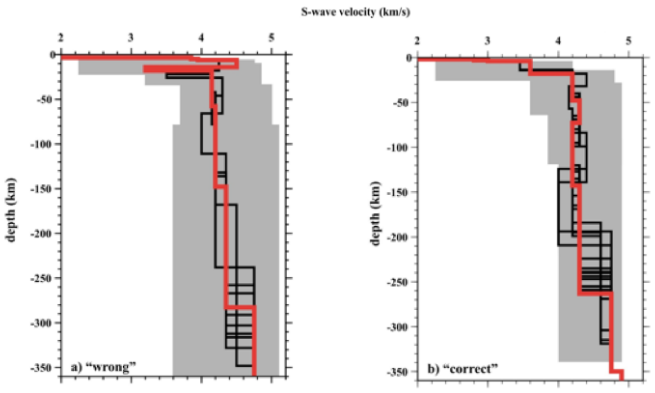

Non-linear inversion results for I case (a) and II case (b) of the uppermost fixed crust. V_S models that are solution of the inverse problem are shown with thin black lines and the selected cellular model is represented by thick red line. The grey areas delimit the explored parameter's space sampled by the simultaneous non-linear inversion of phase and group velocity of Rayleigh waves.

The obtained two sets of solutions are different not only in the shallow crustal structure but also at mantle depths (Fig. 23). In the first case the uppermost fixed crust is defined as the oceanic-like with layer of water, two sedimentary layers and two high-velocity layers (Tab. 4). In the case of the offshore of Corsica this is not realistic and the uppermost crust can be defined as "wrong". The obtained set of solutions for this case is shown in Fig. 23a. All accepted models have a high-velocity layer (V_S about 4.25-4.50 km/s) at depths of about 5-15 km. This layer is followed by thin, low-velocity layer (V_S about 3.2 km/s). The velocity in the mantle increases slightly with depth below 20 km. The representative solution selected by LSO (processing all cells of the study area) is presented by thick line in Fig 23a. It is characterized by high V_S (about 4.50 km/s) at depths of 5 to 15 km, followed by thin low velocity layer. Below 20 km of depth V_S increases from 4.15 to 4.75 km/s at about 280 km of depth. More realistic uppermost fixed crust is used in the second case of parameterization: water layer is the same and it is followed by sedimentary layers with increasing velocities and densities and upper crustal layer with V_P of 5.20 km/s. The obtained set of solutions (Fig. 23b) is consistent with the known geodynamical setting of the region and it is characterized by crustal layer with V_S of 3.45-3.60 km/s reaching depth of about 20 km. This layer is followed by mantle with V_S between 4.15 and 4.40 km/s and low-velocity layer with V_S about 4.00 – 4.20

km/s. The deeper mantle layer has V_S about 4.60 - 4.75 km/s and starts between 200 and 250 km of depth. The selected representative solution (thick line in Fig. 23b) has a crust about 20 km thick, a mantle lid about 50 km thick, a LVZ with V_S of 4.20 – 4.30 km/s located between 70 and 270 km of depth. The following layer has V_S about 4.75 km/s. This model is fairly consistent with the geological interpretation of the obtained V_S models along the section shown in Fig. 22 (see section "Discussion" for details).

The realistic modeling of the crustal layers especially at shallow depth has a very important role in the inversion process and is crucial for the realistic modeling of the upper mantle. The usage of "standard" crust in the inversion of tomographic data biases the results of the inversion also at depths below 100 km, especially in the regions with very complex structure as the study region.

B. V_S-depth model of the Italic region obtained after LSO.

V_S models obtained after the "hedgehog" inversion of surface-wave dispersion data and smoothing optimization are listed in Table 4. Each representative cellular model is presented in the table by the thickness h (km) and shear-wave velocity V_S (km/s) of the layers down to the depth of 350 km. The range of variability of h and V_S are given for inverted layers. The quantities are rounded off to 0.5 km for the thickness and to 0.05 km/s for V_S. The independent information is used to constrain the inversion, therefore the chosen solution does not necessarily fall in the centre of the range that can be smaller than the relevant parameter step. The used relation between V_S and V_P is constant for all dependent parameters in the inversion ($V_P / V_S = \sqrt{3}$), with the only exception of the cells A2, A3, B1, B2, B3, B4, where the relation $V_P / V_S = 2$ is used for the inverted mantle layers, according to Bottinga and Steinmetz (1979). The thickness marked by *** is not a truly inverted parameter, but it satisfies the condition that the total thickness from the free surface to the top of the fixed deep structure is equal to a predefined quantity H. In this study H=350 km according to the penetration depth of the used dispersion data. The structure deeper than H is the same for all the considered cells and is fixed according to the published model in Du *et al.* (1998).

Table 4a. Part I

h	Δh	Vs	ΔVs
11.5 37.5 D1			
0.6	-	0.00	-
2.5	-	1.73	-
2.0	-	2.90	-
0.9	-	3.40	-
3.0	-	3.40	-
5.0	5.0-6.0	3.25	3.15-3.35
15.0	15.0-17.0	3.90	3.85-3.95
15.0	15.0-20.0	4.30	4.25-4.40
110.0	90.0-110.0	4.45	4.40-4.50
110.0	85.0-110.0	4.40	4.35-4.45
86.0	***	4.75	-
12.5 37.5 D2			
0.5	-	0.00	-
2.5	-	1.85	-
2.0	-	2.65	-
1.0	-	2.89	-
1.0	-	2.89	-
10.0	10.0-13.0	3.60	3.45-3.70
12.0	12.0-18.0	3.70	3.50-3.90
30.0	30.0-45.0	4.50	4.45-4.55
110.0	90.0-110.0	4.40	4.40-4.45
110.0	90.0-110.0	4.40	4.25-4.55
71.0	***	4.75	-
13.5 37.5 D3			
0.5	-	1.73	-
2.0	-	1.73	-
2.5	-	2.60	-
1.0	-	2.90	-
4.0	-	2.90	-
13.0	13.0-19.0	3.55	3.40-3.65
30.0	30.0-40.0	4.30	4.15-4.45
30.0	30.0-45.0	4.50	4.30-4.70
90.0	70.0-90.0	4.40	4.20-4.60
100.0	80.0-100.0	4.50	4.25-4.75
77.0	***	4.75	-
14.5 37.5 D4			
0.5	-	1.73	-
2.5	-	1.73	-
2.0	-	2.60	-
1.0	-	2.90	-
4.0	-	2.90	-
17.0	14.5-19.5	3.70	3.60-3.80
30.0	30.0-40.0	4.50	4.40-4.60
30.0	30.0-45.0	4.40	4.20-4.60
100.0	80.0-100.0	4.45	4.25-4.65
100.0	80.0-100.0	4.50	4.25-4.75

h	Δh	Vs	ΔVs
63.0	***	4.75	-
15.5 37.5 D5			
1.5	-	0.00	-
1.0	-	2.22	-
1.4	-	2.22	-
1.3	-	2.31	-
1.8	-	3.15	-
14.0	13.0-15.0	3.10	3.05-3.15
45.0	35.0-45.0	4.30	4.25-4.35
30.0	30.0-40.0	4.80	4.65-4.80
105.0	85.0-105.0	4.40	4.20-4.60
65.0	65.0-85.0	4.50	4.30-4.70
84.0	***	4.75	-
16.5 37.5 D6			
2.7	-	0.00	-
0.3	-	2.25	-
1.1	-	2.25	-
1.1	-	2.31	-
2.8	-	3.32	-
13.0	11.0-15.0	3.10	2.95-3.20
40.0	30.0-50.0	4.20	4.10-4.30
30.0	30.0-45.0	4.80	4.65-4.80
100.0	80.0-100.0	4.40	4.20-4.60
60.0	60.0-80.0	4.45	4.20-4.65
99.0	***	4.75	-
17.5 37.5 D7			
3.1	-	0.00	-
0.9	-	2.08	-
0.2	-	2.22	-
1.1	-	2.31	-
2.7	-	3.31	-
17.0	16.5-17.5	3.25	3.20-3.30
60.0	45.0-60.0	4.50	4.45-4.55
60.0	45.0-60.0	4.75	4.60-4.75
60.0	60.0-80.0	4.30	4.15-4.45
60.0	60.0-80.0	4.75	4.50-4.75
85.0	***	4.75	-
18.5 37.5 D8			
2.9	-	0.00	-
1.1	-	2.25	-
0.1	-	2.25	-
1.1	-	2.31	-
2.8	-	3.31	-
17.0	15.5-18.5	3.20	3.10-3.30
30.0	30.0-40.0	4.60	4.45-4.75
30.0	30.0-42.5	4.60	4.50-4.70
60.0	60.0-80.0	4.75	4.55-4.75
70.0	70.0-90.0	4.40	4.15-4.65
135.0	***	4.75	-
19.5 37.5 D9			
2.9	-	0.00	-
1.1	-	2.25	-
0.1	-	2.25	-
1.1	-	2.31	-
2.8	-	3.31	-
5.0	5.0-7.0	3.05	2.85-3.25
16.0	13.0-19.0	3.30	3.10-3.45
30.0	30.0-40.0	4.60	4.45-4.75
100.0	80.0-100.0	4.60	4.50-4.70
110.0	85.0-110.0	4.50	4.25-4.75
81.0	***	4.75	-
11.5 38.5 C1			
1.5	-	0.00	-
0.9	-	1.10	-
0.4	-	2.31	-
3.2	-	2.90	-
1.0	-	2.90	-
12.0	9.0-15.0	3.60	3.45-3.75
32.0	24.0-40.0	4.15	4.05-4.25
60.0	45.0-60.0	4.45	4.40-4.50

h	Δh	Vs	ΔVs
60.0	60.0-80.0	4.30	4.15-4.45
110.0	85.0-110.0	4.45	4.20-4.65
69.0	***	4.75	-
12.5 38.5 C2			
1.0	-	0.00	-
1.5	-	1.11	-
0.4	-	2.20	-
2.6	-	2.63	-
0.5	-	2.63	-
20.0	17.5-22.5	3.75	3.70-3.80
30.0	25.0-35.0	4.25	4.20-4.30
60.0	45.0-60.0	4.40	4.35-4.45
100.0	80.0-100.0	4.40	4.30-4.50
60.0	60.0-80.0	4.30	4.15-4.45
74.0	***	4.75	-
13.5 38.5 C3			
2.0	-	0.00	-
0.4	-	1.10	-
0.4	-	2.31	-
2.2	-	2.90	-
1.0	-	2.90	-
13.0	11.5-14.5	3.30	3.25-3.35
24.0	18.0-30.0	4.10	4.05-4.15
60.0	45.0-75.0	4.40	4.30-4.50
55.0	55.0-72.5	4.40	4.30-4.50
110.0	90.0-110.0	4.50	4.35-4.65
82.0	***	4.75	-
14.5 38.5 C4			
2.4	-	0.00	-
0.0	-	1.00	-
0.4	-	2.31	-
2.2	-	3.55	-
1.0	-	3.55	-
13.0	11.0-15.0	3.05	2.95-3.10
12.0	12.0-18.0	3.85	3.65-4.05

h	Δh	Vs	ΔVs
30.0	30.0-45.0	4.05	3.95-4.20
60.0	60.0-80.0	4.55	4.45-4.70
120.0	100.0-120.0	4.40	4.20-4.60
109.0	***	4.75	-
15.5 38.5 C5			
1.0	-	0.00	-
0.5	-	2.60	-
0.5	-	2.60	-
0.5	-	2.60	-
0.5	-	2.60	-
14.0	12.5-15.5	2.90	2.85-3.00
27.0	22.5-31.5	3.90	3.80-4.00
60.0	45.0-60.0	4.60	4.45-4.75
110.0	90.0-110.0	4.50	4.40-4.60
70.0	70.0-90.0	4.70	4.50-4.80
66.0	***	4.75	-
16.5 38.5 C6			
2.0	-	2.45	-
1.0	-	2.45	-
0.8	-	2.45	-
1.2	-	2.74	-
8.0	-	2.74	-
14.0	11.0-14.0	3.45	3.40-3.55
24.0	21.0-27.0	4.15	4.05-4.25
30.0	30.0-40.0	4.50	4.35-4.65
70.0	70.0-90.0	4.65	4.50-4.80
70.0	70.0-90.0	4.40	4.20-4.60
129.0	***	4.75	-
17.5 38.5 C7			
2.4	-	0.00	-
2.1	-	2.10	-
0.7	-	2.25	-
0.8	-	3.25	-
1.0	-	3.25	-
18.0	15.5-20.5	3.20	3.10-3.30

h	Δh	Vs	ΔVs
28.0	23.0-33.0	4.25	4.10-4.40
30.0	30.0-45.0	4.80	4.65-4.80
60.0	60.0-80.0	4.40	4.20-4.60
100.0	80.0-100.0	4.50	4.25-4.75
107.0	***	4.75	-
18.5 38.5 C8			
2.9	-	0.00	-
1.2	-	2.25	-
1.1	-	2.35	-
0.8	-	3.32	-
2.0	-	3.32	-
15.0	12.5-17.5	3.05	2.95-3.15
30.0	30.0-40.0	4.25	4.10-4.40
30.0	30.0-42.5	4.90	4.70-4.90
95.0	77.5-95.0	4.45	4.20-4.70
70.0	70.0-95.0	4.50	4.20-4.80
102.0	***	4.75	-
19.5 38.5 C9			
2.8	-	0.00	-
0.3	-	2.02	-
0.1	-	2.02	-
0.3	-	2.02	-
0.5	-	2.02	-
12.0	9.0-15.0	3.35	3.20-3.45
10.0	10.0-14.5	3.00	2.80-3.20
30.0	30.0-45.0	4.35	4.25-4.45
110.0	90.0-110.0	4.60	4.50-4.70
120.0	100.0-120.0	4.45	4.30-4.60
64.0	***	4.75	-
10.5 39.5 B0			
2.3	-	0.00	-
0.7	-	1.16	-
2.0	-	3.01	-
2.0	-	3.12	-
1.0	-	3.24	-

h	Δh	Vs	ΔVs
12.0	10.0-14.0	3.70	3.60-3.80
60.0	47.5-60.0	4.30	4.25-4.35
80.0	65.0-80.0	4.30	4.10-4.50
80.0	65.0-80.0	4.40	4.10-4.70
60.0	60.0-80.0	4.40	4.00-4.80
50.0	***	4.75	-
11.5 39.5 B1			
3.0	-	0.00	-
0.7	-	1.20	-
1.0	-	3.45	-
1.3	-	3.95	-
1.0	-	3.95	-
8.0	6.0-10.0	3.80	3.55-4.05
13.0	11.0-15.0	3.70	3.55-3.90
90.0	75.0-90.0	4.25	4.20-4.30
60.0	60.0-80.0	4.30	4.15-4.45
100.0	80.0-100.0	4.40	4.20-4.60
72.0	***	4.75	-
12.5 39.5 B2			
3.0	-	0.00	-
0.7	-	1.20	-
1.0	-	3.45	-
1.3	-	3.95	-
1.0	-	3.95	-
9.0	7.5-10.5	3.70	3.55-3.90
11.0	9.5-12.5	3.45	3.30-3.60
70.0	55.0-70.0	4.20	4.10-4.30
70.0	70.0-90.0	4.30	4.25-4.40
110.0	85.0-110.0	4.40	4.20-4.60
73.0	***	4.75	-
13.5 39.5 B3			
3.0	-	0.00	-
0.7	-	1.20	-
1.0	-	3.45	-
1.3	-	3.95	-

h	Δh	Vs	ΔVs
1.0	-	3.95	-
11.0	9.0-13.0	3.80	3.60-4.00
8.0	6.5-9.5	3.10	2.90-3.30
60.0	50.0-60.0	4.20	4.10-4.30
70.0	70.0-90.0	4.30	4.20-4.40
120.0	100.0-120.0	4.40	4.20-4.60
74.0	***	4.75	-
14.5 39.5 B4			
2.5	-	0.00	-
0.5	-	1.30	-
2.0	-	3.45	-
0.5	-	3.95	-
0.5	-	3.95	-
17.0	15.0-19.0	3.30	3.20-3.40
60.0	45.0-60.0	4.20	4.10-4.30
60.0	45.0-60.0	4.35	4.20-4.50
90.0	70.0-90.0	4.40	4.20-4.60
70.0	70.0-90.0	4.40	4.20-4.60
47.0	***	4.75	-
15.5 39.5 B5			
0.9	-	0.00	-
2.1	-	1.15	-
1.0	-	2.90	-
1.0	-	2.90	-
1.0	-	2.90	-
18.0	14.0-22.0	3.50	3.45-3.55
8.0	8.0-10.5	3.90	3.70-4.10
40.0	30.0-50.0	4.15	4.10-4.20
70.0	70.0-90.0	4.60	4.50-4.70
110.0	90.0-110.0	4.40	4.20-4.60
98.0	***	4.75	-
16.5 39.5 B6			
3.0	-	2.45	-
1.0	-	2.45	-
1.0	-	2.80	-

h	Δh	Vs	ΔVs
1.0	-	2.80	-
7.0	-	2.80	-
8.0	8.0-11.0	3.40	3.35-3.50
15.0	15.0-20.0	3.70	3.50-3.90
30.0	30.0-45.0	4.40	4.20-4.60
60.0	60.0-85.0	4.60	4.40-4.80
110.0	85.0-110.0	4.50	4.25-4.75
114.0	***	4.75	-
17.5 39.5 B7			
1.5	-	0.00	-
1.5	-	2.90	-
0.5	-	3.52	-
0.5	-	3.52	-
1.0	-	3.52	-
8.0	7.0-9.0	2.60	2.55-2.65
20.0	17.0-23.0	3.50	3.35-3.65
30.0	30.0-45.0	4.50	4.35-4.65
110.0	90.0-110.0	4.55	4.40-4.70
60.0	60.0-85.0	4.40	4.20-4.60
117.0	***	4.75	-
18.5 39.5 B8			
1.0	-	0.00	-
2.0	-	2.25	-
0.5	-	2.25	-
0.6	-	2.25	-
3.9	-	3.05	-
19.0	17.5-19.0	3.25	3.20-3.30
50.0	40.0-50.0	4.60	4.45-4.75
35.0	35.0-47.5	4.45	4.30-4.55
50.0	50.0-70.0	4.50	4.30-4.70
120.0	90.0-120.0	4.55	4.30-4.80
68.0	***	4.75	-
19.5 39.5 B9			
1.7	-	0.00	-
1.3	-	2.30	-

h	Δh	Vs	ΔVs
0.5	-	2.30	-
1.5	-	2.30	-
2.0	-	3.00	-
20.0	18.0-22.0	3.30	3.25-3.35
60.0	50.0-60.0	4.50	4.45-4.55
40.0	30.0-50.0	4.35	4.15-4.55
70.0	60.0-80.0	4.70	4.60-4.80
100.0	80.0-100.0	4.20	4.10-4.30
53.0	***	4.75	-
8.5 39.5 B-2			
1.0	-	1.85	-
1.0	-	1.85	-
1.0	-	2.66	-
0.8	-	2.89	-
1.2	-	3.35	-
10.0	10.0-11.0	3.35	3.25-3.45
20.0	17.5-22.5	4.80	4.75-4.80
30.0	30.0-45.0	4.20	4.10-4.30
95.0	77.5-95.0	4.20	4.05-4.35
110.0	90.0-110.0	4.20	4.05-4.35
80.0	***	4.75	-
9.5 39.5 B-1			
1.0	-	1.85	-
0.5	-	1.85	-
1.5	-	2.78	-
0.5	-	2.89	-
1.5	-	3.35	-
6.0	4.5-7.5	3.20	3.00-3.40
8.0	8.0-10.5	4.10	3.95-4.10
35.0	35.0-52.5	4.40	4.30-4.50
75.0	57.5-75.0	4.20	4.10-4.30
160.0	130.0-160.0	4.35	4.25-4.45
61.0	***	4.75	-
10.5 40.5 A0			
1.8	-	0.00	-

h	Δh	Vs	ΔVs
1.2	-	1.16	-
2.0	-	3.01	-
2.0	-	3.12	-
1.0	-	3.24	-
12.0	8.0-16.0	3.85	3.75-3.95
50.0	40.0-50.0	4.30	4.20-4.45
80.0	65.0-80.0	4.20	4.05-4.30
85.0	67.5-85.0	4.40	4.10-4.70
65.0	65.0-85.0	4.40	4.10-4.70
50.0	***	4.75	-
11.5 40.5 A1			
2.5	-	0.00	-
0.7	-	1.38	-
1.0	-	3.45	-
0.8	-	3.52	-
1.0	-	3.52	-
16.0	14.0-18.0	3.60	3.55-3.65
49.0	37.0-49.0	4.30	4.20-4.40
30.0	30.0-45.0	4.00	4.00-4.10
100.0	80.0-100.0	4.40	4.20-4.60
110.0	90.0-110.0	4.45	4.20-4.65
39.0	***	4.75	-
12.5 40.5 A2			
2.5	-	0.00	-
0.7	-	1.20	-
1.0	-	3.45	-
0.8	-	3.95	-
1.0	-	3.95	-
20.0	15.0-25.0	3.65	3.60-3.70
12.0	12.0-17.0	4.40	4.20-4.60
60.0	45.0-60.0	4.15	4.10-4.20
100.0	80.0-100.0	4.35	4.20-4.50
100.0	80.0-100.0	4.40	4.20-4.60
52.0	***	4.75	-
13.5 40.5 A3			

h	Δh	Vs	ΔVs
1.5	-	0.00	-
2.2	-	1.20	-
1.0	-	3.45	-
0.3	-	3.95	-
1.0	-	3.95	-
5.0	5.0-6.0	4.40	4.20-4.60
10.0	10.0-15.0	3.50	3.40-3.60
40.0	40.0-55.0	4.00	3.85-4.15
100.0	85.0-100.0	4.35	4.30-4.40
120.0	100.0-120.0	4.40	4.20-4.60
69.0	***	4.75	-
14.5 40.5 A4			
0.5	-	0.00	-
1.0	-	2.60	-
1.5	-	3.00	-
2.0	-	3.35	-
1.0	-	3.35	-
4.0	4.0-5.5	2.55	2.40-2.70
13.0	13.0-18.0	3.50	3.30-3.70
50.0	40.0-50.0	4.20	4.10-4.25
110.0	90.0-110.0	4.40	4.25-4.55
120.0	95.0-120.0	4.40	4.20-4.60
47.0	***	4.75	-
15.5 40.5 A5			
1.1	-	1.50	-
2.4	-	2.10	-
1.5	-	2.90	-
2.0	-	3.49	-
2.0	-	3.49	-
12.0	10.0-14.0	3.25	3.15-3.35
50.0	40.0-50.0	4.25	4.15-4.35
30.0	30.0-40.0	4.80	4.60-4.80
60.0	60.0-85.0	4.30	4.15-4.45
110.0	85.0-110.0	4.45	4.20-4.65
79.0	***	4.75	-

h	Δh	Vs	ΔVs
16.5 40.5 A6			
1.1	-	1.50	-
2.4	-	2.10	-
1.5	-	2.90	-
2.0	-	3.49	-
2.0	-	3.49	-
10.0	7.5-12.5	3.10	2.90-3.30
17.0	-	4.15	4.05-4.15
13.0	8.0-18.0	4.15	4.05-4.25
30.0	30.0-45.0	4.80	4.65-4.80
60.0	60.0-85.0	4.35	4.15-4.55
110.0	90.0-110.0	4.50	4.30-4.70
101.0	***	4.75	-
17.5 40.5 A7			
1.0	-	2.25	-
2.0	-	2.25	-
1.6	-	2.25	-
2.4	-	3.06	-
1.0	-	3.06	-
12.0	11.0-13.0	3.05	3.00-3.10
20.0	15.0-25.0	4.10	4.00-4.10
50.0	50.0-65.0	4.60	4.55-4.65
100.0	80.0-100.0	4.45	4.40-4.50
60.0	60.0-80.0	4.40	4.20-4.60
100.0	***	4.75	-
18.5 40.5 A8			
0.3	-	0.00	-
2.4	-	2.25	-
1.9	-	2.60	-
1.3	-	3.03	-
1.0	-	3.03	-
20.0	19.0-21.0	3.30	3.25-3.35
40.0	30.0-50.0	4.60	4.55-4.65
30.0	30.0-40.0	4.30	4.15-4.45
105.0	90.0-105.0	4.50	4.35-4.65

h	Δh	Vs	ΔVs
65.0	65.0-85.0	4.40	4.20-4.60
83.0	***	4.75	-
19.5 40.5 A9			
0.8	-	1.85	-
2.2	-	1.95	-
2.0	-	1.95	-
2.0	-	3.50	-
1.0	-	3.50	-
5.0	5.0-7.0	3.90	3.70-4.10
19.0	15.5-22.5	3.50	3.35-3.65
60.0	50.0-60.0	4.55	4.45-4.65
120.0	100.0-120.0	4.45	4.40-4.50
70.0	70.0-90.0	4.40	4.25-4.55
68.0	***	4.75	-
20.5 40.5 A10			
1.5	-	2.50	-
1.5	-	2.50	-
1.0	-	3.30	-
1.0	-	3.30	-
1.0	-	3.30	-
18.0	15.0-18.0	3.40	3.35-3.50
14.0	14.0-19.0	3.50	3.35-3.65
50.0	50.0-67.5	4.65	4.55-4.80
60.0	60.0-77.5	4.55	4.45-4.70
75.0	75.0-95.0	4.40	4.20-4.60
127.0	***	4.75	-
8.5 40.5 A-2			
1.0	-	1.85	-
1.0	-	1.85	-
1.0	-	2.66	-
0.8	-	2.89	-
1.2	-	3.35	-
11.0	11.0-12.0	3.35	3.25-3.40
8.0	8.0-11.5	4.80	4.75-4.80
45.0	27.5-62.5	4.30	4.25-4.35

h	Δh	Vs	ΔVs
90.0	72.5-90.0	4.20	4.15-4.25
110.0	90.0-110.0	4.40	4.30-4.50
81.0	***	4.75	-
9.5 40.5 A-1			
1.0	-	1.85	-
0.5	-	1.85	-
1.5	-	2.78	-
0.5	-	2.89	-
1.5	-	3.35	-
4.0	4.0-5.5	3.10	2.90-3.25
10.0	10.0-12.5	3.85	3.70-3.95
40.0	40.0-55.0	4.45	4.40-4.50
80.0	62.5-80.0	4.20	4.10-4.30
160.0	125.0-160.0	4.35	4.15-4.55
51.0	***	4.75	-
10.5 41.5 a0			
1.2	-	0.00	-
1.8	-	1.20	-
0.7	-	1.35	-
1.2	-	3.75	-
1.1	-	3.90	-
25.0	22.5-27.5	3.90	3.90-3.95
10.0	7.5-12.5	4.65	4.55-4.75
25.0	20.0-30.0	4.10	4.00-4.20
80.0	70.0-80.0	4.20	4.15-4.25
130.0	120.0-140.0	4.30	4.25-4.35
74.0	***	4.75	-
11.5 41.5 a1			
1.0	-	0.00	-
2.5	-	1.33	-
1.1	-	2.90	-
0.4	-	3.30	-
1.0	-	3.30	-
4.0	3.5-4.5	4.75	4.70-4.80
13.0	11.5-14.5	3.75	3.65-3.85

h	Δh	Vs	ΔVs
60.0	52.5-60.0	4.20	4.15-4.25
50.0	40.0-60.0	4.15	4.10-4.20
140.0	125.0-155.0	4.30	4.25-4.35
77.0	***	4.75	-
12.5 41.5 a2			
0.4	-	0.00	-
2.1	-	1.32	-
1.0	-	3.06	-
1.5	-	3.30	-
1.0	-	3.30	-
19.0	-	3.90	3.90-3.95
10.0	9.0-11.0	3.90	3.90-3.95
12.0	12.0-15.0	4.70	4.60-4.80
40.0	30.0-50.0	4.10	4.05-4.15
70.0	70.0-90.0	4.25	4.20-4.30
110.0	90.0-110.0	4.30	4.15-4.45
83.0	***	4.75	-
13.5 41.5 a3			
2.5	-	1.87	-
1.5	-	2.19	-
0.5	-	3.26	-
0.3	-	3.26	-
0.2	-	3.26	-
6.0	6.0-9.0	3.65	3.55-3.80
10.0	10.0-13.0	3.45	3.35-3.60
30.0	30.0-45.0	4.20	4.10-4.30
110.0	85.0-110.0	4.35	4.20-4.50
120.0	95.0-120.0	4.40	4.20-4.60
69.0	***	4.75	-
14.5 41.5 a4			
2.5	-	2.25	-
2.0	-	2.45	-
0.5	-	2.55	-
0.5	-	3.06	-
0.5	-	3.06	-

h	Δh	Vs	ΔVs
6.0	5.0-7.0	3.45	3.25-3.65
5.0	5.0-7.5	3.25	3.05-3.45
24.0	18.5-29.5	3.90	3.80-4.00
110.0	90.0-110.0	4.45	4.40-4.50
120.0	100.0-120.0	4.40	4.20-4.60
79.0	***	4.75	-
15.5 41.5 a5			
1.0	-	2.00	-
2.0	-	2.00	-
2.0	-	2.28	-
3.0	-	3.00	-
2.0	-	3.25	-
8.0	8.0-12.0	3.50	3.40-3.60
25.0	25.0-35.0	4.00	3.85-4.10
30.0	30.0-45.0	4.70	4.55-4.80
100.0	80.0-100.0	4.40	4.20-4.60
100.0	75.0-100.0	4.50	4.25-4.75
77.0	***	4.75	-
16.5 41.5 a6			
0.1	-	0.00	-
2.9	-	2.22	-
1.6	-	2.22	-
0.8	-	3.20	-
0.7	-	3.20	-
4.0	4.0-5.0	3.25	3.20-3.30
10.0	8.5-11.5	3.15	3.05-3.25
26.0	20.0-32.0	4.20	4.05-4.35
70.0	70.0-90.0	4.45	4.40-4.50
120.0	95.0-120.0	4.40	4.30-4.50
114.0	***	4.75	-
17.5 41.5 a7			
1.3	-	0.00	-
1.7	-	2.08	-
2.0	-	2.08	-
3.0	-	3.06	-

h	Δh	Vs	ΔVs
1.0	-	3.06	-
15.0	12.5-17.5	3.30	3.20-3.40
15.0	15.0-22.5	4.35	4.20-4.45
60.0	45.0-60.0	4.50	4.40-4.60
60.0	60.0-80.0	4.40	4.30-4.55
70.0	70.0-90.0	4.35	4.15-4.55
121.0	***	4.75	-
18.5 41.5 a8			
1.1	-	0.00	-
1.9	-	2.08	-
2.0	-	2.08	-
1.0	-	3.03	-
1.0	-	3.03	-
19.0	16.0-22.0	3.30	3.20-3.40
30.0	30.0-40.0	4.40	4.20-4.60
60.0	45.0-60.0	4.50	4.35-4.65
60.0	60.0-80.0	4.40	4.25-4.55
60.0	60.0-80.0	4.50	4.25-4.75
114.0	***	4.75	-
19.5 41.5 a9			
1.0	-	1.85	-
2.0	-	1.85	-
1.0	-	1.85	-
1.0	-	3.50	-
2.0	-	3.56	-
22.0	22.0-26.0	3.45	3.40-3.50
30.0	30.0-40.0	4.45	4.25-4.60
30.0	30.0-40.0	4.40	4.20-4.60
60.0	60.0-80.0	4.50	4.25-4.75
105.0	82.5-105.0	4.50	4.15-4.80
96.0	***	4.75	-
20.5 41.5 a10			
1.2	-	1.97	-
0.8	-	2.54	-
1.0	-	2.54	-
1.0	-	3.49	-
1.0	-	3.49	-
19.0	15.5-19.0	3.45	3.35-3.55
18.0	15.0-18.0	3.65	3.50-3.80
80.0	65.0-80.0	4.55	4.45-4.70
95.0	75.0-95.0	4.50	4.35-4.65
75.0	75.0-97.5	4.75	4.55-4.80
58.0	***	4.75	-
21.5 41.5 a11			
1.2	-	2.19	-
2.0	-	2.66	-
0.8	-	3.58	-
1.0	-	3.58	-
1.0	-	3.58	-
12.0	12.0-14.0	3.45	3.40-3.55
20.0	18.0-20.0	3.60	3.50-3.70
50.0	50.0-70.0	4.40	4.35-4.45
95.0	75.0-95.0	4.50	4.35-4.65
65.0	65.0-87.5	4.35	4.15-4.55
102.0	***	4.75	-

Table 4b. Part II

h	Δh	Vs	ΔVs
8.5 41.5 a-2			
1.0	-	0.00	-
1.5	-	1.20	-
1.5	-	2.10	-
1.0	-	2.20	-
1.0	-	2.50	-
12.0	10.0-14.0	3.90	3.85-3.95
45.0	37.5-45.0	4.35	4.30-4.40
50.0	40.0-60.0	4.15	4.10-4.20
45.0	45.0-62.5	4.40	4.30-4.55
105.0	85.0-105.0	4.30	4.15-4.45
87.0	***	4.75	-
9.5 41.5 a-1			

h	Δh	Vs	ΔVs
0.1	-	0.00	-
0.8	-	1.10	-
0.5	-	1.20	-
1.5	-	2.80	-
2.0	-	3.00	-
11.0	9.5-12.5	3.55	3.50-3.60
12.0	12.0-18.0	4.20	4.15-4.25
70.0	57.5-82.5	4.25	4.20-4.30
70.0	52.5-70.0	4.20	4.05-4.35
105.0	85.0-105.0	4.40	4.25-4.55
77.0	***	4.75	-
10.5 42.5 b0			
0.5	-	0.00	-
0.5	-	3.00	-
2.0	-	2.65	-
2.0	-	2.65	-
2.0	-	2.65	-
6.0	6.0-8.5	3.15	3.10-3.25
17.0	14.5-17.0	3.90	3.75-4.05
30.0	30.0-45.0	4.30	4.25-4.35
110.0	90.0-110.0	4.30	4.25-4.35
120.0	90.0-120.0	4.40	4.20-4.60
60.0	***	4.75	-
11.5 42.5 b1			
0.2	-	3.00	-
0.8	-	3.50	-
2.0	-	2.65	-
2.0	-	2.65	-
2.0	-	2.65	-
16.0	14.0-18.0	3.45	3.35-3.55
18.0	18.0-26.0	4.20	4.10-4.25
30.0	30.0-45.0	4.35	4.25-4.45
110.0	85.0-110.0	4.30	4.25-4.40
100.0	75.0-100.0	4.45	4.20-4.65
69.0	***	4.75	-

h	Δh	Vs	ΔVs
12.5 42.5 b2			
1.2	-	1.60	-
0.8	-	2.30	-
1.0	-	3.00	-
0.5	-	3.00	-
0.5	-	3.30	-
10.0	7.5-12.5	3.35	3.25-3.40
19.0	16.5-21.5	3.75	3.60-3.90
55.0	42.5-55.0	4.35	4.30-4.40
70.0	70.0-90.0	4.30	4.20-4.40
120.0	95.0-120.0	4.40	4.20-4.60
72.0	***	4.75	-
13.5 42.5 b3			
1.2	-	1.55	-
0.8	-	2.13	-
0.5	-	3.10	-
0.5	-	3.10	-
0.5	-	3.10	-
12.0	10.5-13.5	3.30	3.25-3.30
20.0	15.0-25.0	3.70	3.55-3.85
60.0	45.0-60.0	4.55	4.40-4.70
60.0	60.0-85.0	4.20	4.05-4.35
110.0	85.0-110.0	4.40	4.20-4.60
84.5	***	4.75	-
14.5 42.5 b4			
0.2	-	0.00	-
2.8	-	2.08	-
1.0	-	2.08	-
2.0	-	3.20	-
1.0	-	3.20	-
10.0	8.5-11.5	3.15	3.05-3.25
24.0	19.0-29.0	3.90	3.75-4.05
60.0	45.0-60.0	4.60	4.40-4.80
110.0	90.0-110.0	4.30	4.15-4.45
70.0	70.0-95.0	4.50	4.25-4.75

h	Δh	Vs	ΔVs
69.0	***	4.75	-
15.5 42.5 b5			
0.1	-	0.00	-
2.9	-	1.91	-
1.0	-	1.91	-
1.5	-	3.55	-
0.5	-	3.55	-
2.0	2.0-2.5	3.85	3.65-4.05
7.0	7.0-8.5	2.95	2.80-3.10
21.0	17.0-25.0	3.90	3.80-4.00
130.0	105.0-130.0	4.45	4.40-4.50
70.0	70.0-100.0	4.40	4.20-4.60
114.0	***	4.75	-
16.5 42.5 b6			
0.2	-	0.00	-
2.8	-	1.92	-
0.9	-	1.92	-
1.6	-	3.55	-
2.5	-	3.50	-
8.0	8.0-10.0	3.20	3.15-3.25
9.0	9.0-13.0	3.60	3.40-3.75
14.0	14.0-19.0	4.20	4.00-4.40
70.0	70.0-90.0	4.40	4.35-4.45
120.0	95.0-120.0	4.40	4.25-4.55
121.0	***	4.75	-
17.5 42.5 b7			
0.5	-	0.00	-
2.5	-	1.91	-
0.8	-	1.91	-
1.7	-	3.55	-
2.5	-	3.55	-
14.0	12.5-15.5	3.20	3.15-3.25
10.0	10.0-14.5	3.95	3.75-4.10
30.0	30.0-45.0	4.40	4.30-4.55
50.0	50.0-70.0	4.35	4.15-4.55
120.0	90.0-120.0	4.50	4.25-4.75
118.0	***	4.75	-
18.5 42.5 b8			
0.2	-	0.00	-
2.8	-	1.91	-
0.5	-	1.91	-
2.0	-	3.55	-
1.5	-	3.55	-
20.0	17.5-22.5	3.35	3.30-3.40
30.0	25.0-35.0	4.30	4.20-4.40
60.0	45.0-60.0	4.50	4.35-4.65
60.0	60.0-80.0	4.35	4.20-4.50
60.0	60.0-82.5	4.50	4.25-4.75
113.0	***	4.75	-
19.5 42.5 b9			
1.5	-	2.50	-
1.5	-	2.50	-
1.0	-	3.35	-
1.0	-	3.50	-
1.0	-	3.50	-
15.0	11.5-18.5	3.15	3.10-3.25
12.0	12.0-17.0	3.60	3.45-3.70
35.0	35.0-45.0	4.40	4.30-4.50
70.0	70.0-90.0	4.50	4.35-4.65
115.0	92.5-115.0	4.35	4.15-4.55
97.0	***	4.75	-
20.5 42.5 b10			
2.0	-	2.75	-
0.5	-	2.75	-
0.5	-	3.35	-
1.0	-	3.50	-
1.0	-	3.50	-
12.0	12.0-17.5	3.20	3.15-3.25
25.0	19.5-25.0	3.70	3.50-3.90
80.0	65.0-80.0	4.60	4.45-4.70

h	Δh	Vs	ΔVs
55.0	55.0-72.5	4.40	4.20-4.60
70.0	70.0-90.0	4.40	4.20-4.60
103.0	***	4.75	-
21.5 42.5 b11			
1.0	-	3.00	-
1.0	-	3.00	-
1.0	-	3.20	-
1.0	-	3.20	-
1.0	-	3.20	-
14.0	10.0-18.0	3.35	3.25-3.40
16.0	16.0-21.0	3.70	3.50-3.90
50.0	50.0-67.5	4.35	4.20-4.45
100.0	80.0-100.0	4.45	4.25-4.60
70.0	70.0-90.0	4.40	4.15-4.65
95.0	***	4.75	-
8.5 42.5 b-2			
1.5	-	0.00	-
0.5	-	1.20	-
1.0	-	2.15	-
1.5	-	2.25	-
1.5	-	2.60	-
8.0	6.5-9.5	3.35	3.25-3.45
15.0	15.0-22.5	4.35	4.25-4.45
65.0	52.5-65.0	4.40	4.20-4.60
75.0	57.5-75.0	4.15	4.00-4.35
100.0	77.5-122.5	4.50	4.25-4.75
81.0	***	4.75	-
9.5 42.5 b-1			
0.1	-	0.00	-
1.4	-	1.20	-
0.5	-	1.35	-
1.0	-	2.80	-
1.0	-	3.00	-
14.0	12.0-16.0	3.60	3.50-3.65
30.0	26.0-34.0	4.20	4.10-4.30

h	Δh	Vs	ΔVs
25.0	25.0-32.5	4.30	4.25-4.40
70.0	55.0-85.0	4.20	4.10-4.30
120.0	95.0-120.0	4.30	4.15-4.45
87.0	***	4.75	-
10.5 43.5 c0			
3.0	-	2.20	-
1.0	-	2.20	-
1.0	-	2.65	-
0.5	-	3.00	-
0.5	-	3.00	-
8.0	8.0-11.5	3.20	3.10-3.30
14.0	14.0-20.5	3.80	3.65-3.95
60.0	47.5-60.0	4.40	4.35-4.45
100.0	80.0-100.0	4.40	4.25-4.55
110.0	85.0-110.0	4.45	4.20-4.65
52.0	***	4.75	-
11.5 43.5 c1			
3.0	-	2.20	-
1.0	-	2.20	-
1.0	-	2.65	-
1.0	-	3.20	-
1.0	-	3.20	-
14.0	11.0-17.0	3.35	3.25-3.45
18.0	18.0-23.0	4.10	3.95-4.25
35.0	35.0-50.0	4.55	4.45-4.65
105.0	85.0-105.0	4.40	4.25-4.55
100.0	75.0-100.0	4.40	4.20-4.60
71.0	***	4.75	-
12.5 43.5 c2			
0.5	-	1.60	-
1.0	-	2.30	-
1.0	-	3.00	-
0.5	-	3.50	-
1.0	-	3.50	-
6.0	5.0-7.0	2.70	2.60-2.80

h	Δh	Vs	ΔVs
24.0	22.0-26.0	3.60	3.50-3.65
35.0	35.0-50.0	4.60	4.50-4.70
100.0	80.0-100.0	4.40	4.25-4.55
110.0	85.0-110.0	4.40	4.20-4.60
71.0	***	4.75	-
13.5 43.5 c3			
1.1	-	1.55	-
1.9	-	2.08	-
0.5	-	2.08	-
1.5	-	3.18	-
1.0	-	3.50	-
15.0	12.5-17.5	3.25	3.15-3.35
20.0	16.5-23.5	3.95	3.80-4.10
60.0	45.0-60.0	4.50	4.35-4.65
110.0	90.0-110.0	4.35	4.20-4.45
70.0	70.0-90.0	4.45	4.20-4.65
69.0	***	4.75	-
14.5 43.5 c4			
0.1	-	0.00	-
2.9	-	1.76	-
1.0	-	2.25	-
1.0	-	3.45	-
1.0	-	3.45	-
15.0	12.5-17.5	3.35	3.30-3.40
28.0	21.0-35.0	3.85	3.65-4.05
30.0	30.0-45.0	4.80	4.60-4.80
100.0	75.0-100.0	4.30	4.15-4.45
50.0	50.0-75.0	4.40	4.20-4.60
121.0	***	4.75	-
15.5 43.5 c5			
0.2	-	0.00	-
2.8	-	1.96	-
1.0	-	2.28	-
1.0	-	3.45	-
1.0	-	3.45	-

h	Δh	Vs	ΔVs
14.0	11.0-17.0	3.30	3.20-3.40
15.0	15.0-19.0	3.95	3.80-4.10
40.0	40.0-55.0	4.40	4.25-4.55
100.0	75.0-100.0	4.40	4.20-4.60
60.0	60.0-85.0	4.40	4.20-4.60
115.0	***	4.75	-
16.5 43.5 c6			
2.0	-	2.10	-
2.0	-	2.10	-
1.5	-	3.30	-
1.5	-	3.60	-
1.0	-	3.60	-
18.0	15.0-21.0	3.45	3.40-3.55
10.0	10.0-15.0	4.20	4.05-4.20
30.0	30.0-45.0	4.35	4.20-4.45
100.0	75.0-100.0	4.40	4.25-4.55
60.0	60.0-85.0	4.40	4.20-4.60
124.0	***	4.75	-
17.5 43.5 c7			
2.0	-	2.20	-
2.0	-	2.25	-
1.5	-	3.40	-
1.0	-	3.60	-
1.5	-	3.60	-
11.0	9.0-13.0	3.20	3.10-3.30
17.0	17.0-25.5	3.75	3.55-3.95
60.0	45.0-60.0	4.50	4.30-4.70
55.0	55.0-75.0	4.30	4.20-4.45
110.0	85.0-110.0	4.50	4.25-4.75
89.0	***	4.75	-
18.5 43.5 c8			
2.0	-	2.20	-
2.0	-	2.20	-
1.0	-	3.25	-
0.5	-	3.45	-

h	Δh	Vs	ΔVs
0.5	-	3.45	-
3.0	3.0-4.0	3.95	3.90-4.05
9.0	7.5-10.5	3.00	2.90-3.10
24.0	18.5-29.5	3.85	3.75-3.95
60.0	60.0-90.0	4.40	4.30-4.50
120.0	90.0-120.0	4.40	4.20-4.60
128.0	***	4.75	-
19.5 43.5 c9			
1.5	-	2.55	-
1.0	-	2.55	-
1.5	-	3.25	-
1.0	-	3.45	-
1.0	-	3.45	-
16.0	12.0-16.0	3.30	3.20-3.40
3.0	3.0-7.5	3.30	3.10-3.50
25.0	25.0-40.0	4.00	4.00-4.10
100.0	82.5-100.0	4.40	4.20-4.60
110.0	90.0-110.0	4.40	4.20-4.60
90.0	***	4.75	-
20.5 43.5 c10			
1.5	-	2.65	-
1.0	-	2.65	-
1.5	-	3.40	-
1.0	-	3.50	-
1.0	-	3.50	-
12.0	12.0-15.0	3.20	3.10-3.30
20.0	15.0-25.0	3.80	3.65-3.90
45.0	45.0-60.0	4.30	4.20-4.45
100.0	80.0-100.0	4.50	4.30-4.70
65.0	65.0-87.5	4.40	4.10-4.70
102.0	***	4.75	-
21.5 43.5 c11			
2.0	-	2.80	-
2.0	-	2.80	-
1.0	-	3.05	-
1.0	-	3.05	-
12.0	8.0-16.0	3.40	3.35-3.50
16.0	12.0-20.0	3.75	3.60-3.90
40.0	40.0-57.5	4.30	4.10-4.50
60.0	60.0-77.5	4.45	4.25-4.65
110.0	87.5-110.0	4.40	4.15-4.65
105.0	***	4.75	-
8.5 43.5 c-2			
2.1	-	0.00	-
1.0	-	1.20	-
0.9	-	1.60	-
1.0	-	1.60	-
1.0	-	2.50	-
10.0	7.5-12.5	3.55	3.45-3.65
15.0	15.0-22.5	4.10	4.00-4.25
15.0	15.0-27.5	4.30	4.10-4.50
70.0	52.5-70.0	4.40	4.20-4.60
100.0	80.0-120.0	4.15	4.00-4.40
134.0	***	4.75	-
9.5 43.5 c-1			
0.7	-	0.00	-
1.3	-	1.10	-
0.5	-	1.60	-
2.5	-	3.40	-
1.0	-	3.50	-
4.0	3.0-5.0	2.80	2.65-2.90
19.0	14.0-24.0	3.75	3.65-3.85
70.0	55.0-70.0	4.40	4.30-4.50
75.0	57.5-75.0	4.20	4.00-4.40
105.0	85.0-125.0	4.45	4.25-4.60
71.0	***	4.75	-
10.5 44.5 d0			
3.0	-	2.00	-
1.4	-	2.20	-

h	Δh	Vs	ΔVs
1.6	-	2.80	-
0.5	-	3.25	-
0.5	-	3.25	-
11.0	10.5-11.5	3.30	3.25-3.35
20.0	20.0-30.0	3.95	3.85-4.05
30.0	30.0-45.0	4.45	4.25-4.60
100.0	75.0-100.0	4.45	4.20-4.65
50.0	50.0-75.0	4.00	4.00-4.20
132.0	***	4.75	-
11.5 44.5 d1			
2.0	-	2.00	-
1.0	-	2.15	-
1.4	-	2.15	-
1.6	-	2.80	-
1.0	-	3.25	-
9.0	9.0-13.0	3.25	3.15-3.35
20.0	15.0-25.0	3.80	3.60-3.95
50.0	40.0-50.0	4.50	4.35-4.65
60.0	60.0-80.0	4.70	4.50-4.80
60.0	60.0-80.0	4.00	4.00-4.20
144.0	***	4.75	-
12.5 44.5 d2			
0.4	-	0.00	-
3.6	-	2.00	-
1.0	-	3.30	-
1.0	-	3.30	-
2.0	-	3.50	-
6.0	6.0-9.0	3.15	3.10-3.25
20.0	20.0-26.0	3.55	3.35-3.75
60.0	45.0-60.0	4.50	4.35-4.65
55.0	55.0-80.0	4.45	4.20-4.65
60.0	60.0-85.0	4.00	4.00-4.20
141.0	***	4.75	-
13.5 44.5 d3			
0.1	-	0.00	-
3.0	-	1.76	-
1.0	-	2.25	-
1.0	-	3.45	-
1.0	-	3.50	-
19.0	15.5-22.5	3.45	3.40-3.50
12.0	10.0-14.0	4.10	3.95-4.10
15.0	15.0-22.5	4.15	4.05-4.30
80.0	65.0-95.0	4.60	4.50-4.70
70.0	70.0-90.0	4.00	4.00-4.10
148.0	***	4.75	-
14.5 44.5 d4			
0.1	-	0.00	-
3.0	-	1.76	-
1.0	-	2.25	-
1.0	-	3.40	-
1.0	-	3.40	-
5.0	4.0-6.0	3.60	3.55-3.65
15.0	14.0-16.0	3.50	3.45-3.55
34.0	33.0-35.0	4.15	4.10-4.20
70.0	65.0-75.0	4.75	4.70-4.80
65.0	57.5-72.5	4.00	4.00-4.05
155.0	***	4.75	-
15.5 44.5 d5			
3.0	-	2.10	-
1.0	-	2.10	-
1.5	-	3.30	-
1.5	-	3.60	-
1.0	-	3.60	-
21.0	17.0-25.0	3.50	3.45-3.55
30.0	25.0-35.0	4.30	4.05-4.55
30.0	30.0-40.0	4.60	4.55-4.60
100.0	80.0-100.0	4.40	4.25-4.55
60.0	60.0-90.0	4.40	4.20-4.60
101.0	***	4.75	-
16.5 44.5 d6			

h	Δh	Vs	ΔVs
3.0	-	2.20	-
1.0	-	2.30	-
1.5	-	3.30	-
1.0	-	3.45	-
0.5	-	3.45	-
4.0	4.0-6.0	3.95	3.85-4.05
20.0	16.0-24.0	3.50	3.40-3.60
70.0	55.0-70.0	4.40	4.30-4.50
60.0	60.0-85.0	4.30	4.20-4.40
110.0	85.0-110.0	4.45	4.20-4.65
79.0	***	4.75	-
17.5 44.5 d7			
3.0	-	2.20	-
1.0	-	2.30	-
1.0	-	3.30	-
0.5	-	3.50	-
0.5	-	3.50	-
7.0	7.0-8.5	3.65	3.55-3.80
16.0	13.0-19.0	3.50	3.40-3.60
70.0	55.0-70.0	4.40	4.30-4.50
110.0	85.0-110.0	4.40	4.25-4.55
60.0	60.0-90.0	4.50	4.25-4.75
81.0	***	4.75	-
18.5 44.5 d8			
3.0	-	2.30	-
1.0	-	2.30	-
1.5	-	3.25	-
0.5	-	3.45	-
1.0	-	3.45	-
22.0	16.5-27.5	3.55	3.45-3.60
15.0	15.0-22.5	4.20	4.00-4.45
40.0	40.0-57.0	4.40	4.25-4.55
90.0	70.0-90.0	4.40	4.20-4.60
100.0	75.0-100.0	4.50	4.25-4.75
76.0	***	4.75	-

h	Δh	Vs	ΔVs
6.5 44.5 d-4			
1.0	-	2.75	-
1.0	-	2.75	-
1.0	-	3.00	-
1.0	-	3.00	-
1.0	-	3.15	-
8.0	6.5-9.5	2.90	2.80-3.05
22.0	19.5-24.5	3.90	3.80-4.05
70.0	55.0-70.0	4.35	4.30-4.40
110.0	85.0-110.0	4.35	4.20-4.50
60.0	60.0-85.0	4.40	4.20-4.60
75.0	***	4.75	-
7.5 44.5 d-3			
1.0	-	2.75	-
1.0	-	2.85	-
1.0	-	3.00	-
1.0	-	3.10	-
1.0	-	3.10	-
6.0	6.0-8.0	2.65	2.55-2.80
20.0	20.0-30.0	3.80	3.65-3.95
85.0	67.5-85.0	4.40	4.30-4.50
100.0	80.0-100.0	4.35	4.15-4.55
60.0	60.0-80.0	4.50	4.25-4.75
74.0	***	4.75	-
8.5 44.5 d-2			
1.0	-	2.30	-
1.0	-	2.30	-
1.0	-	2.50	-
1.0	-	2.50	-
2.0	-	2.50	-
10.0	8.5-11.5	3.35	3.20-3.45
29.0	24.5-33.5	4.10	3.95-4.10
50.0	50.0-65.0	4.60	4.45-4.70
100.0	80.0-100.0	4.30	4.15-4.45
70.0	70.0-90.0	4.50	4.20-4.80

h	Δh	Vs	ΔVs
85.0	***	4.75	-
9.5 44.5 d-1			
1.0	-	2.30	-
1.0	-	2.30	-
1.0	-	2.50	-
1.0	-	2.50	-
2.0	-	2.50	-
5.0	5.0-7.5	2.95	2.75-3.15
20.0	16.0-24.0	3.75	3.60-3.90
85.0	70.0-85.0	4.45	4.40-4.50
70.0	52.5-87.5	4.25	4.05-4.45
110.0	90.0-110.0	4.50	4.25-4.75
54.0	***	4.75	-
10.5 45.5 e0			
1.0	-	2.00	-
1.0	-	2.56	-
1.0	-	2.56	-
2.0	-	3.01	-
1.0	-	3.01	-
5.0	5.0-6.0	2.95	2.85-3.05
27.0	24.0-30.0	3.75	3.65-3.85
50.0	50.0-70.0	4.65	4.55-4.75
50.0	50.0-70.0	4.50	4.25-4.75
70.0	70.0-90.0	4.00	4.00-4.40
142.0	***	4.75	-
11.5 45.5 e1			
3.0	-	2.55	-
1.5	-	2.55	-
1.5	-	3.18	-
0.5	-	3.30	-
0.5	-	3.30	-
4.0	4.0-5.5	2.80	2.65-2.90
21.0	17.5-24.5	3.55	3.40-3.65
80.0	60.0-80.0	4.50	4.40-4.60
110.0	90.0-110.0	4.40	4.25-4.55

h	Δh	Vs	ΔVs
60.0	60.0-82.5	4.50	4.25-4.75
68.0	***	4.75	-
12.5 45.5 e2			
1.0	-	2.10	-
2.0	-	2.50	-
2.0	-	2.50	-
1.0	-	2.90	-
1.0	-	2.90	-
14.0	10.5-17.5	3.35	3.30-3.40
20.0	20.0-30.0	3.90	3.75-4.10
60.0	45.0-60.0	4.65	4.55-4.80
90.0	70.0-90.0	4.40	4.25-4.55
100.0	75.0-100.0	4.45	4.20-4.65
59.0	***	4.75	-
13.5 45.5 e3			
1.0	-	2.10	-
4.0	-	2.60	-
1.0	-	3.00	-
1.0	-	3.20	-
1.0	-	3.20	-
12.0	12.0-15.0	3.30	3.25-3.35
25.0	22.5-27.5	3.95	3.80-4.10
60.0	45.0-75.0	4.65	4.60-4.70
90.0	70.0-90.0	4.35	4.30-4.40
90.0	70.0-90.0	4.50	4.30-4.70
65.0	***	4.75	-
14.5 45.5 e4			
4.0	-	2.30	-
1.0	-	3.25	-
0.5	-	3.25	-
1.5	-	3.35	-
1.0	-	3.45	-
15.0	15.0-20.0	3.50	3.45-3.55
17.0	-	4.00	3.80-4.00
13.0	5.5-20.5	4.00	4.00-4.20

h	Δh	Vs	ΔVs
30.0	30.0-40.0	4.80	4.70-4.80
100.0	80.0-100.0	4.40	4.20-4.60
60.0	60.0-85.0	4.50	4.30-4.70
107.0	***	4.75	-
15.5 45.5 e5			
4.0	-	2.10	-
1.0	-	3.30	-
0.5	-	3.30	-
1.5	-	3.60	-
1.0	-	3.60	-
24.0	20.0-28.0	3.75	3.65-3.85
25.0	25.0-37.5	4.30	4.10-4.50
60.0	45.0-60.0	4.55	4.40-4.75
90.0	70.0-90.0	4.30	4.15-4.45
50.0	50.0-75.0	4.50	4.25-4.75
93.0	***	4.75	-
16.5 45.5 e6			
1.5	-	2.40	-
1.0	-	2.60	-
0.5	-	3.00	-
0.5	-	3.20	-
0.5	-	3.20	-
12.0	10.0-14.0	3.30	3.25-3.35
21.0	17.5-24.5	3.80	3.65-3.90
50.0	50.0-67.5	4.50	4.35-4.65
85.0	67.5-85.0	4.35	4.10-4.55
65.0	65.0-87.5	4.40	4.10-4.70
113.0	***	4.75	-
17.5 45.5 e7			
1.0	-	1.50	-
0.6	-	3.05	-
1.9	-	3.14	-
0.5	-	3.20	-
1.0	-	3.20	-
5.0	5.0-7.5	3.15	3.05-3.25

h	Δh	Vs	ΔVs
15.0	10.0-20.0	3.60	3.45-3.70
50.0	50.0-67.5	4.30	4.20-4.45
60.0	60.0-80.0	4.50	4.35-4.65
70.0	70.0-92.5	4.00	4.00-4.20
145.0	***	4.75	-
6.5 45.5 e-4			
0.5	-	1.20	-
0.5	-	2.90	-
1.0	-	2.90	-
1.0	-	2.90	-
2.0	-	2.90	-
8.0	7.0-9.0	2.85	2.80-2.90
20.0	17.0-23.0	3.95	3.75-4.10
75.0	65.0-75.0	4.45	4.40-4.45
65.0	65.0-82.5	4.60	4.50-4.70
110.0	87.5-110.0	4.35	4.15-4.55
67.0	***	4.75	-
7.5 45.5 e-3			
0.1	-	1.20	-
0.9	-	2.80	-
1.0	-	2.80	-
2.0	-	2.80	-
2.0	-	2.80	-
7.0	7.0-8.0	2.85	2.75-2.95
26.0	22.5-29.5	4.00	3.90-4.00
85.0	70.0-85.0	4.55	4.50-4.60
100.0	72.5-100.0	4.30	4.05-4.55
55.0	55.0-82.5	4.50	4.25-4.75
71.0	***	4.75	-
8.5 45.5 e-2			
1.0	-	2.43	-
1.0	-	2.43	-
1.0	-	2.43	-
1.0	-	2.90	-
2.0	-	2.90	-

h	Δh	Vs	ΔVs
10.0	8.0-12.0	3.15	3.05-3.30
25.0	21.0-29.0	4.00	3.90-4.10
50.0	50.0-65.0	4.65	4.55-4.75
100.0	80.0-100.0	4.35	4.20-4.50
70.0	70.0-90.0	4.40	4.20-4.60
89.0	***	4.75	-
9.5 45.5 e-1			
1.0	-	2.30	-
1.0	-	2.30	-
1.0	-	2.30	-
1.0	-	2.60	-
2.0	-	2.60	-
10.0	10.0-12.5	3.15	3.05-3.30
25.0	21.0-25.0	4.00	3.90-4.00
50.0	50.0-65.0	4.70	4.55-4.85
100.0	82.5-100.0	4.35	4.20-4.50
70.0	70.0-90.0	4.40	4.20-4.60
89.0	***	4.75	-
10.5 46.5 f0			
1.0	-	3.20	-
1.0	-	3.20	-
1.0	-	3.20	-
1.0	-	3.50	-
1.0	-	3.50	-
6.0	5.0-7.0	2.85	2.80-2.90
22.0	17.0-27.0	3.70	3.60-3.80
35.0	35.0-50.0	4.45	4.30-4.55
70.0	70.0-90.0	4.50	4.35-4.65
70.0	70.0-90.0	4.00	4.00-4.25
142.0	***	4.75	-
11.5 46.5 f1			
0.1	-	1.20	-
0.9	-	3.35	-
1.0	-	3.15	-
1.0	-	3.15	-

h	Δh	Vs	ΔVs
1.0	-	3.15	-
8.0	6.5-9.5	3.00	2.90-3.10
25.0	21.5-28.5	3.70	3.60-3.80
75.0	60.0-75.0	4.50	4.40-4.60
100.0	82.5-100.0	4.45	4.30-4.60
70.0	70.0-90.0	4.45	4.20-4.65
68.0	***	4.75	-
12.5 46.5 f2			
0.1	-	3.50	-
0.4	-	3.50	-
1.5	-	2.85	-
1.0	-	2.85	-
4.0	-	2.85	-
14.0	10.5-17.5	3.40	3.35-3.50
17.0	17.0-21.5	3.85	3.65-4.05
35.0	35.0-45.0	4.35	4.20-4.50
110.0	90.0-110.0	4.50	4.35-4.65
110.0	85.0-110.0	4.50	4.20-4.80
57.0	***	4.75	-
13.5 46.5 f3			
0.2	-	1.70	-
1.0	-	2.40	-
3.2	-	3.15	-
0.5	-	3.15	-
3.0	-	3.15	-
10.0	10.0-14.0	3.15	3.15-3.30
25.0	25.0-37.5	3.85	3.65-4.05
30.0	30.0-40.0	4.40	4.20-4.60
100.0	80.0-100.0	4.40	4.20-4.60
70.0	70.0-90.0	4.40	4.20-4.60
107.0	***	4.75	-
14.5 46.5 f4			
1.0	-	2.35	-
1.0	-	2.35	-
1.0	-	2.35	-

h	Δh	Vs	ΔVs
0.5	-	3.25	-
0.5	-	3.35	-
10.0	8.0-12.0	3.20	3.15-3.25
24.0	19.0-29.0	3.85	3.70-3.95
35.0	35.0-47.5	4.40	4.20-4.60
105.0	85.0-105.0	4.40	4.20-4.60
65.0	65.0-87.5	4.40	4.20-4.60
107.0	***	4.75	-
15.5 46.5 f5			
0.1	-	2.20	-
0.8	-	2.40	-
0.7	-	2.75	-
0.8	-	3.30	-
0.5	-	3.35	-
4.0	4.0-6.0	2.80	2.70-2.90
18.0	14.5-21.5	3.50	3.40-3.60
30.0	30.0-45.0	4.25	4.10-4.40
65.0	65.0-82.5	4.50	4.35-4.65
110.0	90.0-110.0	4.40	4.20-4.60
120.0	***	4.75	-
7.5 46.5 f-3			
1.0	-	2.85	-
1.0	-	3.10	-
1.0	-	3.10	-
1.0	-	3.45	-
1.0	-	3.45	-
12.0	10.5-13.5	3.00	2.95-3.05
26.0	22.0-30.0	3.95	3.80-4.10
35.0	35.0-47.5	4.45	4.30-4.55
70.0	70.0-90.0	4.35	4.30-4.40
110.0	90.0-110.0	4.50	4.25-4.75
92.0	***	4.75	-
8.5 46.5 f-2			
1.0	-	2.85	-
1.0	-	3.10	-

h	Δh	Vs	ΔVs
1.0	-	3.45	-
1.0	-	3.45	-
1.0	-	3.45	-
11.0	9.0-13.0	3.05	2.90-3.20
24.0	21.0-27.0	3.90	3.80-3.95
35.0	35.0-52.5	4.60	4.45-4.75
70.0	70.0-90.0	4.30	4.15-4.45
110.0	90.0-110.0	4.50	4.25-4.75
95.0	***	4.75	-
9.5 46.5 f-1			
0.1	-	1.20	-
0.9	-	3.30	-
2.0	-	3.30	-
2.0	-	3.30	-
3.0	-	3.30	-
6.0	5.0-7.0	2.80	2.65-2.90
25.0	21.0-29.0	3.95	3.90-4.05
50.0	50.0-65.0	4.50	4.45-4.55
100.0	82.5-100.0	4.45	4.20-4.65
70.0	70.0-90.0	4.45	4.20-4.70
91.0	***	4.75	-
10.5 47.5 g0			
1.0	-	3.40	-
1.0	-	3.40	-
1.0	-	3.40	-
1.0	-	3.50	-
1.0	-	3.50	-
7.0	7.0-9.5	2.85	2.70-3.00
20.0	20.0-27.0	3.75	3.60-3.90
35.0	35.0-45.0	4.45	4.30-4.60
110.0	90.0-110.0	4.45	4.25-4.60
70.0	70.0-90.0	4.35	4.15-4.55
103.0	***	4.75	-
11.5 47.5 g1			
1.0	-	2.70	-

h	Δh	Vs	ΔVs
1.0	-	2.70	-
1.0	-	2.70	-
1.0	-	3.00	-
2.0	-	3.00	-
12.0	9.0-15.0	3.55	3.45-3.65
15.0	15.0-20.0	3.70	3.55-3.85
90.0	70.0-90.0	4.45	4.35-4.55
60.0	60.0-77.5	4.40	4.20-4.60
60.0	60.0-80.0	4.25	4.00-4.50
107.0	***	4.75	-
12.5 47.5 g2			
1.8	-	2.20	-
1.2	-	3.20	-
1.0	-	3.20	-
0.5	-	3.20	-
0.5	-	3.20	-
17.0	13.5-20.5	3.50	3.40-3.60
13.0	13.0-19.5	4.10	3.85-4.10
30.0	30.0-45.0	4.25	4.05-4.45
60.0	60.0-80.0	4.55	4.40-4.75
110.0	90.0-110.0	4.40	4.20-4.60
115.0	***	4.75	-
13.5 47.5 g3			
1.8	-	2.20	-
1.2	-	3.10	-
1.0	-	3.10	-
0.5	-	3.10	-
0.5	-	3.10	-
14.0	10.5-17.5	3.50	3.40-3.60
12.0	12.0-18.0	3.80	3.65-3.95
30.0	30.0-45.0	4.20	4.10-4.30
60.0	60.0-80.0	4.55	4.40-4.70
110.0	90.0-110.0	4.40	4.20-4.60
119.0	***	4.75	-
8.5 47.5 g-2			

h	Δh	Vs	ΔVs
0.5	-	2.30	-
0.5	-	2.65	-
1.0	-	2.90	-
2.0	-	3.45	-
2.0	-	3.40	-
13.0	11.5-14.5	3.30	3.25-3.35
30.0	30.0-40.0	4.20	4.10-4.30
30.0	30.0-45.0	4.65	4.55-4.80
100.0	80.0-100.0	4.30	4.25-4.40
70.0	70.0-90.0	4.45	4.20-4.65
101.0	***	4.75	-
9.5 47.5 g-1			
1.0	-	2.75	-
1.0	-	2.75	-
1.0	-	3.40	-
2.0	-	3.40	-
2.0	-	3.40	-
8.0	8.0-10.0	3.10	3.00-3.20
29.0	24.5-33.5	4.10	3.95-4.10
50.0	40.0-50.0	4.65	4.55-4.75
70.0	70.0-90.0	4.35	4.20-4.45
70.0	70.0-90.0	4.30	4.10-4.55
116.0	***	4.75	-

C. V_S-depth model of the Alpine region obtained after GFO.

V_S models obtained after the "hedgehog" inversion of surface-wave dispersion data and GFO smoothing optimization for Alpine region are listed in Table 5. Each representative cellular model is presented in the table by the thickness h (km) and shear-wave velocity V_S (km/s) of the layers down to the depth of 350 km. The range of variability of h and V_S are given for inverted layers. The quantities are rounded off to 0.5 km for the thickness and to 0.05 km/s for V_S. The independent information is used to constrain the inversion, therefore the chosen solution does not necessarily fall in the centre of the range that can be smaller than the relevant parameter step. The used relation between V_S and V_P is constant for all dependent parameters in the inversion ($V_P/V_S = \sqrt{3}$). The thickness marked by *** is not a truly inverted parameter, but it satisfies the condition that the total thickness from the free surface to the top of the fixed deep structure is equal to a predefined quantity H. In this study H=350 km according to the penetration depth of the used dispersion data. The structure deeper than H is the same for all the considered cells and is fixed according to the published model in Du *et al.* (1998).

Table 5. V_S models

h	Δh	Vs	ΔVs
8.5 44.5 d-2			
1.0	-	2.30	-
1.0	-	2.30	-
1.0	-	2.50	-
1.0	-	2.50	-
2.0	-	2.50	-
10.0	8.0-12.0	3.35	3.20-3.50
29.0	24.5-33.5	4.10	3.95-4.10
80.0	65.0-80.0	4.40	4.30-4.50
100.0	80.0-100.0	4.35	4.20-4.45
70.0	70.0-90.0	4.50	4.30-4.70
55.0	***	4.75	-
9.5 44.5 d-1			
1.0	-	2.30	-
1.0	-	2.50	-
1.0	-	2.50	-
2.0	-	2.50	-
10.0	7.5-12.5	3.30	3.15-3.45
28.0	24.0-28.0	4.00	3.90-4.00
85.0	70.0-85.0	4.45	4.35-4.55
70.0	70.0-87.5	4.25	4.05-4.45
70.0	70.0-90.0	4.50	4.25-4.75
81.0	***	4.75	-
10.5 44.5 d0			
3.0	-	2.00	-
1.4	-	2.20	-
1.6	-	2.80	-
0.5	-	3.25	-
0.5	-	3.25	-
12.0	11.5-12.5	3.35	3.30-3.40
20.0	20.0-30.0	3.95	3.85-4.05
30.0	30.0-45.0	4.45	4.25-4.60
100.0	75.0-100.0	4.45	4.20-4.65
50.0	50.0-75.0	4.00	4.00-4.20
130.0	***	4.75	-
11.5 44.5 d1			
2.0	-	2.00	-
1.0	-	2.15	-
1.4	-	2.15	-
1.6	-	2.80	-
1.0	-	3.25	-
17.0	13.0-21.0	3.4	3.35-3.50
30.0	25.0-35.0	4.15	4.00-4.30
30.0	30.0-40.0	4.80	4.65-4.80
100.0	80.0-100.0	4.35	4.15-4.55
60.0	60.0-80.0	4.45	4.20-4.65
105.0	***	4.75	-
6.5 44.5 d-4			

h	Δh	Vs	ΔVs
1.0	-	2.75	-
1.0	-	2.75	-
1.0	-	3.00	-
1.0	-	3.00	-
1.0	-	3.15	-
8.0	6.5-9.5	2.90	2.80-3.05
22.0	19.5-24.5	3.90	3.80-4.05
70.0	55.0-70.0	4.35	4.30-4.40
110.0	85.0-110.0	4.35	4.20-4.50
110.0	85.0-110.0	4.00	4.00-4.20
25.0	***	4.75	-
7.5 44.5 d-3			
1.0	-	2.75	-
1.0	-	2.85	-
1.0	-	3.00	-
1.0	-	3.10	-
1.0	-	3.10	-
6.0	6.0-8.0	2.65	2.55-2.80
20.0	20.0-30.0	3.85	3.70-4.00
85.0	67.5-85.0	4.40	4.30-4.50
100.0	80.0-100.0	4.35	4.20-4.50
100.0	80.0-100.0	4.50	4.25-4.75
34.0	***	4.75	-
6.25 45.5 e-4e			
1.0	-	2.90	-
1.0	-	2.90	-
1.0	-	3.00	-
1.0	-	3.10	-
1.0	-	3.10	-
7.0	6.0-8.0	2.75	2.70-2.80
15.0	11.5-18.5	3.75	3.60-3.90
48.0	38.0-48.0	4.35	4.30-4.40
110.0	90.0-110.0	4.45	4.30-4.60
70.0	70.0-90.0	4.40	4.20-4.60
95.0	***	4.75	-

h	Δh	Vs	ΔVs
6.75 45.5 e-4w			
1.0	-	2.75	-
1.0	-	2.75	-
1.0	-	3.00	-
1.0	-	3.00	-
1.0	-	3.10	-
8.0	6.5-9.5	2.80	2.70-2.90
18.0	17.0-19.0	3.85	3.75-3.95
75.0	62.5-75.0	4.35	4.30-4.40
70.0	70.0-90.0	4.60	4.55-4.65
70.0	70.0-90.0	4.35	4.15-4.55
104.0	***	4.75	-
7.25 45.5 e-3w			
0.1	-	2.85	-
1.9	-	2.85	-
2.0	-	3.00	-
1.0	-	3.10	-
1.0	-	3.25	-
9.0	7.5-10.5	2.90	2.80-3.00
24.0	20.5-27.5	3.90	3.80-4.05
65.0	47.5-65.0	4.35	4.25-4.45
70.0	70.0-90.0	4.50	4.40-4.60
70.0	70.0-90.0	4.35	4.15-4.55
106.0	***	4.75	-
7.75 45.5 e-3e			
0.1	-	1.20	-
0.4	-	2.55	-
1.5	-	2.70	-
2.0	-	2.85	-
1.0	-	3.05	-
11.0	9.5-12.5	3.00	2.90-3.10
33.0	27.0-39.0	4.15	4.05-4.15
30.0	30.0-42.5	4.60	4.50-4.70
110.0	90.0-110.0	4.35	4.25-4.45
110.0	90.0-110.0	4.30	4.10-4.55

h	Δh	Vs	ΔVs
51.0	***	4.75	-
8.5 45.5 e-2			
1.0	-	2.43	-
1.0	-	2.43	-
1.0	-	2.43	-
1.0	-	2.90	-
2.0	-	2.90	-
10.0	8.0-12.0	3.15	3.05-3.30
25.0	21.0-29.0	4.00	3.90-4.10
80.0	65.0-80.0	4.45	4.35-4.55
100.0	80.0-100.0	4.35	4.20-4.50
70.0	70.0-90.0	4.40	4.20-4.60
59.0	***	4.75	-
9.5 45.25 e-1s			
1.0	-	1.45	-
1.0	-	1.80	-
1.0	-	2.30	-
1.0	-	2.40	-
1.0	-	2.75	-
8.0	8.0-9.8	3.65	3.60-3.70
13.0	10.0-16.0	3.55	3.45-3.65
32.0	24.5-39.5	4.20	4.10-4.30
110.0	90.0-110.0	4.40	4.30-4.50
110.0	90.0-110.0	4.40	4.20-4.60
72.0	***	4.75	-
9.5 45.75 e-1n			
1.0	-	2.75	-
1.0	-	3.00	-
1.0	-	3.35	-
0.5	-	3.45	-
0.5	-	3.45	-
7.0	5.5-8.5	2.70	2.60-2.85
24.0	20.0-28.0	3.70	3.60-3.80
62.0	47.0-62.0	4.40	4.25-4.55
70.0	70.0-90.0	4.30	4.20-4.45

h	Δh	Vs	ΔVs
110.0	90.0-110.0	4.50	4.30-4.70
73.0	***	4.75	-
10.5 45.5 e0			
1.0	-	2.00	-
1.0	-	2.56	-
1.0	-	2.56	-
2.0	-	3.01	-
1.0	-	3.01	-
7.0	6.0-8.0	3.15	3.05-3.25
21.0	18.0-24.0	3.75	3.65-3.85
90.0	70.0-90.0	4.45	4.35-4.55
50.0	50.0-70.0	4.50	4.25-4.75
70.0	70.0-90.0	4.00	4.00-4.40
106.0	***	4.75	-
11.5 45.5 e1			
3.0	-	2.55	-
1.5	-	2.55	-
1.5	-	3.18	-
0.5	-	3.30	-
0.5	-	3.30	-
7.0	5.5-8.5	3.05	2.90-3.15
28.0	24.5-31.5	3.80	3.65-3.90
40.0	40.0-60.0	4.75	4.60-4.80
110.0	90.0-110.0	4.40	4.25-4.55
60.0	60.0-82.5	4.50	4.25-4.75
97.0	***	4.75	-
12.5 45.5 e2			
1.0	-	2.10	-
2.0	-	2.50	-
2.0	-	2.50	-
1.0	-	2.90	-
1.0	-	2.90	-
14.0	10.5-17.5	3.35	3.30-3.40
20.0	20.0-30.0	3.90	3.75-4.10
60.0	45.0-60.0	4.65	4.55-4.80

h	Δh	Vs	ΔVs
90.0	70.0-90.0	4.40	4.25-4.55
50.0	50.0-75.0	4.45	4.20-4.65
108.0	***	4.75	-
13.5 45.5 e3			
1.0	-	2.10	-
4.0	-	2.60	-
1.0	-	3.00	-
1.0	-	3.20	-
1.0	-	3.20	-
12.0	12.0-15.0	3.30	3.25-3.35
25.0	22.5-27.5	3.95	3.80-4.10
90.0	75.0-90.0	4.65	4.60-4.70
90.0	70.0-90.0	4.20	4.10-4.25
50.0	50.0-70.0	4.50	4.25-4.75
74.0	***	4.75	-
8.5 46.5 f-2			
0.1	-	2.85	-
1.9	-	2.85	-
2.0	-	3.00	-
1.0	-	3.10	-
1.0	-	3.25	-
9.0	7.5-10.5	2.90	2.80-3.00
24.0	20.5-27.5	3.90	3.80-4.05
65.0	47.5-65.0	4.35	4.25-4.45
70.0	70.0-90.0	4.50	4.40-4.60
70.0	70.0-90.0	4.35	4.15-4.55
106.0	***	4.75	-
9.5 46.5 f-1			
0.1	-	1.20	-
0.4	-	2.55	-
1.5	-	2.70	-
2.0	-	2.85	-
1.0	-	3.05	-
11.0	9.5-12.5	3.00	2.90-3.10
33.0	27.0-39.0	4.15	4.05-4.15

h	Δh	Vs	ΔVs
30.0	30.0-42.5	4.60	4.50-4.70
110.0	90.0-110.0	4.35	4.25-4.45
110.0	90.0-110.0	4.30	4.10-4.55
51.0	***	4.75	-
10.5 46.5 f0			
1.0	-	3.20	-
1.0	-	3.20	-
1.0	-	3.20	-
1.0	-	3.50	-
1.0	-	3.50	-
6.0	5.0-7.0	2.85	2.80-2.90
22.0	17.0-27.0	3.70	3.60-3.80
35.0	35.0-50.0	4.45	4.30-4.55
110.0	90.0-110.0	4.50	4.35-4.65
70.0	70.0-90.0	4.00	4.00-4.25
102.0	***	4.75	-
11.5 46.5 f1			
1.0	-	1.45	-
1.0	-	1.80	-
1.0	-	2.30	-
1.0	-	2.40	-
1.0	-	2.75	-
8.0	8.0-9.8	3.65	3.60-3.70
13.0	10.0-16.0	3.55	3.45-3.65
32.0	24.5-39.5	4.20	4.10-4.30
110.0	90.0-110.0	4.40	4.30-4.50
110.0	90.0-110.0	4.40	4.20-4.60
72.0	***	4.75	-
12.5 46.5 f2			
0.1	-	3.50	-
0.4	-	3.50	-
1.5	-	2.85	-
1.0	-	2.85	-
4.0	-	2.85	-
14.5	11.0-18.0	3.40	3.30-3.50

h	Δh	Vs	ΔVs
17.0	17.0-21.5	3.85	3.65-4.05
35.0	35.0-45.0	4.35	4.15-4.55
110.0	90.0-110.0	4.50	4.30-4.70
60.0	60.0-85.0	4.50	4.25-4.75
106.5	***	4.75	-
13.5 46.5 f3			
0.2	-	1.70	-
1.0	-	2.40	-
3.2	-	3.15	-
0.5	-	3.15	-
3.0	-	3.15	-
10.0	10.0-14.0	3.15	3.15-3.30
25.0	25.0-37.5	3.85	3.65-4.05
30.0	30.0-40.0	4.40	4.20-4.60
100.0	80.0-100.0	4.40	4.20-4.60
70.0	70.0-90.0	4.40	4.20-4.60
107.0	***	4.75	-
14.5 46.5 f4			
0.2	-	1.70	-
1.0	-	2.40	-
3.2	-	3.15	-
0.5	-	3.15	-
3.0	-	3.15	-
10.0	10.0-14.0	3.15	3.15-3.30
25.0	25.0-37.5	3.85	3.65-4.05
30.0	30.0-40.0	4.40	4.20-4.60
100.0	80.0-100.0	4.40	4.20-4.60
70.0	70.0-90.0	4.40	4.20-4.60
107.0	***	4.75	-
7.5 46.5 f-3			
1.0	-	2.90	-
1.0	-	2.90	-
1.0	-	3.00	-
1.0	-	3.10	-
1.0	-	3.10	-

h	Δh	Vs	ΔVs
8.0	6.5-9.5	2.80	2.70-2.90
18.0	17.0-19.0	3.85	3.75-3.95
75.0	62.5-75.0	4.35	4.30-4.40
70.0	70.0-90.0	4.60	4.55-4.65
70.0	70.0-90.0	4.35	4.15-4.55
104.0	***	4.75	-
8.5 47.5 g-2			
0.5	-	2.30	-
0.5	-	2.65	-
1.0	-	2.90	-
2.0	-	3.45	-
2.0	-	3.40	-
13.0	11.5-14.5	3.25	3.20-3.30
30.0	30.0-40.0	4.20	4.10-4.30
30.0	30.0-45.0	4.65	4.55-4.80
60.0	60.0-80.0	4.30	4.25-4.40
110.0	90.0-110.0	4.45	4.20-4.65
101.0	***	4.75	-
9.5 47.5 g-1			
1.0	-	2.75	-
1.0	-	2.75	-
1.0	-	3.40	-
2.0	-	3.40	-
2.0	-	3.40	-
8.0	8.0-10.2	3.30	3.20-3.40
20.0	20.0-24.5	3.80	3.65-3.95
30.0	30.0-40.0	4.65	4.55-4.75
110.0	90.0-110.0	4.45	4.30-4.55
70.0	70.0-90.0	4.25	4.00-4.50
105.0	***	4.75	-
10.5 47.5 g0			
1.0	-	3.40	-
1.0	-	3.40	-
1.0	-	3.40	-
1.0	-	3.50	-

h	Δh	Vs	ΔVs
1.0	-	3.50	-
7.5	7.5-10.0	2.85	2.70-3.00
20.0	20.0-27.0	3.75	3.60-3.90
35.0	35.0-45.0	4.45	4.30-4.60
110.0	90.0-110.0	4.45	4.25-4.60
70.0	70.0-90.0	4.35	4.15-4.55
102.5	***	4.75	-
11.5 47.25 g1s			
2.0	-	2.70	-
1.0	-	2.70	-
1.0	-	3.00	-
1.0	-	3.00	-
1.0	-	3.00	-
9.0	9.0-12.5	3.35	3.25-3.40
20.0	20.0-30.0	3.85	3.60-4.10
25.0	25.0-37.5	4.35	4.15-4.55
70.0	70.0-90.0	4.50	4.35-4.65
70.0	70.0-90.0	4.30	4.05-4.55
150.0	***	4.75	-
11.5 47.75 g1n			
1.8	-	2.20	-
1.2	-	3.20	-
2.0	-	3.20	-
1.0	-	3.20	-
1.0	-	3.20	-
14.0	10.5-17.5	3.50	3.40-3.60
16.0	16.0-24.0	4.10	3.90-4.10
45.0	34.0-56.0	4.25	4.05-4.45
70.0	70.0-90.0	4.60	4.45-4.75
70.0	70.0-90.0	4.15	4.15-4.40
128.0	***	4.75	-
12.5 47.5 g2			
1.8	-	2.20	-
1.2	-	3.20	-
1.0	-	3.20	-
0.5	-	3.20	-
0.5	-	3.20	-
17.0	13.5-20.5	3.35	3.25-3.40
13.0	13.0-19.5	4.10	3.85-4.10
30.0	30.0-45.0	4.25	4.05-4.45
100.0	80.0-100.0	4.55	4.40-4.75
70.0	70.0-90.0	4.40	4.20-4.60
115.0	***	4.75	-
13.5 47.5 g3			
1.8	-	2.20	-
1.2	-	3.10	-
1.0	-	3.10	-
0.5	-	3.10	-
0.5	-	3.10	-
11.0	10.5-11.5	3.35	3.30-3.40
18.0	17.0-19.0	3.80	3.75-3.85
30.0	30.0-45.0	4.30	4.25-4.35
100.0	80.0-100.0	4.55	4.50-4.60
70.0	70.0-90.0	4.40	4.35-4.45
116.0	***	4.75	-